Vibration-based wheel-terrain slip detection for skid-steer rovers

Pierre-Lucas Aubin-Fournier

A Thesis

in

The Department

of

Electrical Engineering and Computer Science

Presented in Partial Fulfillment of the Requirements

for the Degree of

Master of Applied Science (Electrical Engineering) at

Concordia University

Montréal, Québec, Canada

May 2023

CONCORDIA UNIVERSITY

School of Graduate Studies

This is to certify that the thesis prepared

By: **Pierre-Lucas Aubin-Fournier**

Entitled: **Vibration-based wheel-terrain slip detection for skid-steer rovers**

and submitted in partial fulfillment of the requirements for the degree of

Master of Applied Science (Electrical Engineering)

complies with the regulations of this University and meets the accepted standards with respect to originality and quality.

Signed by the Final Examining Committee:

____________________________________ Chair
Dr. Luis Rodrigues

____________________________________ Examiner
Dr. Paula Lago

____________________________________ Supervisor
Dr. Krzysztof Skonieczny

Approved by ____
Yousef R. Shayan, Chair
Department of Electrical Engineering and Computer Science

______________ 2023

____
Mourad Debbabi, Dean
Gina Cody School of Engineering and Computer Science

Abstract

Vibration-based wheel-terrain slip detection
for skid-steer rovers

Pierre-Lucas Aubin-Fournier

To fulfill their mission properly, planetary exploration rovers must often be able to travel long distances and traverse various terrain types. Some terrain types and topologies may present traversability challenges. In difficult situations, such as slopes and loose soil, rover wheel slip may increase to a level leading to entrapment risks. Autonomous slip detection allows a rover to detect potentially dangerous terrain and take precautions. While visual odometry slip estimation solutions exist, numerous external factors, such as luminance, haze and shadows, may negatively impact quality of imaging sensor data and consequently slip estimation. Visual odometry also requires significant computational resources. Previous studies have shown promise in the use of Machine Learning algorithms to process IMU-measured vibration data to detect and classify slip events. This research develops a low-latency and computationally efficient vibration-based system to detect wheel-terrain slip events for skid-steer rovers with modest hardware requirements.

To this end, vibration datasets corresponding to various wheel-terrain slip values are generated. A Husky rover with two Inertial Measurement Unit sensors is used in indoor and outdoor test environments. Slip is induced at specific values by mechanically constraining the rover to reduce the Actual Rover Speed below the Commanded Rover Speed. The vibration datasets are used to train and validate a Support Vector Machine classifier to differentiate abnormally high slip events from normal low slip. The training is done with various sensor outputs, sampling time, and sampling frequency. The performance of the system is then evaluated in order to find which combinations of parameters are effective and to qualify the trade-offs in performance which come with less ideal parameter values.

Acknowledgments

I wish to express my gratitude to Professor Krzysztof Skonieczny for his guidance, generous patience, and unwavering support throughout my Master’s thesis. His constructive criticism, precisely applied peer pressure and dedication to my academic growth have been instrumental in shaping my research and helping me achieve my academic goals. I am also grateful to my partner Thy, whose constant energetic encouragement and motivation kept me going through the challenging times of thesis writing. Her unwavering belief in my abilities and willingness to sacrifice her time and energy to support me are truly commendable. Being asked ”So how’s your thesis?!” on a regular basis, with a hint of sadistic glee, definitely helped keep my eyes on the prize. Without their support, this thesis would not have been possible, and I will forever be thankful to both of them.

I also wish to acknowledge the support I received from my parents throughout my slow and steady academic progression. I can imagine how much harder it would have been to reach this point without them and I am very thankful that they are still present to witness this achievement. I hope it will bring them parental pride and satisfaction.

I must also extend my thanks to the Canadian Space Agency for granting our research group access to their testing grounds on multiple occasions. This was critical in carrying out the field experiments presented in this thesis. Their cooperation made it possible to conduct high-quality field tests and obtain valuable datasets that would have been otherwise difficult to obtain.

And finally, I wish to express my gratitude to our industrial partner, Mission Control Space Services, for their research funding and technical consultations. Their financial support and technical advice played a significant role in the successful completion of this research. Their commitment to advancing scientific research and innovation in the field of remote exploration robotics is commendable, and it was a pleasure to work with them.

Contents

List of Figures

List of Tables

Acronyms

AE Auto-Encoders 12

ANN Artificial Neural Network 11 f.

ARL Aerospace Robotics Lab 19

AUC Area Under the Curve 49, 57, 62, 67

AWS ”all-wheel slippage” 8 f.

CI Current Indicator 9

CNN Convolutional Neural Networks 12

CPU Central Processing Unit 7

CSA Canadian Space Agency 24, 27 f., 40, 49

DOF degree of freedom 6, 31, 38, 49, 66

EI Encoder Indicator 9

F/T force/torque 10, 31

FFT Fast Fourier Tranform 37, 39, 62

GI Gyro Indicator 9

GNSS global navigation satellite system 44, 68

GRC-1 Glenn Research Center-1 20, 40

IMU Inertial Measurement Unit . . . 2, 4, 6, 10–13, 15 ff., 19, 21, 23, 27, 29, 31, 33, 37 ff., 44, 49 f., 55, 57, 62, 66 ff.

IPEM Integrated Prediction Error Minimization . . . 10

LSTM Long-Short Term Memory . . . 12

MC Motor Current . . . 4, 7 ff., 13

MER Mars Exploration Rover . . . 7, 13

ML Machine Learning . . . 4 f., 10 f., 17

MSL Mars Science Laboratory . . . 7, 13

PCA Principal Component Analysis . . . 62

PE Pose Estimation . . . 6, 10

RBF Radial Basis Function . . . 35 f.

RMS Root Mean Square . . . 39 f.

ROC Receiver Operating Characteristic . . . 49 f., 57, 62, 67

ROS Robot Operating System . . . 23, 60

RTK Real-time kinematic positioning . . . 44, 68

SNR Signal-to-noise ratio . . . 39

SOM Self-Organizing Maps . . . 11

SVM Support Vector Machine . . . 10 ff., 16 f., 35, 37 f., 42, 49, 57, 60, 62, 66 ff.

UGV Unmanned Ground Vehicles . . . 13

VCE Vision Compute Element . . . 13

VO Visual Odometry . . . 4, 6 f., 13, 16, 68

VTWD VO Thinking While Driving . . . 7, 13

WO Wheel Odometry . . . 4, 6, 8 ff., 13

Chapter 1

Introduction

Despite the impressive progress made over the past few decades in the field of extraterrestrial exploration rovers, many outstanding technical challenges have been encountered. A notable and significant one is terrain traversability evaluation. Given the usual mission goal of obtaining maximum scientific value over the rover's functional lifetime, this challenge can be linked to two specific design issues. First, how can the rover be kept moving at its nominal safe speed and second, how to judge the rover's capacity to traverse potentially difficult terrain leading to valuable mission targets (Gonzalez & Iagnemma, 2018). The topic of this research, wheel-terrain slip detection, relates to the first design issue and has attracted the attention of a number of academic research teams and motivated them to research potential solutions.

Prior work from our lab (Skonieczny, Shukla, Faragalli, Cole, & Iagnemma, 2019) summarizes persisting challenges:

> The motivation for studying rover mobility, and particularly rover slip, is most clearly demonstrated by examples from NASA's Mars exploration missions. Spirit had experienced high slip when crossing loose sandy terrains and ultimately its mission ended after it became embedded in a sulfate sand-filled crater (Arvidson et al., 2010). Opportunity has experienced high wheel sinkage and slip on multiple occasions when traversing sandy crater walls or wind-blown ripples. In some instances wheel slip approached 100%, leading to scenarios where the rover could not reach the desired traverse target and was forced to reroute (Arvidson et al., 2011). The most significant

> difficulty for Opportunity was the embedding event in what was dubbed "Purgatory Dune" that lasted from Sol 446 to Sol 484. To date, Opportunity has lost more than 6 weeks of progress while engineers focused on extrication from embedding events. Curiosity has also experienced mobility difficulties when traveling over loose, wind-deposited soil, with the most extreme slip events occurring when the rover attempted to travel over shallow slope formations (ripples). More specifically, Curiosity has experienced high slip events (up to 77% slip) on sols 672 and 709–711 during travel into the Hidden Valley ripple formation (Arvidson et al., 2017).

The Emirates Lunar Mission, to which our research group is a science team partner, will land on the Moon in late April 2023 and deploy the Rashid rover. The rover will collect telemetry, such as motor current and Inertial Measurement Unit (IMU) data, at 8 Hz and have very modest computational capabilities. Further, this rover is illustrative of an upcoming class of international and commercial Lunar microrovers, including one being developed by the Canadian Space Agency, that demonstrate modest capabilities. A key question is whether slip detection is feasible for such a class of rovers.

It is valuable to mention a few criteria based on which the usefulness of various slip detection strategies can be evaluated. Specifically, since these technologies are aimed at the context of rover missions for interplanetary exploration, the evaluation of their value must take this context into account. It is natural that some solutions may not be suitable or appropriate to an interplanetary mission context while still having considerable research value.

It may sometimes be tempting to dismiss concerns about costs with the notion that space exploration is, by its nature, costly. However, the reality is that most space exploration missions will have budgetary constraints. Between solutions with similar specifications and performance, a significantly cheaper option will often be preferred. Otherwise, if an optional system's cost is more than expected or than is considered reasonable, its implementation may be cut from the project altogether. Cost is also often a significant base factor when boiling down other criteria & technical constraints to their simplest constituents.While costs are not explicitly considered in this research, modest system requirements for non-essential systems helps reduce costs.

While cost is somewhat of an arbitrary external constraint, reliability on the other hand is a strict internal requirement. Given the interplanetary exploration context which many of these systems are designed for, the ability of the system to provide appropriate results throughout the duration of the mission and beyond is important. Once the system goes beyond low-earth orbit, hardware malfunctions can likely only be addressed using workarounds. While reliability is not explicitly considered in this research, modest system requirements for non-essential systems helps increase reliability by reducing system complexity.

Reliability concerns also consider the various harsh environmental conditions to which the system can be subjected during its mission. It is worth mentioning that for some missions the expected lifetime of the exploration hardware can be very short. Sometimes measured in days for exploration of hot and cold bodies like the Moon. Sometimes measured in minutes for hot, high pressure and corrosive environments such as the surface of Venus. This aspect plays a significant role in deciding the balance of resources dedicated to improving reliability and environment resiliency vs payload capacity or sensor quality. While durability in harsh environmental conditions is not explicitly considered in this research, proprioceptive vibration sensors can be mounted at various locations on the rover chassis which makes shielding them from harsh environmental conditions relatively simple.

As with most technological solutions, slip estimation or classification systems described in the literature come in various degrees of complexity, with corresponding system requirements, limitations and trade-offs. Some sensor systems may be specifically designed for certain rover designs and may not be implementable as is in a different type of rover. Others may have strict hardware size and weight requirements that make them unfeasible to implement in an exploration vehicle smaller than a certain size. In this research a slip classification system for skid-steer rovers with modest requirements is presented. Specifically, this research demonstrates how modest certain requirements can be before performance degrades and by how much it degrades.

1.1 Wheel-terrain slip in skid-steer rover dynamics

Exploration rovers have been designed with various types of locomotion systems. The four-wheeled skid-steer rover is the simplest that is commonly used, and is the typical configuration for the upcoming class of Lunar microrovers. In its simplest suspensionless mechanical form, all four wheels are mounted on static axles and two motors are used to apply mechanical power to the wheels. The left and right wheel pairs are each driven by a single motor. The resulting system will tend to move in a straight line with both motors commanded to the same speed and will tend to change orientation when the two motors are commanded different speeds. In ideal conditions, the system can achieve turns of any radius down to point-turns. However, these turning motions create a skidding action between the wheels and the ground, hence the ”skid-steering” name. Significant frictional forces are exerted on the wheels as a consequence of this skidding, which can make certain turning motions difficult, especially in soft, granular, and deformable soils. Nevertheless, because of their mechanical and control simplicity, the skid-steer rover design can be a pertinent option for modest or heavily constrained exploration missions.

1.2 Types of slip estimation & detection systems

1.2.1 Exteroceptive Estimators

Exteroceptive estimators rely on exteroceptive sensor measurements of environmental stimuli originating outside a system (e.g. camera images) to estimate the rover slip based on global estimates of the amount of actual rover displacement. These methods can come with significant and cumbersome hardware requirements, such as quality navigation cameras and dedicated image processing hardware. However, these techniques tend to provide robust and accurate estimation of slip. Indeed, Visual Odometry (VO), a notable sensor-based has proven its value in multiple rover missions to Mars. It is routinely used to establish ground-truth of previously executed rover movements. However, along with its demanding hardware requirements, it can also only accomplish estimation steps at a low frequency which can significantly reduce the overall average rover speed.

1.2.2 Proprioceptive Detectors

Proprioceptive detectors rely on sensor measurement of stimuli which are internal to the system (e.g. structure vibrations, applied forces, electrical power consumption, component positions & movements, etc). For slip estimation, these sensor measurements then require some form of post-processing or interpretation.

This can be done using empirical estimators or through Machine Learning (ML) algorithms. Empirical estimators are mathematical models based on deterministic assumptions, for example from terramechanics (e.g. Bekker-derived models (Bekker, 1956)) or electrical motor theory (e.g. Motor empirical models). These models rely on sensor measurements such as IMUs, Wheel Odometry (WO) from motor encoders, Motor Current (MC) and may also require knowledge of terrain parameters (Lopez-Arreguin & Montenegro, 2021). These techniques have demonstrated effectiveness and some even provide real-time results without requiring hardware beyond what is already usually available on exploration rovers. However, these techniques can suffer from model error issues. In remote planetary environment with reduced gravity, Earth-based terramechanics models may not be entirely accurate which can reduce the effectiveness of these slip estimation techniques; further, Earth-based assumptions tend to err on the side of underestimating rover mobility challenges (Niksirat, Daca, & Skonieczny, 2020). Given the complexity and limitations of induced micro-gravity experiments, accurately evaluating mobility system performance during the design phase remains an open research problem (Daca, Nassiraei, Tremblay, & Skonieczny, 2022). Soil parameters also play a significant role in both terramechanics and motor modeling. There is significant uncertainty about the soil parameters of remote planetary environments (Lopez-Arreguin & Montenegro, 2021). Without this a priori knowledge, the effectiveness of these techniques is often reduced in mission environments compared to lab conditions.

ML estimators can also be used for raw data interpretation and show significant promise for slip estimation applications, amongst others. Implemented as classifiers or as regression tools, they can provide pertinent information to identify dangerous slip conditions. However, ML systems may rely on complex algorithms and/or require significant training data to provide acceptable results. Even in good conditions, ML systems tend to have worse performance than established exteroceptive methods. Nevertheless, appropriately designed ML estimators can provide valuable information from otherwise difficult to decipher sensor data at a higher rate than exteroceptive methods.

Chapter 2

Literature Review

This chapter presents existing exteroceptive and proprioceptive slip estimation/detection systems, and then provides a discussion and synthesis of them from the perspectives of computational and sensing requirements.

2.1 Existing literature on slip estimation systems

2.1.1 Exteroceptive Estimators

In Helmick, Cheng, Clouse, Matthies, and Roumeliotis (2004), a sensor-based slip regression estimation system is described. It uses rover Pose Estimation (PE), in which VO and IMU measurements are combined through a Kalman filter to obtain a 3 degrees of freedom (DOF) rover motion estimate. This estimate is then compared to a rover WO motion estimate obtained from the vehicle kinematics of the rocker-bogie suspension system with a no-slip assumption. Any significant difference between the two estimates indicates the possible occurrence of wheel-terrain slip. The VO step requires a stereo-camera and requires significant mission time for the rover to stop moving, capture an image of its surroundings and process the visual data into a PE. No specific numbers are provided regarding the computing time required or for the distance traveled and time required between slip estimation steps.

Reina, Ishigami, Nagatani, and Yoshida (2010) presents a slip estimation system based on VO system. The system relies on a rear-facing camera to image the track left in deformable terrain by the rear left wheel of the rover. A Hough transform is then applied to the images and the results are handled by fuzzy inference model to track the wheel trace location. This system also relies on a magnetic compass to measure the yaw rate or z-axis angular speed of the rover, which may not be suitable in environments without a sufficient planetary magnetic field. The authors do mention that this compass could be replaced by another suitable sensor for angular speed, such as a gyroscope or an IMU. In the article, the system is presented specifically as a method to improve dead-reckoning odometry by compensating for slip error. As such, the focus is on the accuracy of the odometry correction, with impressive results. It is not clear what the latency of slip detection in this system would be. It is however clear that this system imposes the significant hardware requirement of a rear-facing camera and may also impose significant computational load to process the images, especially if done at the suggested rate of 5 Hz.

Gonzalez, Rodriguez, Guzman, Pradalier, and Siegwart (2012) present a sensor-based VO and compass system. Two monocular cameras are used, one is pointed down at the ground in front of the rover and the other is pointed at the environment further ahead or to the sides of the rover. The images are then processed using a template matching algorithm, which has some advantages over a technique based on optical flow. In a nutshell, optical flow relies on detected features in images to track movement whereas template matching does not. Sandy soil environments such as the Moon and Mars tend to lack strong easily detected features. With template matching, larger patterns of gradients (i.e. templates) are used to estimate motion between subsequent captured images. This technique is quite interesting in the fact that it makes use of both local and global measurements for localization. The camera pointing down at the ground close to the rover is suitable to detect small local Cartesian motions, but will tend to accumulate error over time or may introduce sudden jumps in error if mistakes occur in individual iterations of the algorithm, especially during turning motions. The camera looking at the global surroundings, on the other hand, provides a robust evaluation of the rover pose angle. Such an arrangement of sensors has been shown to produce very accurate localization estimates with probabilistic sensor fusion systems such as Kalman filtering (Li, Aubin-Fournier, & Skonieczny, 2020). As with most vision-based systems, this method can have issues with difficult imaging conditions, and processing images imposes a significant computational cost.

In Arvidson et al. (2017) and Gonzalez and Iagnemma (2018), NASA's Mars Science Laboratory (MSL) Curiosity rover's slip estimation strategy is discussed. This strategy consists mainly of a mixture of empirical estimation using MC readings and intermittent sensor-based VO iterations to more accurately assess wheel slip over the last segment driven. The VO system is largely the same as what was used for NASA's Mars Exploration Rover (MER) Spirit & Opportunity relies on detected features in stereo images captured from mast-mounted navigation cameras. The feature detection uses an interest operator tuned for corner detection. Over Opportunity's first year of operation, the VO system managed to converge 95% of the time (Cheng, Maimone, & Matthies, 2005). The empirical estimator is quite simple, consisting only of an experimentally determined fixed MC threshold over a 20 s window. If the threshold is exceeded over the entire window, Curiosity stops moving and captures images to conduct a VO localization and slip estimation iteration. According to Maimone, Patel, Sabel, Holloway, and Rankin (2022), outside of these high-slip events, the VO iterations tend to be conducted every 60 s to 90 s when using the ”VO Full” drive mode. In good terrain conditions, this corresponds to nominal driving steps of 1 m between VO iterations. Other available driving modes have longer travel distance before VO iterations is done allowing faster average travel speed on low risk terrain. However, following an embedding event on sol 672 ”VO full” became the main driving mode to reduce entrapment risks. Over the first 9 years of Curiosity's mission, up to 87% of the total cumulative commanded drive distance has been done using the ”VO full” drive mode. This led to a design effort to update Curiosity's drive mode with the VO Thinking While Driving (VTWD) capability to allow VO computation while traversing the next movement step instead of having to wait immobile for approximately 30 s at every iteration. This dramatically improves average driving speed and makes better use of otherwise idle time on the rover's Central Processing Unit (CPU), however it can be noted that the VO processing almost constantly claims 50%+ of the CPU utilization while using the VTWD drive mode.

2.1.2 Proprioceptive Detectors

In Ojeda, Cruz, Reina, and Borenstein (2006), an empirical slip estimation system is presented. It uses MC measurements to correct slip-induced error in WO and produces an estimation of the condition where all of the rover's wheels are slipping, identified as ”all-wheel slippage” (AWS). This system requires some knowledge of the terrain's terramechanics parameters which may be acquired through 3 provided tuning techniques. Two of those techniques require a ground truth measurement such as GPS and the third method provides a less accurate parameter estimation without requiring a ground truth measurement. This third method consists of inducing slip in a single wheel on a six-wheeled rover by spinning it faster with the assumption that the rover will move according to the speed of the five other wheels. Measuring the MC in this single slipping wheel allows an estimation of the terrain parameters to be made. This method may not be suitable for a four-wheeled skid-steer rover, especially if the front and rear wheels on the same side are driven by a single motor. It is also mentioned that slip estimation while climbing slopes is possible with this system. The system lowers the MC threshold according to the slope angle, since the wheels may slip at a lower exerted torque. The biggest drawback of this technique is the required knowledge of terrain parameters. In mission environments, these parameters may be difficult to evaluate and may fluctuate significantly as the rover traverses through different terrain types and conditions, leading to risks of unreliable slip detection.

In Reina, Ojeda, Milella, and Borenstein (2006), an empirical estimator for the AWS condition is presented. It uses WO encoder data, MC readings and also yaw rate or z-axis angular speed measured by a fiber optic gyroscope. Three indicators are presented where these measurements are evaluated, these indicators are then compared using a fuzzy logic system. This results in a confidence in the presence of the AWS condition. A flag for the AWS condition is raised if the confidence level passes a predefined treshold. The first indicator, the Encoder Indicator (EI), compares the encoder readings of the six wheels with each other. Large differences in encoder readings between wheels on the same side of the rover would indicate wheel slippage. The second indicator, the Gyro Indicator (GI), compares WO with the z-axis gyro. Discrepancies between the z-axis angular speed interpreted from WO and the measured z-axis angular speed would indicate wheel slippage. The third indicator, the Current Indicator (CI), monitors the MC for each wheel as an evaluation of the external torque applied on the wheel. This torque estimation is compared to the maximum allowable shear strength of the terrain, obtained using the Coulomb-Mohr soil failure criterion (Bekker, 1960). From the results shown in the article, with all three indicators considered, this system seems to work well in laboratory conditions, with prior knowledge of the terrain parameters and on an artificial slope AWS detection accuracy is shown to be 94%. The more realistic tests where small sand mounds are used to create AWS events seemed to be more challenging for the system, showing significantly worse performance with only 61% accuracy for AWS occurence detection. The performance of individual indicators was much lower in all conditions and these indicators may also not be as suitable to other rover mobility systems with less independent wheels, such as skid-steer rovers.

In Bussmann, Meyer, Steidle, and Wedler (2018) an empirical slip estimation system based on direct IMU readings is presented. The system starts with WO PE data from the vehicle kinematics, which includes the wheel encoders and considers the joint positions of the rover. It then uses readings of linear accelerations and angular rates from the IMU. It processes these readings using the Integrated Prediction Error Minimization (IPEM) method, which uses a motion model to interpret the data and improve the accuracy of the WO PE. This system makes the assumption that all wheels slip simultaneously, which may not always be the case in complex terrain conditions. The motion model of the system includes a series of slip parameters which must be calibrated using empirical data. This may mean the slip estimation will only be valid for the specific terrain conditions in which the system is tested for calibration and other terrain conditions will increase the estimation error. Overall, while this kind of model does provide an improvement to the accuracy of the WO estimates when properly calibrated, it also hints at significant limitations in complex and unknown terrain conditions. Furthermore, IMU integration is well known to rapidly develop large drift errors due to noise and the inherent noise amplification of the integration step.

In Omura and Ishigami (2017) a special type of sensor suite is proposed where the normal force and the contact angle at the wheel-sand interaction boundary are measured. Data is collected in a single-wheel testing gantry system for a variety of slip conditions divided into three classes, non-stuck, quasi-stuck and stuck wheel. The data is then used to train a Support Vector Machine (SVM) ML classification system to be able to differentiate between the three states. The article then presents testing of the system with a four-wheeled rover in a sandbox. The rover is commanded to move into a variety of slip situations and the system is used to classify those situations into the three mentioned classes. The results shown are impressive with a few caveats. Given the design of their sensor suite, only about 30% of the wheel circumference is instrumented and all sensors are clustered in a single patch which creates a blind spot situation for the rest of the wheel. This system also considerably increases the complexity of the wheels of the rover, which may lead to difficult design compromises.

In Bouguelia, Gonzalez, Iagnemma, and Byttner (2017), an unsupervised ML slip classification system is demonstrated. The system was first developed using a single-wheel test bed and was then further demonstrated using a four-wheeled rover in outdoor field tests. Four features are used as the input vector: absolute wheel torque, the variance of the longitudinal acceleration, the variance of the pitch rate, and the variance of the vertical acceleration. The first item is assumed to be collected using motor current since no force/torque (F/T) sensor is identified for the rover platform. The other three items are obtained from an IMU mounted on the structure just behind the wheel's motor, close to the axle. The system first aggregates the time-series data in time period groups of samples. These groups are mentioned to be 50 to 1000+ samples, with performance results varying slightly depending on the time period size. These time period groups are then parameterized in 16 different statistical features. A clustering algorithm is then run on the parameterized data groups to extract two (low slip / high slip) or three (low slip / medium slip / high slip) classes. Finally, given the estimation latency introduced by the first three steps, especially with long sampling time periods, Bayesian tracking is used with the original time-series and with the clusters as seeds to provide faster/real-time tracking of the slip level. The resulting system gives a slip estimation accuracy of up to 86% with two classes and up to 72% with three classes.

This system is based on slip detection at the individual wheel level and requires an IMU to be installed very close to the axle of any wheel where slip tracking is desired. It is not entirely clear if this is a strict requirement. The article include a comparison to other unsupervised systems, which favors this system, and a comparison to supervised methods, which shows supervised methods having the upper hand in performance.

In Gonzalez, Apostolopoulos, and Iagnemma (2018), an unsupervised ML slip classification system based on Self-Organizing Maps (SOM) is presented and its performance is compared with an SVM system. The system is based on the same hardware setup and dataset as Bouguelia et al. (2017) and uses the same four features as inputs, one wheel's motor current and the sliding variance of pitch rate, vertical and longitudinal acceleration measured with an IMU located near the rear right wheel. The system is also evaluated using IMU measurements from the front right wheel and from the center of the rover. It is applied to the same two class and three class slip classifications. It compares the performance of two implementations of the SOM system, semantic SOM and distance-based SOM to two supervised learning system, SVM and Artificial Neural Network (ANN), and one unsupervised learning system, K-means. A moving median filter is also used to better evaluate the performance of the systems with regards to the task of detecting wheel-terrain slip.

The performance of the semantic SOM system on the two class system is almost on par with the SVM system, which boasts the best performance. However, for the three class problem, despite high accuracy, the system's F1 score is significantly lower than the SVM, which again shows the best performance. An analysis of the testing time and storage requirements for all systems is also presented, showing that SVM algorithms have excellent testing time, around 2 s, but require the most storage. The semantic SOM take less storage, but require almost 8 s testing time. This testing time evaluation does not seem to include data acquisition delay or any factors other than computation time. The tests are said to have been ”run on a standard-performance computer (Intel Core i7, 3 GHz, 16 GB RAM, OS X, Matlab R2016b)”. It is also shown that with both the SVM and ANN systems, the IMU placed near the rear right wheel yields better performance than the other two. It should however be noted that their experiment compared two IMUs mounted close to the wheels with another IMU mounted on the middle section of the rover, which seems to be part of the sprung mass of the vehicle given their rocker arm suspension design. This conclusion about ideal sensor placement may not hold true in simple skid-steer rovers with no suspension features.

In Nourizadeh, Stevens McFadden, and Browne (2022), four deep-learning methods are used to estimate whole rover slip. The system is also used to classify slip into three classes to evaluate discrete slip estimation performance. The system are based mainly on Long-Short Term Memory (LSTM), with two of the four also incorporating Convolutional Neural Networks (CNN) and 2 using Auto-Encoders (AE). The systems use IMU data at 100 Hz and wheel encoder data at 10 Hz on a Clearpath Jackal skid-steer rover. The performance of the systems is then shown compared to a number of other systems (AdaBoost (AB), SVM, random forest (RF), decision tree (DT) and ANN). It is worth noting that the performance obtained with SVM and ANN systems seems significantly lower than what was obtained in other reviewed work (Gonzalez, Apostolopoulos, & Iagnemma, 2018). Training, validation and testing were all done on a seemingly homogeneous dataset, which may not show an accurate assessment of generalized performance. Nevertheless, this work does make a good case for the general performance of LSTM systems in this kind of regression and classification application.

Prior Work	Estimator Type	Main Sensors	Predicted variables
(Helmick et al., 2004)	Exteroceptive	VO, WO, IMU PE	3DOF rover slip %
(Gonzalez et al., 2012)	Exteroceptive	VO	3DOF rover slip %
(Cheng et al., 2005)/(Arvidson et al., 2017)	Exteroceptive	VO	3DOF Rover slip %
(Reina et al., 2010)	Combined	VO, WO, Compass	2DOF rover slip %
(Gonzalez & Iagnemma, 2018)	Proprioceptive	MC	Wheel slip flag
(Ojeda et al., 2006)	Proprioceptive	IMU PE, WO, MC	Rover AWS flag
(Reina et al., 2006)	Proprioceptive	GYRO, WO, MC	Rover AWS flag
(Bussmann et al., 2018)	Proprioceptive	WO, IMU	Rover AWS flag
(Omura & Ishigami, 2017)	Proprioceptive	1DOF F sensor	Wheel slip class
(Bouguelia et al., 2017)	Proprioceptive	IMU, MC	Wheel & rover slip class
(Gonzalez, Apostolopoulos, & Iagnemma, 2018)	Proprioceptive	IMU, MC	Wheel & rover slip class
(Gonzalez, Fiacchini, & Iagnemma, 2018)	Proprioceptive	IMU, MC	Wheel & rover slip class
(Nourizadeh et al., 2022)	Proprioceptive	IMU, WO	Wheel slip % and class

Table 2.1: Summary of existing literature on wheel-terrain slip estimation systems for exploration rovers.

2.2 Synthesis of prior literature

Table 2.1 summarizes existing literature on slip estimation systems for exploration rovers. We can note that only one of the listed articles presents a system which does both regression and classification (Nourizadeh et al., 2022) and it does so with a purely proprioceptive method. All other entries in the list can be separated in two categories, slip regression estimation using exteroceptive methods, primarily VO, and slip classification using proprioceptive methods, primarily IMU, MC and WO. The first category naturally accomplishes the slip detection in a more accurate manner, usually by giving a direct estimation of how much distance the rover moved and comparing this value to the WO values. This is usually also beneficial in terms of increasing the localization accuracy of the rover. However, this beneficial feature comes at a significant hardware cost in terms of imaging and computing capabilities. This also means that the VO cycle time tends to be longer, especially on mission hardware, as per table 2.2. The second category however, with slip classification systems, generally has the more modest aim of rapidly detecting the occurrence of elevated wheel-terrain slip events. Since this is accomplished with simpler sensors, the hardware and computing requirements are modest and the estimation latency is considerably lower. Each of these two categories describes valuable and useful slip estimation methods depending on the context in which they would be implemented.

Prior Work	Demonstrated usage	Sensor rate specified	Detection latency
(Helmick et al., 2004)	Lab tested	Unspecified	Unspecified
(Gonzalez et al., 2012)	Field tested	VO: 5 Hz	∼0.5 s*
(Cheng et al., 2005)/(Arvidson et al., 2017)	Mission tested	VO: <0.02 Hz	1-1.5 min
(Reina et al., 2010)	Field tested	VO: 5 Hz	∼0.5 s*
(Gonzalez & Iagnemma, 2018)	Mission tested	MC: Unspecified	20 s
(Ojeda et al., 2006)	Lab tested	Unspecified	Unspecified
(Reina et al., 2006)	Lab tested	Unspecified	Unspecified
(Bussmann et al., 2018)	Field tested	Unspecified	Unspecified
(Omura & Ishigami, 2017)	Lab tested	Unspecified	Unspecified
(Bouguelia et al., 2017)	Field tested	IMU: 100 Hz MC: 40 Hz	>1-5 s*
(Gonzalez, Apostolopoulos, & Iagnemma, 2018)	Field tested	IMU: 100 Hz MC: 40 Hz	∼7.6 s
(Gonzalez, Fiacchini, & Iagnemma, 2018)	Field tested	IMU: 100 Hz MC: 40 Hz	<10 s
(Nourizadeh et al., 2022)	Field tested Field tested	IMU: 100 Hz WO: 10 Hz	∼2 s*

Table 2.2: Summary of existing literature on wheel-terrain slip estimation systems for exploration rovers. *Indicates estimated values, where possible, when no specific figure is provided by the authors.

Considering the systems in use on deployed exploration rovers, the NASA MER and MSL missions are the most successful & long-lived exploration rover missions to date which include such slip estimation systems. Part of this success is owed to the robust VO localization system on which they have relied to detect mobility challenges and prevent worsening entrapment situations. However, heavy reliance on VO comes at a significant cost in terms of onboard computing resources and significantly slows down the average speed at which these rovers travel. Similarly to the VTWD update to Curiosity, the Vision Compute Element (VCE) system implemented for the Mars2020 mission aims to reduce computing time required by the VO system, offloading the computation load on a dedicated FPGA hardware module. However, this new module comes at a significant mass and power cost for Perseverance (Rieber, McHenry, Twu, & Stragier, 2022). Clearly, for safe travels in remote environments, VO has shown its effectiveness. However, this effectiveness comes at a cost and imposes certain travel speed constraints which may not be suitable to all types of rover missions. Indeed, one of the main ongoing challenge to remote exploration using Unmanned Ground Vehicles (UGV) is how to increase the average travel speed without compromising terrain traversal safety. Relying heavily on VO imposes significant design constraints on exploration rovers and may not be suitable for the numerous upcoming micro-rover missions to the Moon.

There is significant motivation and interest in demonstrating effective & low-cost alternatives to vision sensors for slip estimation (Lopez-Arreguin & Montenegro, 2021). Proprioceptive solutions which rely on measuring vibrations generated at the wheel-terrain interface have shown interesting promises in that regard since they may be used with IMU sensors which are expected to be present in the rover design by default.

Significant research has already been accomplished on these types of slip estimation systems. However, as seen in table 2.2, the research described in prior literature often neglects to mention specific requirements for the minimum rate of measurement required for such a system and how reduced sensing rates may impact detection performance. In some works the methodological details do mention the IMU sensing rate, but it usually seems like an arbitrary rate, often 100 Hz. While 100 Hz may or may not be a realistic rate for mission hardware, it also leaves some important questions unanswered. From an implementation point of view, clear knowledge of the performance trade-offs of different sampling rates is quite valuable. This research aims to demonstrate the value of such a trade-off analysis and show a finer picture regarding the performance of an IMU-based proprioceptive slip classification system.

Table 2.2 also provides an idea of the detection latency for these various systems when possible. Given the speed at which most exploration rovers currently traverse their mission environments, these latencies may be reasonable. However, as per the previously mentioned current research challenge regarding increasing the average travel speed without compromising terrain traversal safety, we believe in the value of breaking down and reducing detection latency in such slip estimation systems. This research will aim to describe in detail the key aspects governing detection latency in these systems.

Some implementations also assume specific sensor placement which may not always be practical or necessary in all rover designs. Gonzalez, Apostolopoulos, and Iagnemma (2018) seems to be the only prior work which discusses performance impact of sensor placement but their conclusion may not be applicable to micro-rovers with no significant wheel suspension features. This research aims to show that in such rigid-body rovers, the mounting location of the IMU may not have such a significant impact on the slip detection performance.

Chapter 3

Problem Statement

3.1 Problem Statement

From the literature, it is known that wheel-terrain slip in exploration rovers can be estimated using proprioceptive methods. However, minimal hardware requirements for such systems have not been carefully established. In the context of the upcoming deployments of micro-rover missions on the Lunar surface, which may have limited design flexibility for advanced mobility features with specific or onerous hardware requirements, it would be valuable to know the minimum scope of hardware requirements for such a proprioceptive system. This would help evaluate the feasibility and cost-benefit of implementation for such a slip detection system in mission hardware. Solutions which can provide beneficial features while requiring no more than access to data from baseline sensors would have a significant advantage over solutions requiring extra hardware and/or significant computation. This research plans to implement a machine learning system to detect wheel-terrain slip in a skid-steer rover to evaluate and gain a better understanding of the relationship between slip detection performance and hardware requirements.

3.2 Thesis Statement

This research demonstrates a two-class SVM slip detection system for a skid-steer microrover. The system is based on proprioceptive sensing to avoid the significant computational cost of VO. The system is able to differentiate between low-slip and high-slip events around a 35% threshold within the scope of driving forward on flat or sloped terrain. The system uses short samples of vibration data measured using an IMU to classify slip events. High classification performance is achieved with low sensor sampling rate ($<$50 Hz), short time sampling windows ($<$0.25 s), and short slip estimation latency ($<$1 s). Performance trade-offs of various sampling frequency and sampling window size are discussed in the context of the system being used on a microrover system with limited hardware capabilities (e.g. low frequency IMU sampling and limited computation capability). The system shows equally good performance between flat-ground slip and slope slip.

3.3 Contributions

This research thesis contributes to the field of remote exploration rovers in a few important ways. Specifically, the following contributions are made:

- The development of a novel proprioceptive slip classifier based on frequency domain features in IMU data.
- An analysis of performance dependence on sensor sampling window duration and sampling rate, as well as sensor channel choice.

3.4 Scope

This research is not intended to be a comparison of different proprioceptive methods or classifier systems. It does not claim that the slip classification system presented outperforms any other system presented in related works.

Our system was designed with a single-channel input, to work with a single sensor output channel. This research does not evaluate the performance of multiple-channel input systems, whether or not they outperform single-channel input systems and what an optimal number of sensor input channels might be.

This research does not claim that SVM systems represent an optimal trade-off between performance and computational efficiency. It only asserts that SVMs are one option amongst other good possibilities for this classifier application, with support from prior work in the literature.

This research also does not explore any cutting-edge deep learning ML methods to obtain the maximum performance possible from the sensor measurements. Given the context of microrovers with limited hardware, it was not considered as an appropriate solution to the classification task.

3.5 Publications

Journal article:

J. Li, P. -L. Aubin-Fournier and K. Skonieczny, ”SLAAM: Simultaneous Localization and Additive Manufacturing,” *in IEEE Transactions on Robotics*, vol. 37, no. 2, pp. 334-349, April 2021, doi: 10.1109/TRO.2020.3021241.[1]

Conference oral presentation:

J. Li, P.-L. Aubin-Fournier and K. Skonieczny, ”SLAAM: Simultaneous Localization and Additive Manufacturing,” *in 2021 IEEE International Conference on Robotics and Automation (ICRA)*, 2021[1]

P.-L. Aubin-Fournier and K. Skonieczny, ”Slip estimation from vibrations,” *in Astronautics Conference of the Canadian Aeronautics and Space Institute (CASI ASTRO)*, 2021

P.-L. Aubin-Fournier and K. Skonieczny, ”Vibration-based wheel-terrain slip detection for skid-steer rovers,” *in International Society For Terrain-Vehicle Systems (ISTVS) Americas Symposium*, 2022

Conference poster presentation:

P.-L. Aubin-Fournier and K. Skonieczny, ”Vibration-based wheel-terrain slip detection for skid-steer rovers,” *in ECE Graduate Student Research (GSR) Conference*, 2022 [2]

---

[1] Project and paper are unrelated to the present thesis, based largely on work by an earlier MASc student followed by Capstone work and an NSERC-funded semester research internship. Project was completed in first semester of this MASc.

[2] Won a third place award for best research presentation

Chapter 4

Research Methodology

This chapter covers the detailed methodology relevant to this vibration-base wheel-terrain slip detection project. It begins with the initial induced slip experiments accomplished in our indoor facility. Following the promising results seen in these indoor experiments, an outdoor field test was organized to gather more induced slip test data on flat ground. In the same outdoor field test, slope climbing tests with variable uncontrolled wheel-terrain slip were conducted on both difficult slopes with high slip and easy slopes with low slip. A series of single-wheel induced slip tests using various designs of 3D printed wheels is also presented. Finally, the last section of the chapter describes the steps taken to make a machine learning system that is able to distinguish between high slip and low slip events using only the vibration data measured by the IMU.

4.1 Induced slip tests

In this section the technical details of two different experiments will be described where wheel-terrain slip was artificially induced in a Clearpath Husky skid-steer rover. During a given test case, the Husky's forward linear speed is commanded at a constant value. An opposing force is then applied to the Husky such that the actual forward linear speed of the Husky's physical movement is limited to a constant average speed lower than the Husky's commanded speed. This lower speed is dictated by the desired wheel-terrain slip ratio for the given test case. For these induced slip tests, the measurements of main interest are linear accelerations and angular velocities measured by two IMU sensors.

First, we cover a test campaign which was done in the Aerospace Robotics Lab (ARL) indoor facility on Concordia University's campus, using a robotic gantry to induce slip. Second, we will describe an outdoor field test campaign which was conducted on the Canadian Space Agency's analogue terrain, also know as the "Mars yard", which replicates the geology of the surface of Mars. In these tests, a larger skid-steer rover is used to induce slip in the Husky rover.

4.1.1 Test parameters for the induced slip tests

4.1.1.1 Input: Soil Preparation and Cone Index Gradient

All indoor lab tests conducted in soil simulant were conducted in Glenn Research Center-1 (GRC-1) sandy soil simulant (Oravec, Zeng, & Asnani, 2010). The soil was prepared for testing by loosening with a shovel followed by compaction using a soil tamping tool. To ensure result consistency between test cases, the soil preparation was evaluated. Data on the soil consistency was collected with a RIMIQ CP40II cone penetrometer instrument. Using data gathered with this instrument (Creager, Asnani, Oravec, & Woodward, 2017), the Cone Index Gradient (G) measurement of the soil was calculated using equation 1 (McRae, Powell, & Wismer, 1965). This metric essentially represents the slope of the pressure vs depth required to drive a metal cone vertically through the soil. Low G values correspond to loose soil and high G values correspond to compacted soil.

$$G = \frac{\sum_{i=1}^{n}(d_i - \overline{d})(CI_i - \overline{CI})}{\sum_{i=1}^{n}(d_i - \overline{d})^2} \tag{1}$$

In this equation, n is the number of measurements in an insertion, i is the measurement number, d_i and CI_i are the depth and cone index at point i, respectively, and $\overline{d}$ and $\overline{CI}$ are the mean of all the depth and cone index values measured in the insertion, respectively. The cone index corresponds to the pressure in kPa required to insert the 323mm^2 cone in the soil at a constant speed of 30mm/s.

For the outdoor tests described in section 4.1.3, the soil consisted of regular playground sand. Cone index gradient measurements were done sparsely on the testing area to ensure the ground condition was uniform and roughly equivalent to the compact conditions in the lab. The soil preparation between tests was limited to raking the sand to erase the rover tracks. For outdoor tests no specific loosening or compacting process was used to change the soil conditions.

4.1.1.2 Input: Commanded Rover Speed

When running tests, the rover is commanded to drive forward at a specific speed which will be referred to as the Commanded Rover Speed, V_{cmd}. The control loop for the rover's drive system spins its motor at a constant velocity that would, in ideal terrain conditions, result in the rover moving at the Commanded Rover Speed. This value is given in cm/s and corresponds to the linear speed the rover would achieve in ideal conditions with 0% slip ratio.

4.1.1.3 Input: Actual Rover Speed

The Actual Moving Speed of the rover, V_{act}, is imposed using external mechanical strategies. This results in a rover speed which is lower than the Commanded Rover Speed. The rover's wheels slip against the soil while rotating at the constant angular velocity dictated by the Commanded Rover Speed.

4.1.1.4 Input: Slip

The Wheel-Terrain Slip is calculated from the relationship between Commanded Rover Speed and the imposed Actual Rover Speed using equation 2 (Bekker, 1956)

$$S = \frac{V_{cmd} - V_{act}}{V_{cmd}} * 100\% \tag{2}$$

where S is the slip percentage, V_{cmd} is the Commanded Rover Speed and V_{act} is the imposed Actual Rover Speed.

4.1.1.5 Output: Linear Acceleration

The linear acceleration measured in our tests corresponds to the rate of change of the rover's velocity. The measurement is done along three axes X-Y-Z. +X is aligned with the forward motion of the rover, +Y is pointed to the right side of the rover and +Z is then naturally pointed vertically down. This measurement is captured at 400 Hz using the VectorNav IMU sensor.

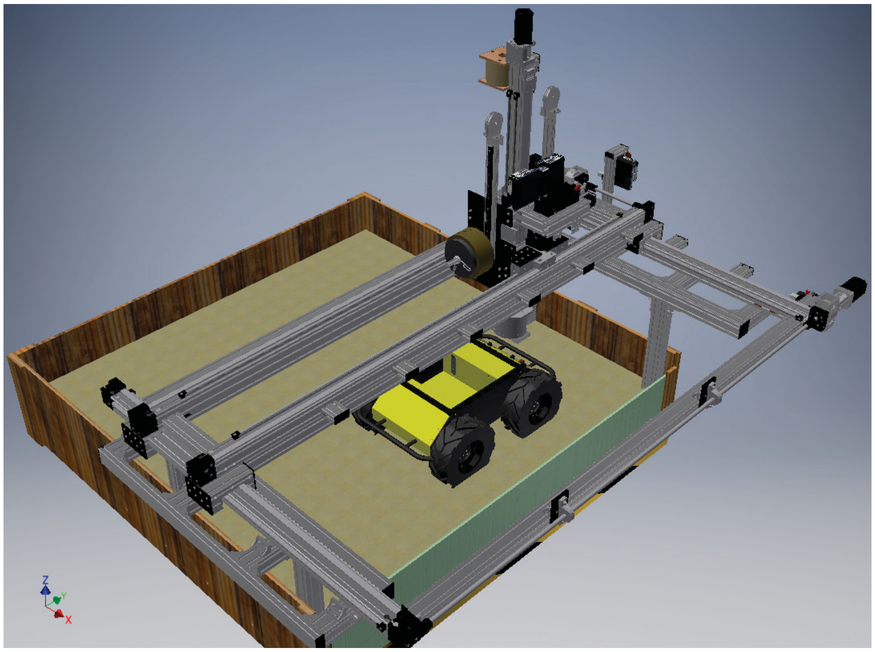

Figure 4.1: CAD of the Husky rover in the sandbox with the gantry (and its coordinate frame) for the induced slip tests.

4.1.1.6 Output: Angular Velocity

The angular velocity measured in our tests corresponds to the rate of change of the angular position of the rover. The measurement is done around the same three axes as the linear acceleration measurements. This measurement is also captured at 400 Hz using the VectorNav IMU sensor.

4.1.2 The indoor ARL experimental setup

Most of the indoor tests were conducted in a large 2.4 m x 2.4 m sandbox situated in the ARL facility. This box is filled up to 20 cm from the bottom of the box with GRC-1 soil simulant (Oravec et al., 2010). In order to ensure repeatable soil conditions, the soil simulant was loosened using a shovel and compacted using a hand tamper between tests. The soil preparation compactness was then verified using the cone penetrometer. Tests were conducted with loose soil conditions at a CI gradient, G, of 4-5 kPa/mm and compact soil conditions at a G of 8-10 kPa/mm.

Above the sandbox, a Macron Dynamics MCS-UC2 4-Dof (XYZTheta) gantry is mounted. The gantry is actuated using AKG Kollmorgen servo motors controlled from a TRIO MC4N-ECAT P901 Motion Coordinator unit. Figure 4.1 shows a CAD diagram of the hardware setup including

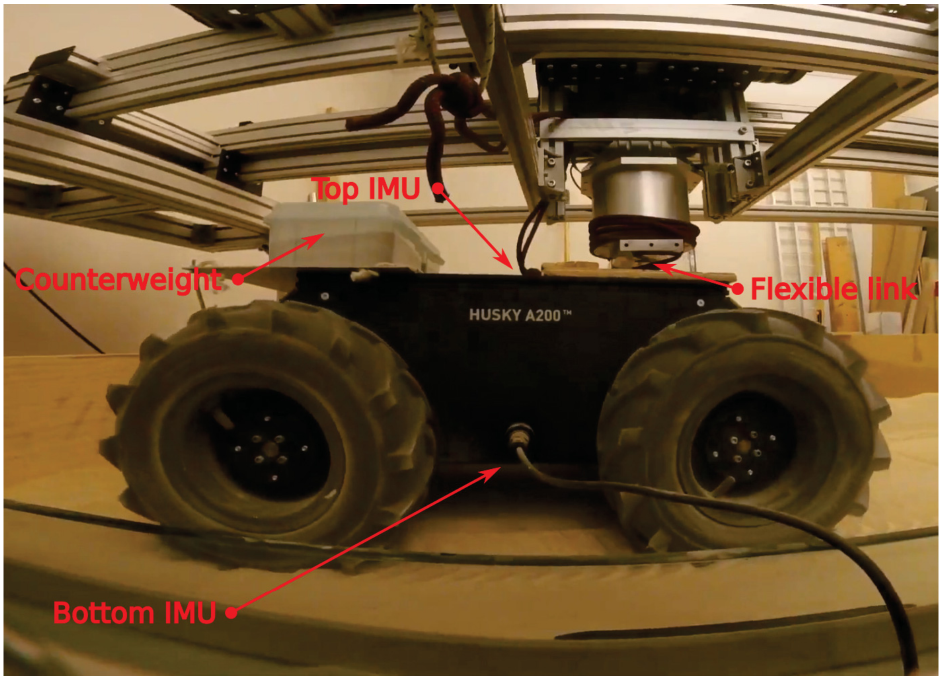

Figure 4.2: Picture of the Husky rover attached to the gantry during testing.

the sandbox, the Husky rover and the gantry system. A strong rope was used to attach the end effector of the gantry to a wooden quick release system installed on the payload structure on top of the Husky. Through this flexible inelastic tension linkage, the Husky was constrained in a single direction along the drawbar pull (i.e. forward driving) axis. This allowed us to precisely reduce the effective movement speed of the Husky using the Y-axis (aligned with the rover's X-axis; see Figure 4.2) of the gantry versus the rover's commanded speed.

During test cases, a collection of python scripts were used to command a constant V_{cmd} linear movement for the rover and simultaneously command movement of the gantry's Y-axis in the same direction at V_{act}. This allowed us to induce specific values of wheel-terrain slip during the Husky's forward linear movement. The Python scripts commanded the gantry using the Trio controller's console interface and commanded the Husky rover by connecting to its onboard computer through SSH using the Paramiko library. SSH commands were then used to activate a simple Robot Operating System (ROS) python script to command the rover's forward motion at V_{cmd}.

Our main interests for data acquisition were 3-axes linear accelerations and angular velocities of the rover. To measure these elements, two VectorNav VN-100 IMU were mounted on the Husky.

Figure 4.3: Satellite picture of the Canadian Space Agency (CSA)'s Analogue Terrain facility, with arrow indicating induced slip testing location (Google, n.d.).

One IMU was mounted on the payload structure located on top of the Husky, roughly above the center of mass of the Husky, identified as IMU1 or top IMU. The other IMU, identified as IMU2 or bottom IMU, was installed on the bottom plate of the Husky's main body using a custom-designed 3D printed bracket, between the front and back wheels, offset to the left side of the rover. This placed the second IMU closer to the center of mass of the rover, giving better measurements for angular velocities. IMU measurements were captured at 400 Hz using the Husky's onboard computer running ROS.

Table 4.1 shows a detailed list of the pertinent induced slip test cases executed in the indoor facility. Most test cases were executed with a nominal V_{cmd} of 5 cm/s which allowed sufficient amounts of data to be captured during each sandbox traverse. Some test cases were executed at a V_{cmd} of 20 cm/s in order to have an equal speed comparison with the outdoor datasets. Datasets were also captured for both loose and compact soil preparations.

4.1.3 The outdoor CSA Analogue Terrain experimental setup

The Canadian Space Agency (CSA)'s Analogue Terrain facility, also known as the Mars Yard, located at the CSA's headquarters in Saint-Hubert, QC, is a carefully designed rover testing facility. Measuring 60 x 120m, the location aims to replicate a Martian environment with different types of geological features such as summits, flagstone patches and craters (Canadian Space Agency, n.d.).

Test ID	Soil condition G (kPa/mm)	Slip (%)	V_{cmd} (cm/s)	V_{act} (cm/s)
A001	Loose (4-5)	10	5	4.5
A002	Loose (4-5)	20	5	4.0
A003	Loose (4-5)	30	5	3.5
A004	Loose (4-5)	40	5	3.0
A005	Loose (4-5)	50	5	2.5
A006	Loose (4-5)	60	5	2.0
A007	Loose (4-5)	70	5	1.5
A008	Loose (4-5)	80	5	1.0
A009	Loose (4-5)	90	5	0.5
A010	Loose (4-5)	100	5	0.0
A011	Compact (8-10)	10	5	4.5
A012	Compact (8-10)	14	5	4.3
A013	Compact (8-10)	15	5	4.3
A014	Compact (8-10)	16	5	4.2
A015	Compact (8-10)	17	5	4.2
A016	Compact (8-10)	18	5	4.1
A017	Compact (8-10)	19	5	4.1
A018	Compact (8-10)	20	5	4.0
A019	Compact (8-10)	30	5	3.5
A020	Compact (8-10)	40	5	3.0
A021	Compact (8-10)	50	5	2.5
A022	Compact (8-10)	60	5	2.0
A023	Compact (8-10)	70	5	1.5
A024	Compact (8-10)	80	5	1.0
A025	Compact (8-10)	10	20	18.0
A026	Compact (8-10)	20	20	16.0
A027	Compact (8-10)	30	20	14.0
A028	Compact (8-10)	40	20	12.0
A029	Compact (8-10)	50	20	10.0
A030	Compact (8-10)	70	20	6.0
A031	Compact (8-10)	80	20	4.0

Table 4.1: Summary of the test cases executed in the indoor test facility.

Figure 4.4: Induced slip test setup, with the large Argo J5 rover restricting the Husky rover using a rope.

Test ID	Soil condition (G value)	Slip (%)	V_{cmd} (cm/s)	V_{act} (cm/s)
A032	Compact (8-10)	10	20	18.0
A033	Compact (8-10)	20	20	16.0
A034	Compact (8-10)	30	20	14.0
A035	Compact (8-10)	40	20	12.0
A036	Compact (8-10)	50	20	10.0
A037	Compact (8-10)	60	20	8.0
A038	Compact (8-10)	70	20	6.0
A039	Compact (8-10)	80	20	4.0
A040	Compact (8-10)	11	20	17.8
A041	Compact (8-10)	12	20	17.6
A042	Compact (8-10)	13	20	17.4
A043	Compact (8-10)	14	20	17.2
A044	Compact (8-10)	15	20	17.0
A045	Compact (8-10)	16	20	16.8
A046	Compact (8-10)	17	20	16.6
A047	Compact (8-10)	18	20	16.4
A048	Compact (8-10)	19	20	16.2

Table 4.2: Summary of the induced slip test cases executed at the outdoor test facility.

For the tests described in this section, the large flat sandy areas were of interest to us. The various slopes found throughout the facility were of interest for the slope testing described in the upcoming section 4.2.

The hardware setup used for the outdoor induced slip tests was similar to the indoor ones. The same Husky rover with two IMUs were used to capture the vibration data at 400 Hz. However, given the lack of gantry on the CSA's installation, we instead opted to use a larger skid-steer rover tied with a rope to the bumpers of the Husky as the constraint on the Husky's motion. The rover in question, an Argo J5 (a prior version of the Clearpath Warthog rover), with approximately six times the mass of the Husky, had no difficulty dictating the effective V_{act} of the overall system.

Similarly to the indoor tests, a collection of Python scripts were used to command linear motion in both rovers simultaneously, with a lower speed for the Argo J5 in order to induce a specific ratio of wheel-terrain slip. As per table 4.2, all outdoor induced slip test cases were executed at a V_{cmd} of 20 cm/s. This was mainly due to limitations of the Argo J5 motor controllers in commanding speeds of less than 4 cm/s.

4.2 Slope tests

The second type of tests accomplished in the CSA's Mars Yard were a series of slope climbs, as detailed in table 4.3 and figure 4.5. The goal of these tests was to generate datasets with variable slip. The Husky rover was placed at the base of the slope facing upslope and commanded with a constant speed forward linear movement. Hill1 through Hill4 sites were selected to provide datasets representing successful and safe slope climb with minimal slip. The Highslope site was selected as an example of a difficult slope with significant slip throughout the climb and a relatively low climb success rate. Indeed, without heading corrections during the climb, only a small fraction of the tests on the Highslope site resulted in a successful climb. When the Husky rover's path deviated too much from the slope's path of steepest ascent, increased amounts of lateral and angular slip appeared as the rover's heading degraded to a lateral slope traverse. The test was thus stopped and the slope ascent was deemed "failed" if either the heading seemed to degrade more than 30 degrees from the projected straight climb path or if the slip degraded all the way to entrapment.

In order to get a value for the wheel-terrain slip experienced by the rover during the climb, a Leica TS16 Robotic total station was used. The total station was installed on a tripod near each slope test location. A target prism was mounted on the Husky rover such that it would stay visible to the total station for the entire test. The total station is then able to dynamically track the position of the target prism at an approximate rate of 5 Hz. In post-processing, the position data obtained from the total station is filtered using interpolation with the help of MATLAB code from a prior research project (Fiset, 2019). The MATLAB code was previously developed to correct data strictly along the X-Y plane, so it was modified to take into account the 3D nature of the slope tests. The modified code was then used to estimate the rover's forward velocity. An estimation of the wheel-terrain slip ratio was then obtained using this velocity estimation and the commanded forward speed in equation 2.

4.2.1 Test parameters for the slope tests

Some of the test parameters defined in section 4.1.1 apply to the slope test. For the inputs, one notable distinction is the slip which becomes an output in the slope tests rather than its previous condition as an input in the induced slip tests.

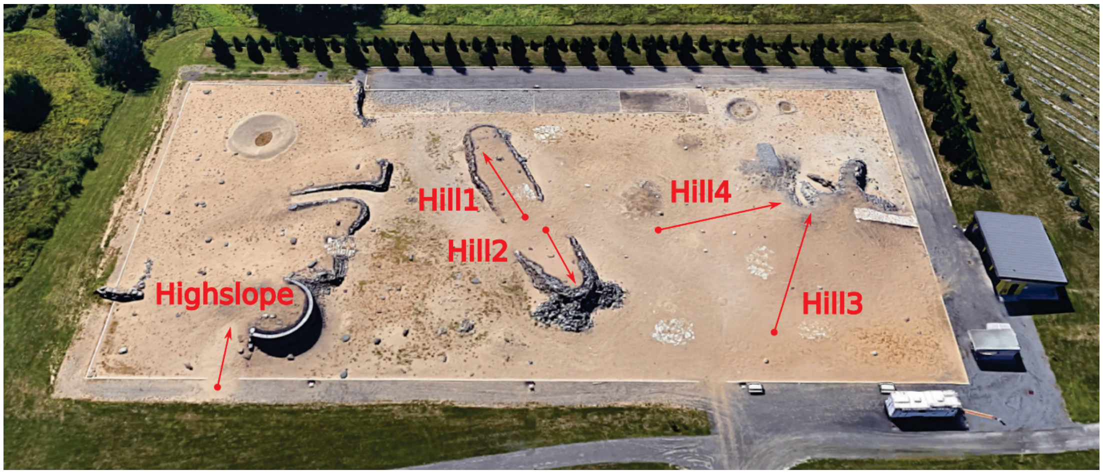

Figure 4.5: Satellite picture of the CSA's Analogue Terrain facility, with arrow indicating slope testing locations (Google, n.d.).

4.2.1.1 Input: Commanded Rover Speed

Similarly to the prior description in section 4.1.1.2, V_{cmd} was commanded as a fixed value. In the case of the slope datasets, the rover was sometimes commanded manually using the controller and sometimes commanded using a simple ROS python script for constant speed forward linear movement. Both solutions resulted in the same rover behavior.

4.2.1.2 Output: Rover position

The Husky rover's position is measured using the Leica TS16 Robotic total station. A tracking reflector prism was installed on the rover and the total station's automated tracking functionality was used to obtain position data at an approximate rate of 5 Hz.

4.2.1.3 Output: Rover slip

The Husky rover's wheel-terrain slip ratio was estimated using the position data measured by the total station. The position data was first filtered and any missing points are interpolated using previously developed code (Fiset, 2019). The code was modified to upgrade it from a 2D assumption to a full 3D capability. Then, the position data is differentiated to obtain an estimation of the V_{act}. This velocity estimation is then used in equation 2 to obtain an estimation of the rover's wheel-terrain slip ratio.

Test ID	Test location & ID	Slip	V_{cmd} (cm/s)	Rover speed
B001	Highslope_b	High	20	Variable
B002	Highslope_c	High	20	Variable
B003	Highslope_d	High	20	Variable
B004	Highslope_e	High	20	Variable
B005	Highslope_f	High	20	Variable
B006	Highslope_g	High	20	Variable
B007	Highslope_h	High	20	Variable
B008	Highslope_j	High	20	Variable
B009	Highslope_k	High	20	Variable
B010	Hill1_a	Low	20	Variable
B011	Hill1_b	Low	20	Variable
B012	Hill1_c	Low	20	Variable
B013	Hill1_d	Low	20	Variable
B014	Hill1_e	Low	20	Variable
B015	Hill2_a	Low	20	Variable
B016	Hill2_b	Low	20	Variable
B017	Hill2_c	Low	20	Variable
B018	Hill3_a	Low	20	Variable
B019	Hill3_b	Low	20	Variable
B020	Hill3_c	Low	20	Variable
B021	Hill3_d	Low	20	Variable
B022	Hill3_e	Low	20	Variable
B023	Hill4_a	Low	20	Variable
B024	Hill4_b	Low	20	Variable
B025	Hill4_c	Low	20	Variable
B026	Hill4_d	Low	20	Variable
B027	Hill4_e	Low	20	Variable

Table 4.3: Summary of the slope slip test cases executed at the outdoor test facility.

4.2.1.4 Outputs: Linear Acceleration and Angular Velocity

IMU outputs were again collected as before, as described in sections 4.1.1.5 and 4.1.1.6.

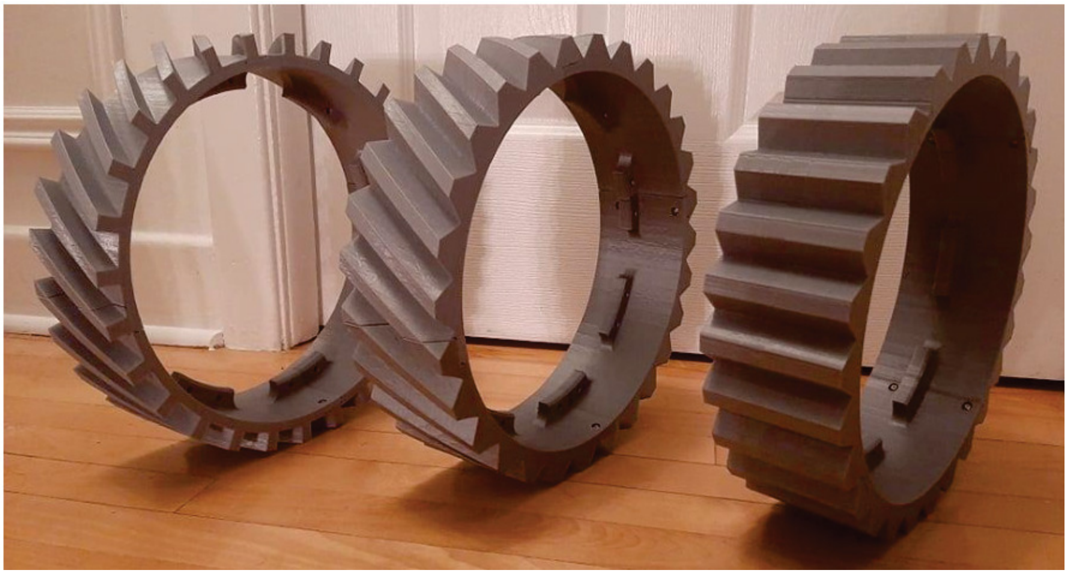

Figure 4.6: 3D printed wheels with different grouser designs.

4.3 Comparative wheel tests

In the context of a separate research project, three wheels were designed and manufactured using Fused Filament Fabrication (FFF) 3D printing. The three wheels had different grouser designs, as shown in figure 4.6. The first wheel from the left has Slanted Rectangular (SLR) grousers. The second wheel, in the middle, has Slanted Trapezoidal (SLT) grousers. The third wheel, on the right, has Straight Trapezoidal (STT) grousers.

As a second part of this separate project, the comparative performance of these wheels was evaluated in the same indoor sandbox facility mentioned earlier. This was done using a single wheel testing system shown in figure 4.7. In this system, the wheel was mounted to a bracket with a motor and transmission assembly to provide mechanical power. The bracket was mounted to a 6-DOF F/T sensor to measure the forces on the wheel. This sensor was then mounted in a 4-bar mechanism to allow vertical movement with minimal friction to obtain consistent wheel loading over a large range of sinkage depths (Daca et al., 2022).

Opportunistically, we chose to record vibration data for some of these performance tests. The same VectorNav IMU used in the induced slip tests with the Husky was installed on the part of the 4-bar mechanism to which the wheel and the motor assembly were attached. To keep the data collection system identical, the Husky rover was installed in the sandbox near the single wheel

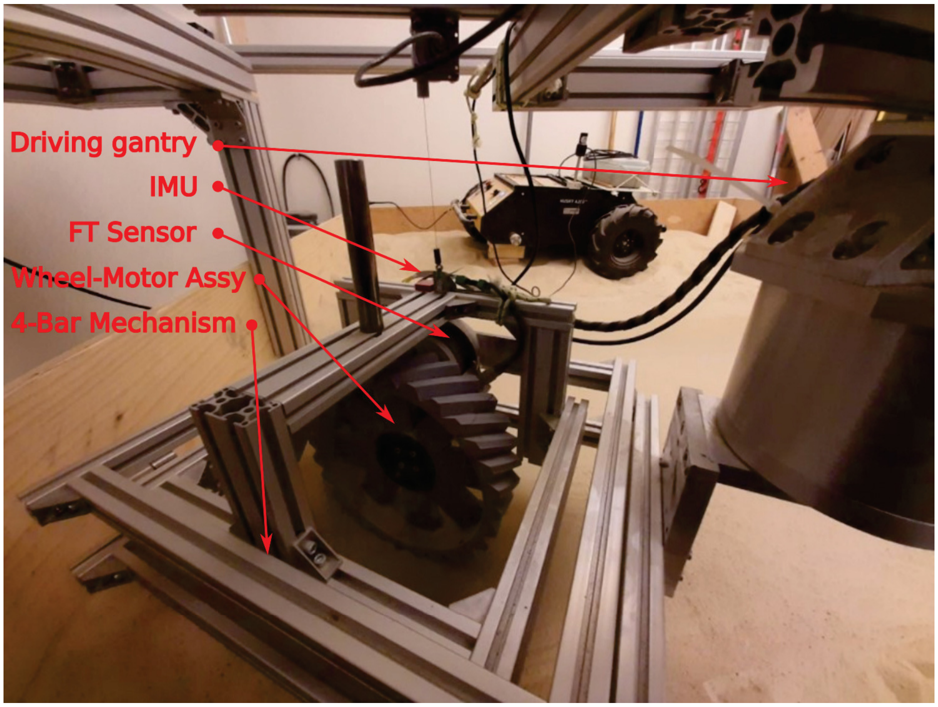

Figure 4.7: Single wheel testing testbed.

testing area and the Husky's onboard computer was used to collect the vibration data at 400 Hz.

The wheels were evaluated at various slip values and slip angle values with a few different goals in mind. The slip angle corresponds to the angular difference between the direction in the which the wheel points and the direction in which it moves. As per table 4.7, a series of single wheel tests were conducted using one of the Husky rover's inflated rubber wheels in order to validate whether or not the vibrations produced in the single wheel testbed were equivalent to what was seen on the full Husky rover tests. As per table 4.4, the tests aimed to evaluate the performance of slanted grousers depending on their orientation to the wheel movement. Correspondingly, we aimed to evaluate if the orientation had a impact on the amount of vibrations generated. The tests detailed in tables 4.5 and 4.6 were done to see if specific grouser designs made a difference in the vibrations generated.

4.3.1 Test parameters

4.3.1.1 Input: Commanded Rover Wheel Speed

The rover wheel speed was commanded to the same value throughout the tests.

Test ID	Slip Ratio (%)	Slip Angle (degree)
SLR-1.1C	0	0
SLR-2.1C	20	0
SLR-3.1C	40	0
SLR-4.1C	60	0
SLR-5.1C	0	15
SLR-6.1C	20	15
SLR-7.1C	40	15
SLR-8.1C	60	15
SLR-9.1C	0	30
SLR-10.1C	20	30
SLR-11.1C	40	30
SLR-12.1C	60	30
SLR-5.1D	0	-15
SLR-6.1D	20	-15
SLR-7.1D	40	-15
SLR-8.1D	60	-15
SLR-9.1D	0	-30
SLR-10.1D	20	-30
SLR-11.1D	40	-30
SLR-12.1D	60	-30

Table 4.4: Summary of the single wheel test cases executed with the wheel with Slanted Rectangular grousers.

4.3.1.2 Inputs: Imposed Actual Wheel Speed and Slip

As per section 4.1.1.3, the actual wheel speed was imposed using the robotic gantry mounted above the sandbox testbed. The speed was calculated using the slip angle in order to result in specific slip ratios along the X-axis of the wheel.

4.3.1.3 Outputs: Linear Acceleration and Angular Velocity

IMU outputs were again collected as before, as described in sections 4.1.1.5 and 4.1.1.6.

Test ID	Slip Ratio (%)	Slip Angle (degree)
SLT-5.1D	0	15
SLT-5.1D	0	15
SLT-6.1D	20	15
SLT-7.1D	40	15
SLT-8.1D	60	15
SLT-9.1D	0	30
SLT-10.1D	20	30
SLT-11.1D	40	30
SLT-12.1D	60	30

Table 4.5: Summary of the single wheel test cases executed with the wheel with Slanted Trapezoidal grousers.

Test ID	Slip Ratio (%)	Slip Angle (degree)
STT-1.1C	0	0
STT-2.1C	20	0
STT-3.1C	40	0
STT-4.1C	60	0
STT-5.1C	0	15
STT-6.1C	20	15
STT-7.1C	40	15
STT-8.1C	60	15
STT-9.1C	0	30
STT-9.1C	0	30
STT-10.1C	20	30
STT-11.1C	40	30
STT-12.1C	60	30

Table 4.6: Summary of the single wheel test cases executed with the wheel with Straight Trapezoidal grousers.

Test ID	Slip Ratio (%)	Slip Angle (degree)
HUS-1.1	0	0
HUS-2.1	20	0
HUS-3.1	40	0
HUS-4.1	60	0
HUS-5.1	0	15
HUS-6.1	20	15
HUS-7.1	40	15
HUS-8.1	60	15
HUS-9.1	0	30
HUS-10.1	20	30
HUS-11.1	40	30
HUS-12.1	60	30

Table 4.7: Summary of the single wheel test cases executed with the Husky rover wheel.

4.4 Slip classification system

A key goal of this research is to develop a slip classification system. As per chapter 3, the system should also be robust and have frugal processing requirements. A modest classifier tool would be a linear classifier. However, to obtain satisfactory performance with such a classifier, the data being classified needs to be linearly separable. A more robust option would be an SVM system since it can handle situations where the boundary between classes is non-linear. SVMs have been shown to be quite popular and effective for a large variety of classification problems. They perform well with low sample sizes and have a low risk of overfitting (Pisner & Schnyer, 2020). As per our literature review in chapter 2, prior work on proprioceptive terrain classification has made use of SVMs to analyse vibration data (Brooks & Iagnemma, 2012). We chose to use the Support Vector Classification (SVC) module in Scikit-Learn's SVM python software library (*SciKit-Learn: SVM module*, 2022). Given that the size of our feature vector is generally smaller than the number of data samples we have, we chose to use the Gaussian Radial Basis Function (RBF) kernel for our classifier, making it a non-linear SVM. This may result in higher processing time, but should result in higher performance compared to a linear SVM (Hsu, Chang, Lin, & others, 2003).

4.4.1 SVM algorithm

The algorithm of the SVM seeks to define a hyperplane which separates the two classes of the samples with the maximum margin (Cortes & Vapnik, 1995). With training samples $x_i \in \mathbb{R}^p$, defined in two classes by $y \in \{1, -1\}^n$, the algorithm will find the coefficient vector $w \in \mathbb{R}^p$ and $b \in \mathbb{R}$ such that $\text{sign}(w^T \phi(x) + b)$ gives a correct prediction. These values are minimized according to equation 3, where ζ_i is the distance between a sample and the correct margin boundary, acting as a penalty term. The term C thus controls the strength of this penalty (*SciKit-Learn: SVM module*, 2022).

$$\begin{gathered}\min_{w,b,\zeta} \frac{1}{2} w^T w + C \sum_{i=1}^{n} \zeta_i \\ \text{subject to } y_i(w^T \phi(x_i) + b) \geq 1 - \zeta_i, \\ \zeta_i \geq 0, i = 1, ..., n\end{gathered} \tag{3}$$

$$\begin{aligned} &\min_{\alpha} \frac{1}{2}\alpha^T Q\alpha - e^T\alpha \\ \text{subject to } &y^T\alpha = 0 \\ &0 \leq \alpha_i \leq C, i = 1, ..., n \end{aligned} \tag{4}$$

$$\sum_{i \in SV} y_i \alpha_i K(x_i, x) + b, \tag{5}$$

Equation 4 defines the minimization problem for the dual coefficients vector α_i. With e being the vector of all ones and Q is an n by n positive semidefinite matrix $Q_{ij} \equiv y_i y_j K(x_i, x_j)$, where $K(x_i, x_j)$ corresponds to the kernel function. In our case, the RBF kernel function is used, defined as $K(x, y) = exp(-\gamma ||x - y||^2)$, where gamma is an hyperparameter that controls the shape of the decision boundary. Equation 5 then represents the decision function, where the sign of the result corresponds to the predicted class (*SciKit-Learn: SVM module*, 2022).

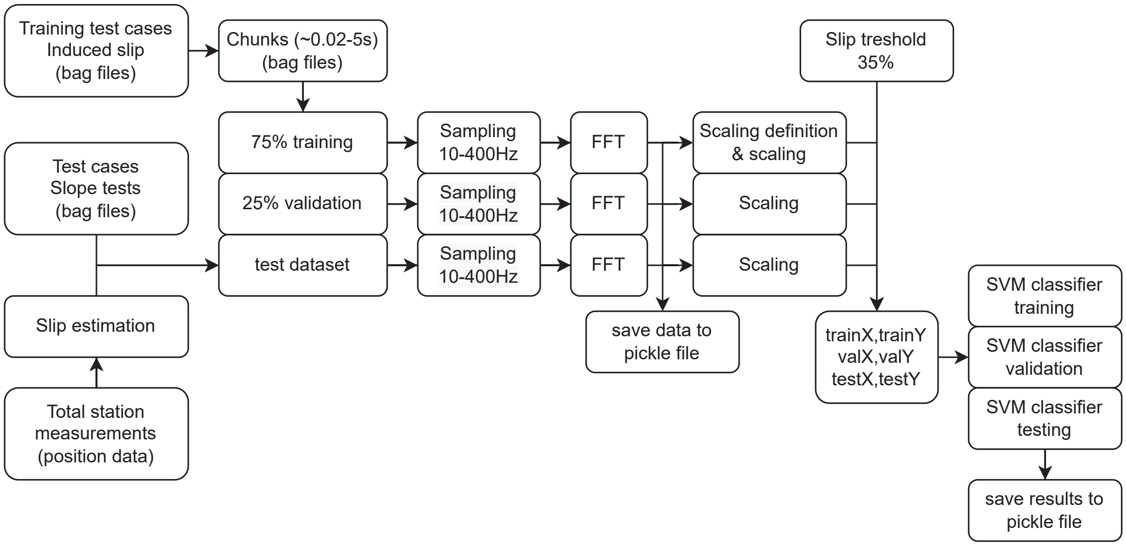

Figure 4.8: Block diagram showing an overview of the SVM training, validation and testing process.

4.4.2 Training, validation and testing SVM system

The overall process used to train, validate and test our SVM system is shown in figure 4.8. The classifier is trained and validated using labeled data from the induced slip datasets, and later tested on slope test data. The induced slip vibration datasets are broken down into short chunks of 0.02-5 s of data. These chunks are then randomly partitioned as 75% training data and 25% validation data. The data in the chunks is then sampled at different rates and converted to the frequency domain using a Fast Fourier Tranform (FFT). A single sensor input type from the IMU is used to train the classifier. The size of our feature vector is thus determined by the sampling window times the sampling rate, divided by two (because of the FFT). For example, a 100Hz sample rate for 0.5 s yields a feature vector of length 25. A floor operation is added to correctly handle sampling frequencies which would result in decimals. As per the following equation:

$$n = \left\lfloor \frac{w_s * F_s}{2} \right\rfloor \tag{6}$$

where n is the amount of system input features, w_s is the sampling window duration, and F_s is the sampling frequency.

With this training data, a scaling rule is defined and applied such that the mean is removed and the data is scaled to unit variance by dividing all the values by the standard deviation. The resulting scaled data from the training dataset is then used to train the classifier using a slip threshold to separate cases of acceptable low slip and cases of undesirable high slip. The boundary between these two classes is set at 35%. Prior work set 30% as the boundary between low slip and medium slip which corresponds to the types of slip we are looking to differentiate in this research (Bouguelia et al., 2017). The threshold is adjusted up by 5% to fall between 30% and 40% induced slip tests and this also gave the training dataset a good balance between the two slip classes with approximately 40% of the dataset being above 35%. Once the classifier is trained, its performance could be evaluated using the validation data. To test the classifier with test data from the slope tests, the estimation of the rover's wheel-terrain slip ratio calculated using the total station's position measurement is used. The same sampling, FFT and scaling process is applied to the data before using the trained classifier.

4.4.3 Parameter performance analysis

In order to improve the effectiveness of our system, sampling rate, sampling window duration and sensor stream choice are varied and the classification performance is evaluated using the validation data. To reduce the impact of random training/validation selection noise, the system is run repeatedly with fresh random selections of training and validation data. The results of these iterations are then averaged to obtain a more accurate evaluation of the chosen parameters.

The IMU used for this project is a standard 6-DOF IMU, consisting of a combination of a 3-DOF accelerometer and a 3-DOF gyroscope. Two of these IMUs are used, such that our measured data has 12 channels. Each of these measurements are used individually to train, validate and test the SVM classifier.

The sampling window duration is varied between 0.02 s to 5 s in order to evaluate its impact on classification performance.

Finally, the sampling rates are varied between 4 Hz and 400 Hz. The lower end being an exploration of the minimum sampling rate at which our system would work and the higher being the maximum stable sampling rate of our IMU instrument.

Chapter 5

Results

5.1 Induced slip test results

This section provides an overview of induced slip test results. These provide a basis for understanding the phenomena being studied, and produce training data for the eventual classifier.

5.1.1 Indoor ARL experimental setup

Induced slip test data in our indoor facility demonstrates that significant vibrations happen during induced slip events. More specifically, we found that the linear acceleration in the z-axis is the sensor output which sees the largest vibration amplitude. The Root Mean Square (RMS) magnitude of the vibrations shows an interesting relationship between the amount of slip and the vibration magnitude, as seen in Figure 5.1. Vibration amplitude for the indoor test data increases with rising slip until about 40%, at which point it begins to fall back down again. The data from tests conducted at a speed of 20 cm/s show significantly more vibration than those at 5 cm/s.

Looking at the vibrations in the frequency domain using FFT in figure 5.2, we can see that most of the vibration energy associated with elevated slip is concentrated in a narrow frequency band between 15 Hz to 18 Hz. This remains true across commanded test speeds of 5 cm/s and 20 cm/s despite the difference in vibration magnitude. This suggests that this particular output, linear accelerations in the z-axis, could have good performance for the classification task. This is reinforced by the fact that prior work has used this output successfully for their vibration-based slip

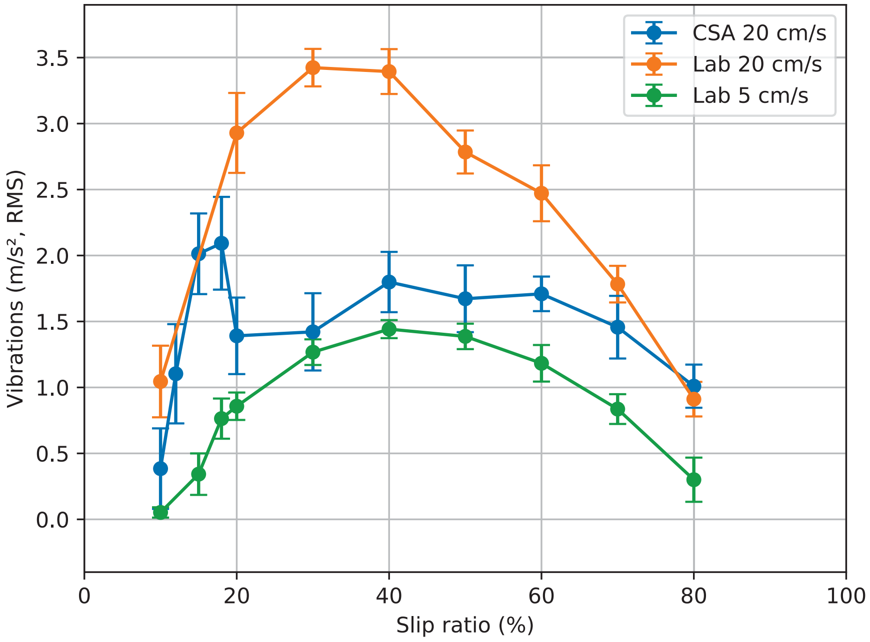

Figure 5.1: Magnitude of vibrations measured during the induced slip tests in our indoor facility according to slip %, calculated from 100 Hz data with 1.00 s sampling window.

classifier. They also mention that performance is less at lower speeds, possibly because the Signal-to-noise ratio (SNR) for vibrations caused by the slip phenomena is low (Bouguelia et al., 2017; Gonzalez, Apostolopoulos, & Iagnemma, 2018; Gonzalez, Chandler, & Apostolopoulos, 2019). We can also note that the majority of the vibrations which seem to be associated to elevated slip happen in lower frequencies, below 50 Hz. Higher frequencies, above 100 Hz, seem to have very few significant features. Overall, visual comparison of the frequency spectrum between the two IMUs (top and bottom) shows little difference except for the angular velocity around the x-axis, as per figures A.11 and A.12.

5.1.2 Outdoor CSA experimental setup

The induced slip test data from our outdoor field test campaigns at the CSA's Mars yard resulted in slightly different results to what was seen in the lab experiments. As per figure 5.1, the RMS magnitude of the vibrations seen in the outdoor experiments increases sharply from 10% to 15% slip, peak at 18% and drop down significantly for 20% and above. The terrain conditions were slightly different with the soil of the Mars yard being composed of regular playground sand rather

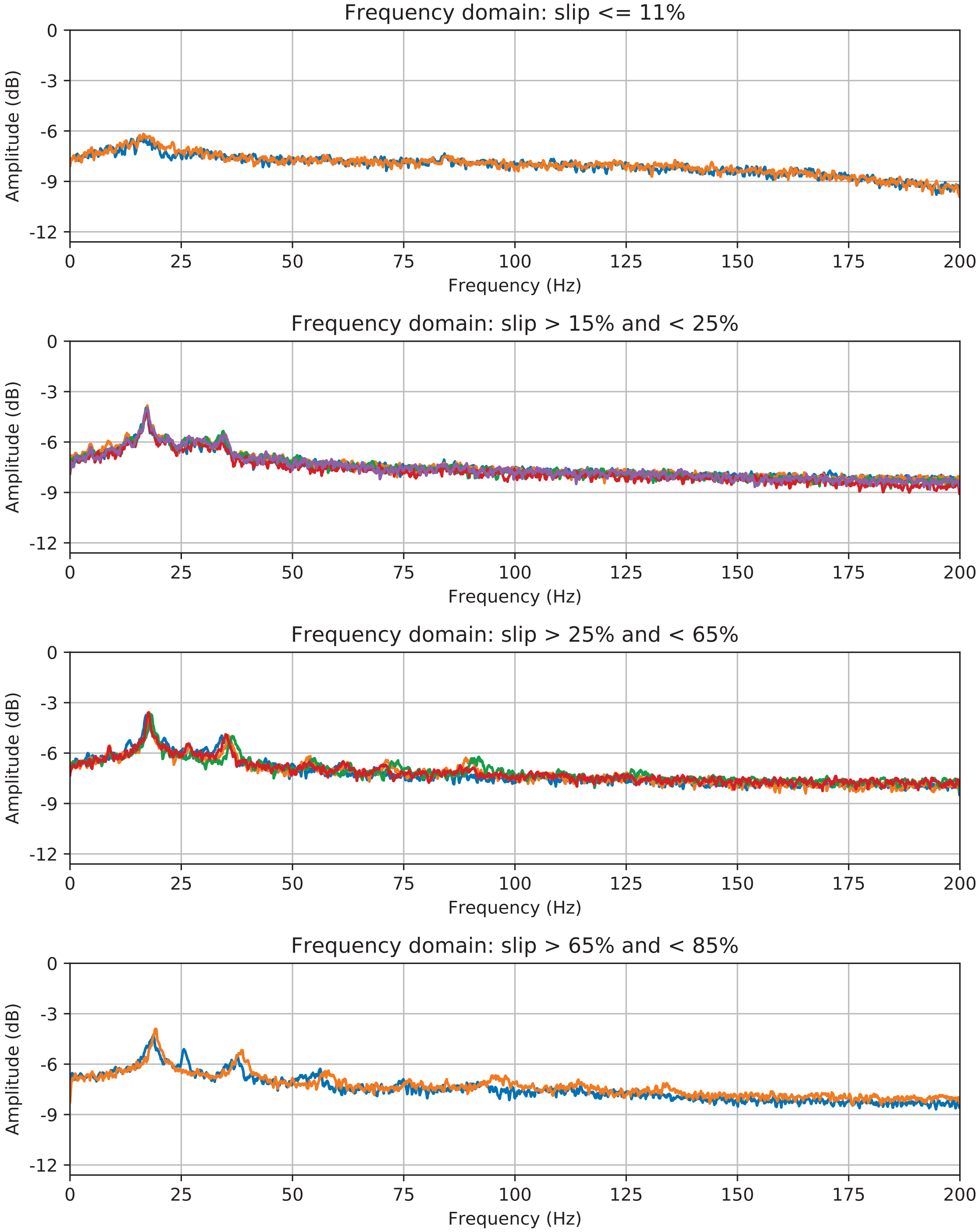

Figure 5.2: Frequency spectrum of vibrations in z-axis linear acceleration measured during induced slip tests at 5 cm/s in our indoor facility separated according to slip %.

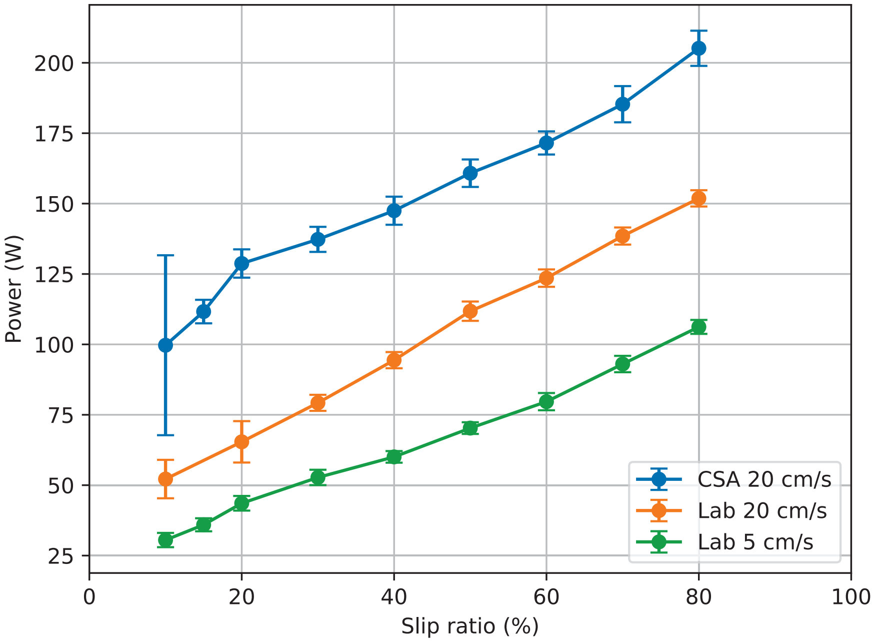

Figure 5.3: Motor power measured during the induced slip tests at the CSA's outdoor facility according to slip %.

than GRC-1 soil simulant. The humidity of the soil was also a significant factor, only the top few cm of the Mars yard being dry. One effect of this is the significantly higher electrical power consumption of the rover motors in this context, as per figure 5.3. Our experiment did not measure drawbar-pull force exerted by the Husky rover, but it seems clear that the humid terrain of the Mars yard offered better traction than the dry GRC-1 in our indoor facility, resulting in higher wheel torque required to achieve the same slip %.

The frequency spectrum of the vibrations in linear acceleration along the z-axis can be seen in figure 5.4. We can see that the low frequency peaks are similar to what is seen in the in the previously mentioned figure 5.2. Given the difference in rover speed, the magnitude of the vibrations is greater and significant vibration can be seen even a low slip values. We can also see slightly more harmonic peaks at elevated slip values. Nevertheless, there is a clear difference between the curves at different slip values which shows promise for SVM classification performance.

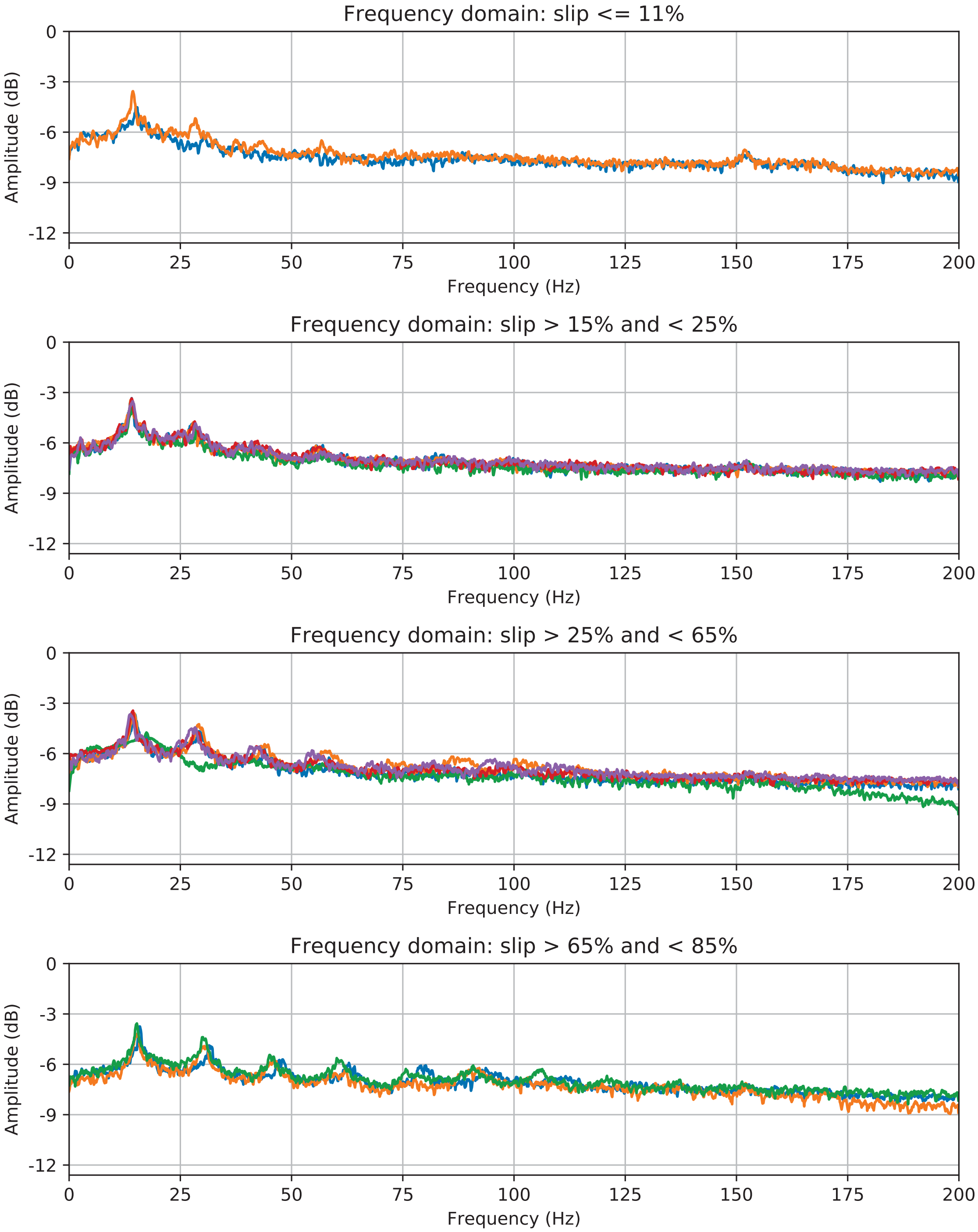

Figure 5.4: Frequency spectrum of vibrations in z-axis linear acceleration measured during induced slip tests at 20 cm/s at the CSA's outdoor facility separated according to slip %.

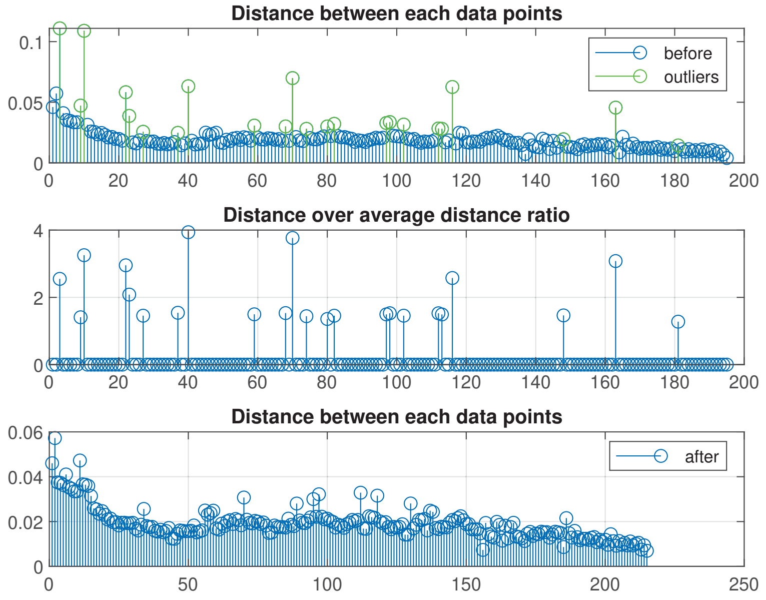

Figure 5.5: Example of the original output of the velocity correction MATLAB script with test B003 Highslope_d.

5.2 Slope slip tests

5.2.1 Slip analysis

As per section 4.2, the slope tests resulted in variable slip. The ground truth position of the rover was measured by the Total Station and post-processed in MATLAB to obtain an estimation of the rover's linear velocity, as shown in Figure 5.7. The MATLAB script previously developed to interpolate the readings from our total station instrument was designed for 2D motions with minimal slip. As such, it did not perform so well with 3D paths where high slip was present. Multiple outlier distances between measured positions are undetected by the script and remain in the ”corrected” data, as per figure 5.5. With a few corrections to properly consider the more complex rover path, more distance outliers are corrected properly, as per figure 5.6. The resulting path is then used to more accurately estimate V_{act}. Based on this V_{act} estimation, an estimation of rover slip is made.

The vibration data measured with the IMU is then be related to the estimated slip ratio and plotted as per figures 5.8 and 5.9. From these plots, we can see that the vibration magnitude vs slip

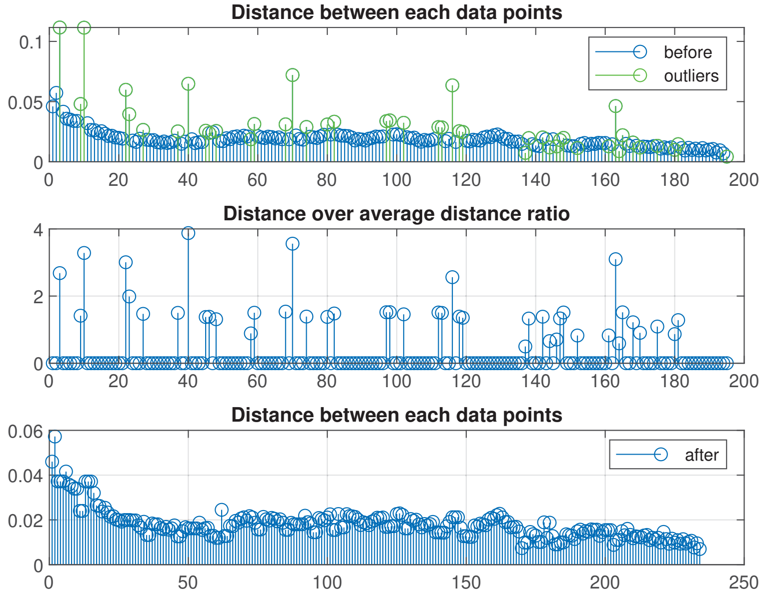

Figure 5.6: Example of the output of the velocity correction MATLAB script with test B003 Highslope_d after it was updated to consider high slip and a 3D rover path.

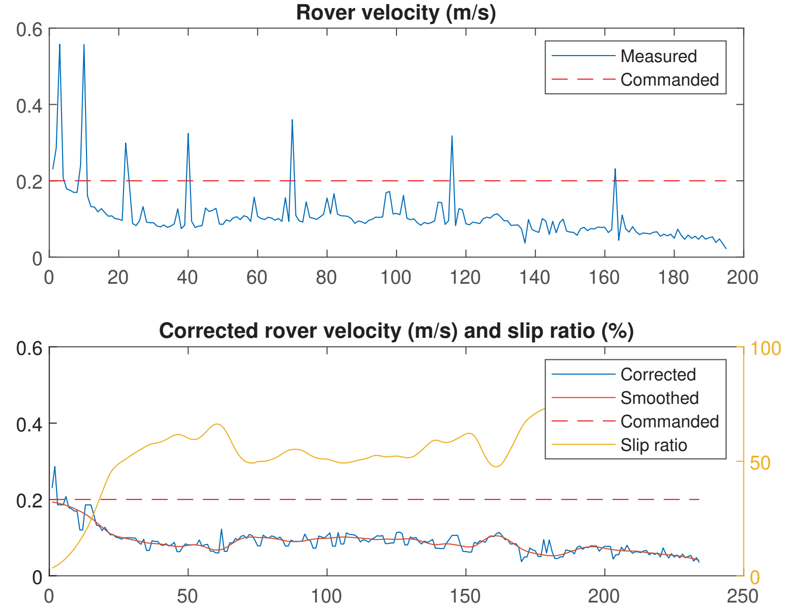

Figure 5.7: Example of the output of our velocity correction and slip estimation MATLAB script.

ratio seen during the slope tests is similar to what is seen in the induced tests, rising on average until slip is approximately 40%, then plateauing or perhaps falling. However, we can note the absence of peaking vibrations at around 18% slip, as seen in figure 5.1 for the outdoor test data. The data is also quite noisy. The noise could be explained by variability in the vibrations due to varying terrain conditions during the slope ascent. We can also note that the standard deviation of the noise in figure 5.9 is significantly higher, indicating the impact of a shorter sampling window on noise. The noise could also be from the slip estimation process. While the Total Station instrument is very accurate when measuring the precise positions of the target prisms at significant ranges, it does not provide accurate timestamps for its measurements and the approximately 5 Hz acquisition rate is not consistent. This introduces noise in the velocity estimation despite the interpolation done by our MATLAB software. Other researchers have found that global navigation satellite system (GNSS) Real-time kinematic positioning (RTK) systems provided more reliable ground truth data for rover field tests compared to Total Station instruments (Gonzalez, Apostolopoulos, & Iagnemma, 2018).

Finally, we can also note the large disparity in vibration magnitude between the high slip slope tests and the low slip slope tests. While we do not have a definite answer to explain this difference, a few possible factors can be mentioned. First, the two sets of tests were done on different days, approximately two months apart, with different weather conditions. This may have led to slightly different soil parameters, leading to different vibrations from the wheel-terrain interaction. Otherwise, the angle at which the rover was climbing the slopes was different between the sites. This may have had an impact on the magnitude of the z-axis linear acceleration. Finally, it is possible that the terrain parameters of the slopes are not entirely uniform. In any case, despite the unknown reason behind this discrepancy, we can say that it does not look like a linear classifier would perform well with this data, especially with short sampling windows like 0.25 s.

It is also interesting to take a look at the vibration magnitude for a different sensor stream such as the z-axis angular velocity. Here, as per figure 5.10, the magnitude of the vibrations is lower than in the z-axis linear acceleration by about two orders of magnitude. However, there is a regular progression of magnitude increasing with slip, with peaks around the 60% slip region. The slope slip plots for the high and low slip tests in figure 5.11 are also much more aligned, meaning low slip ratios exhibit similar vibration response regardless of context, which should result in better classification performance.

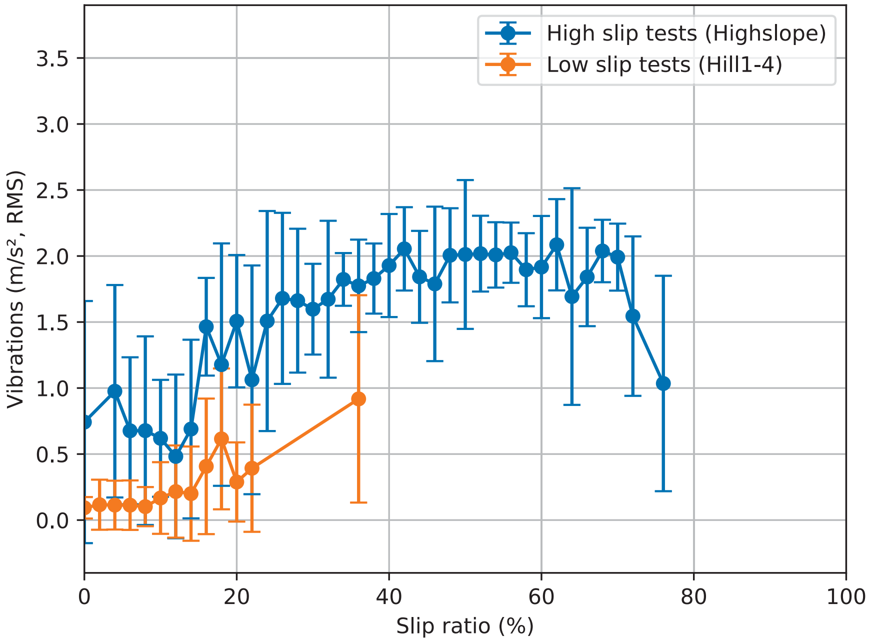

Figure 5.8: Magnitude of vibrations measured in the z-axis linear acceleration during the slope tests according to slip %, sampled at 100 Hz and averaged over 1.00 s windows.

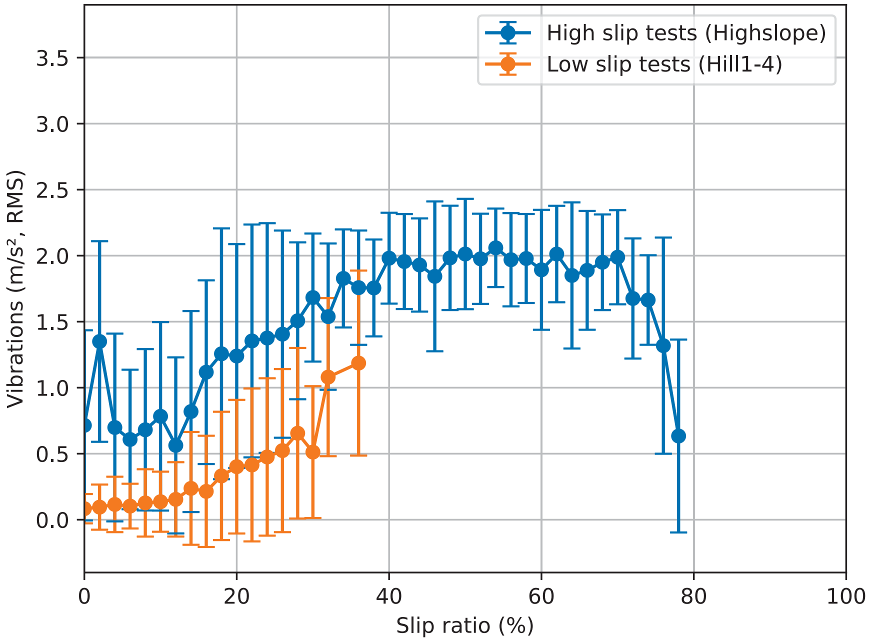

Figure 5.9: Magnitude of vibrations measured in the z-axis linear acceleration during the slope tests according to slip %, sampled at 100 Hz and averaged over 0.25 s windows.

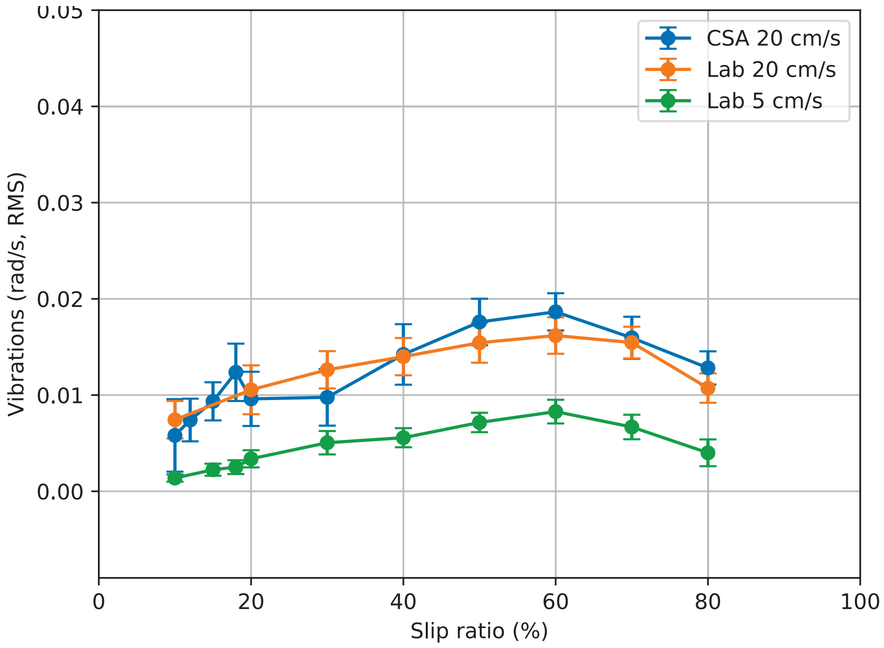

Figure 5.10: Magnitude of vibrations measured in the z-axis angular velocity during the induced slip tests according to slip %, sampled at 100 Hz and averaged over 0.25 s windows.

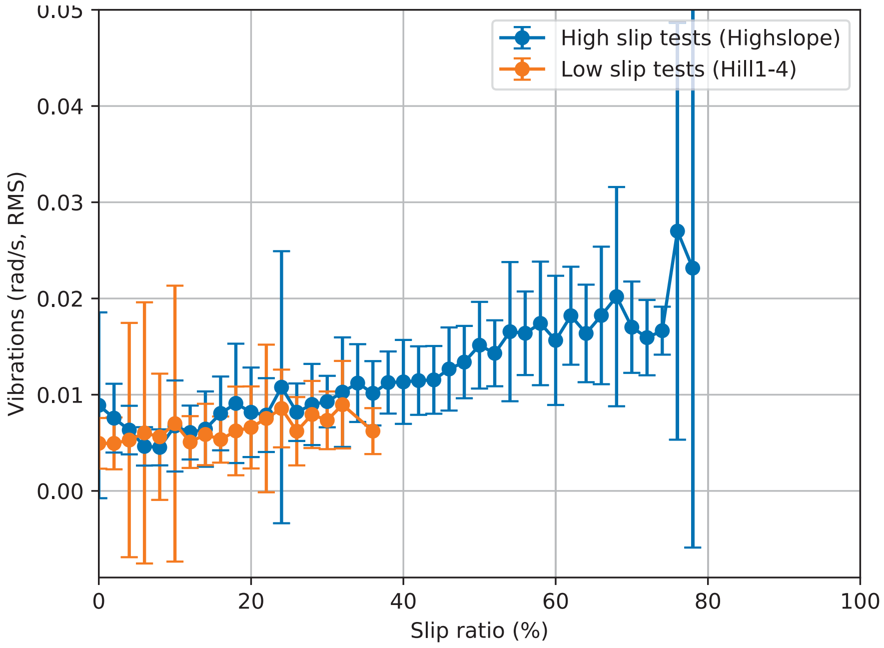

Figure 5.11: Magnitude of vibrations measured in the z-axis angular velocity during the slope tests according to slip %, sampled at 100 Hz and averaged over 0.25 s windows.

5.3 SVM system training and validation results

Initially, some proof-of-concept work was done using the induced slip datasets collected in our indoor facility. These tests showed that the vibrations associated to different slip levels collected on our system could be used to train an SVM classification system. The validation part of the dataset showed that the SVM system was able to properly classify the two slip classes with high accuracy. However, the limited size of the sandbox in our indoor facility resulted in a limited amount of data per test, especially for the tests where V_{cmd} was set to 20 cm/s. Properly preparing the soil between tests and moving the Husky rover in and out of the test area was also prohibitively time consuming. A slope test dataset could also have been generated in our indoor facility thanks to the hydraulic tilt table installed below our sandbox. However, given the opportunity to field test at the CSA's outdoor facility, it was considered a better use of resources to focus entirely on creating and using those datasets. Henceforth, the datasets from the CSA's outdoor facility are used as seen in tables 4.2 and 4.3 are used for training, validation, and testing of the SVM system. As mentioned in section 4.4.2, from these datasets parameter performance evaluation can be done. As per section 4.4.2, the high and low slip classes are defined around the 35% slip threshold.

5.3.1 Parameter performance evaluation

5.3.1.1 Sensor output comparison with reduced sampling window

A selection of sampling rates and sampling window durations is used to compare the performance (and thus utility) of the 12 sensor output streams of the two 6-DOF IMUs. To do this, we use the Receiver Operating Characteristic (ROC) curves produced using the results of the classifying task on the validation data as per figure 5.12. The Area Under the Curve (AUC) of the ROC curve is also calculated and presented in the legend. The ROC curve plots the rate of true positive prediction vs. the rate of false positive prediction. A rapid rise, and thus a high AUC, represents the ability to achieve a high rate of true positive predictions while maintaining a low rate of false positive predictions. As detailed in table 5.1 an AUC of 1.00 represents perfect performance, and greater than 0.90 is generally considered outstanding (Hosmer Jr, Lemeshow, & Sturdivant, 2013). This gives a good approximate measure of performance for each sensor output, showing outstanding performance across the board for a sampling window duration of 1.00 s and sampling rate of 100 Hz.

Area Under the Curve (AUC)	Evaluation
$AUC = 1.00$	Perfect
$0.90 < AUC < 1.00$	Outstanding
$0.80 < AUC < 0.90$	Excellent
$0.70 < AUC < 0.80$	Acceptable
$0.50 < AUC < 0.70$	Poor

Table 5.1: Summary of AUC performance evaluation criteria.

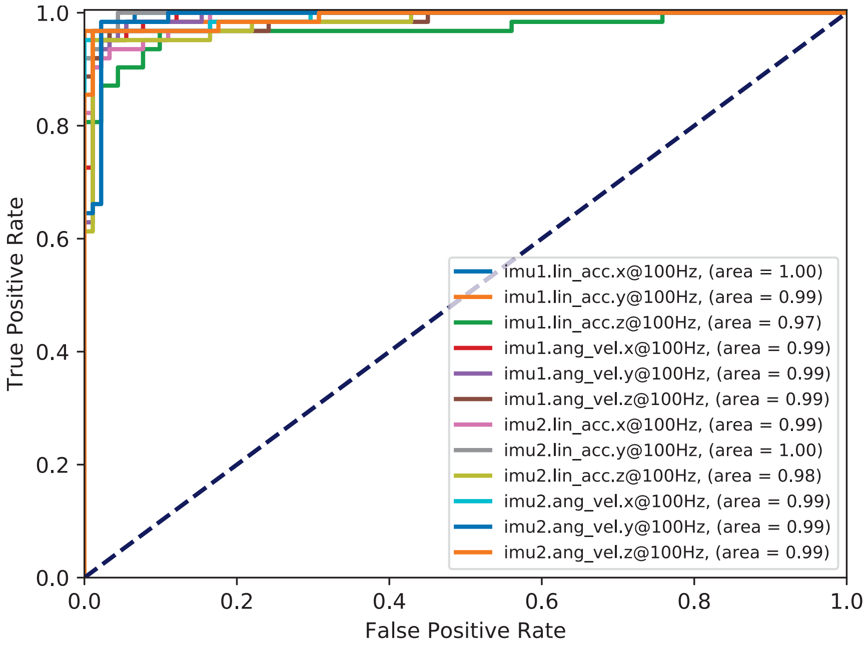

Figure 5.12: Example ROC curves for a single training and testing cycle of the SVM system at 100 Hz subsampling rate with 1.00 s sample window duration.

However, given the randomized separation of the training and validation data from the induced slip dataset, the ROC curves have some noise between iterations of the full SVM training cycle.

To resolve this noise and to help gain a more accurate idea of the performance, we plot the ROC curve averages and standard deviations of multiple cycles as per figures 5.13 and 5.14. In these new figures, we can clearly see that, contrary to expectations based on its use in the literature, the z-axis linear acceleration output on IMU1 shows the lowest performance out of all outputs by a small margin. Reducing the sampling window duration to 0.25 s, as per figures 5.15 and 5.16, significantly worsens the performance of the IMU1 z-axis linear acceleration output while having a comparatively small impact on the performance of the system with all the other output streams.

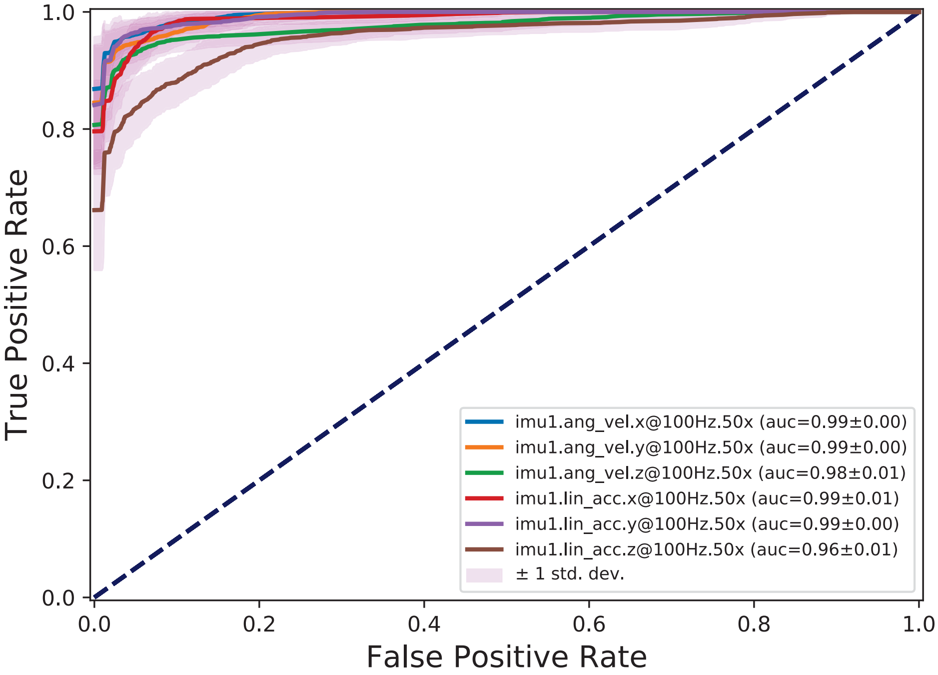

Figure 5.13: ROC curves for 50x training and testing cycle of the SVM system, based on IMU1 outputs sampled at 100 Hz with 1.00 s sample window duration.

Further reducing the sampling window duration exposes a slight performance difference between the two IMUs, as per figures 5.17 and 5.18, with a slightly lower performance for IMU1, specifically for linear acceleration measured along the two other axes. Clearly from all these results, at a given sufficient sampling rate, the sampling window can be quite small and the system can still retain outstanding performance if an appropriate sensor output is selected.

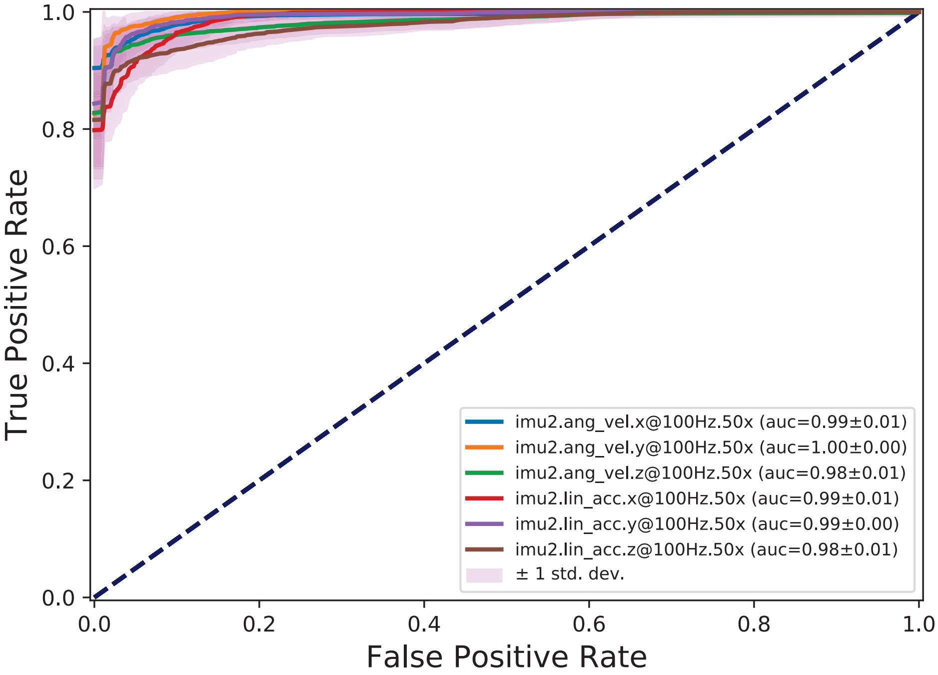

Figure 5.14: ROC curves for 50x training and testing cycle of the SVM system, based on IMU2 outputs sampled at 100 Hz with 1.00 s sample window duration.

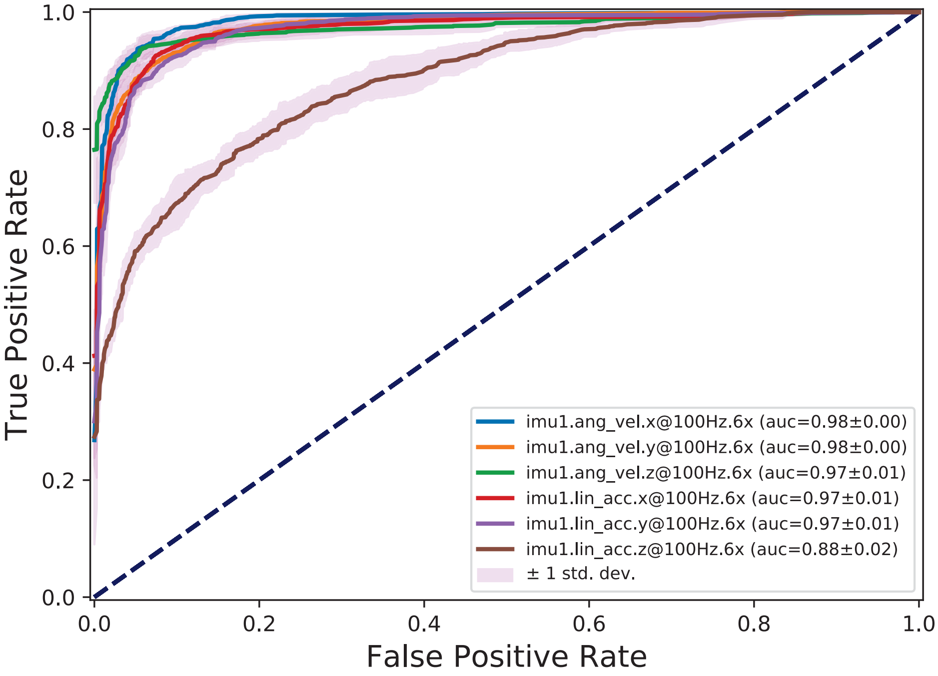

Figure 5.15: ROC curves for 6x training and testing cycle of the SVM system, based on IMU1 outputs sampled at 100 Hz with 0.25 s sample window duration.

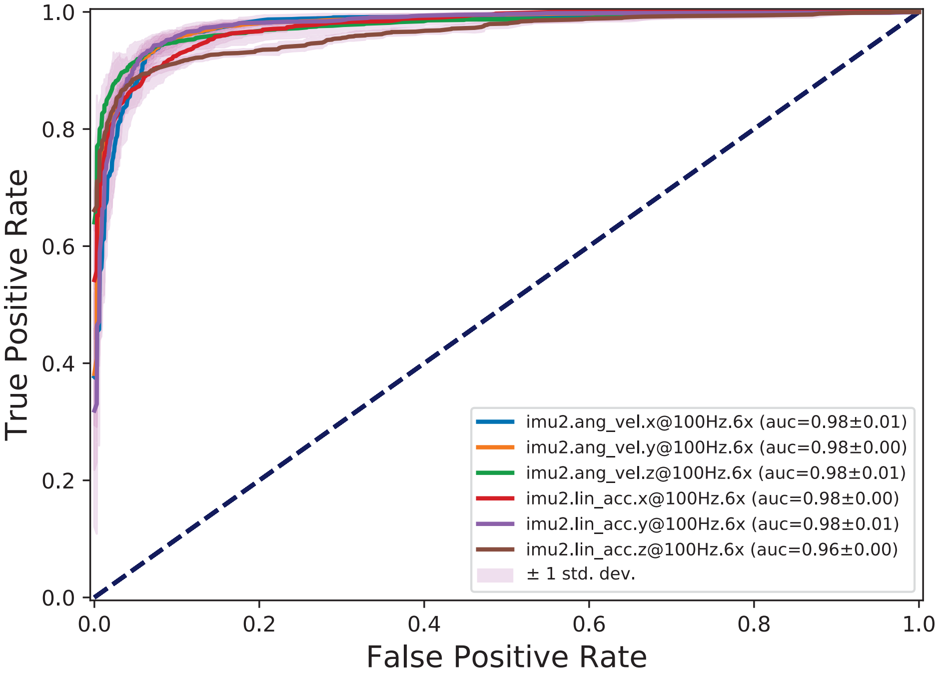

Figure 5.16: ROC curves for 6x training and testing cycle of the SVM system, based on IMU2 outputs sampled at 100 Hz with 0.25 s sample window duration.

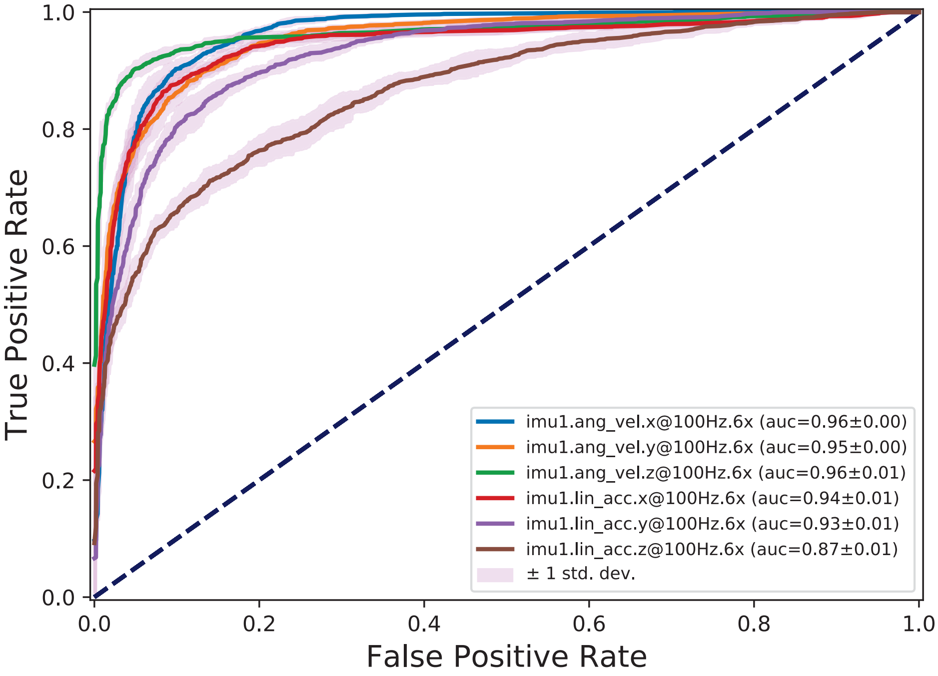

Figure 5.17: ROC curves for 6x training and testing cycle of the SVM system, based on IMU1 outputs sampled at 100 Hz with 0.16 s sample window duration.

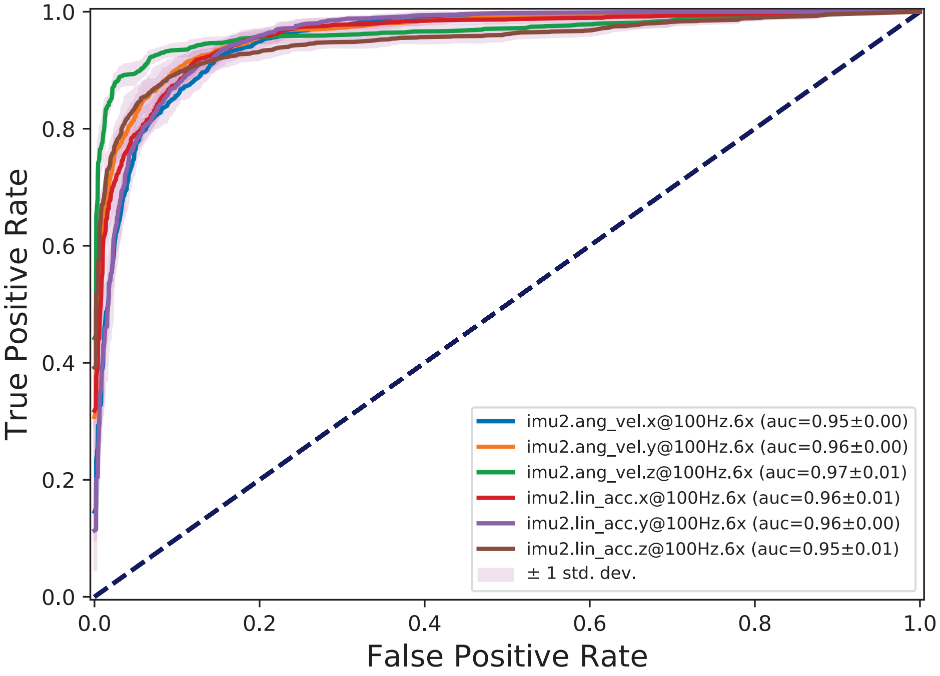

Figure 5.18: ROC curves for 6x training and testing cycle of the SVM system, based on IMU2 outputs sampled at 100 Hz with 0.16 s sample window duration.

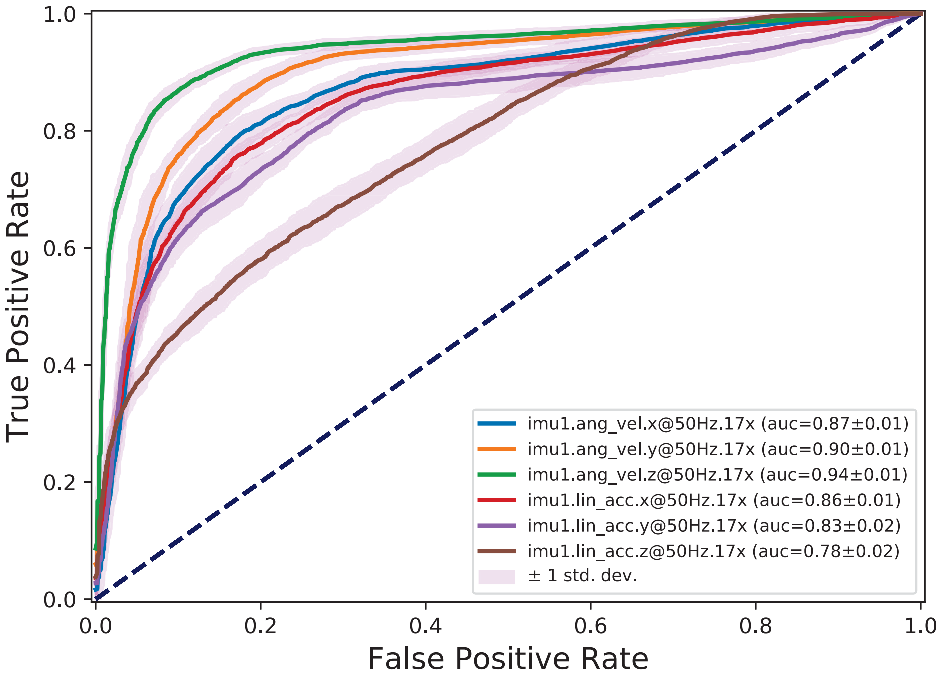

Figure 5.19: ROC curves for 17x training and testing cycle of the SVM system, based on IMU1 outputs sampled at 50 Hz with 0.16 s sample window duration.

5.3.1.2 Sensor output comparison with reduced sampling rate

From the figures in section 5.3.1.1, we can see that at 100 Hz, system performance stays outstanding down to short sampling windows of 0.16 s for all sensor channels. Reducing the sampling rate (while keeping the sample window duration short) produces similar results, though with a sharper drop in performance. Figures 5.19 and 5.20 give a much more discerning picture of the comparative performance of the various sensor outputs. Interestingly, at this reduced sampling rate of 50 Hz, there is less difference in performance between the two IMUs than with the previous sampling rate of 100 Hz.

In terms of individual parameter performance, we can now see a much clearer comparative picture. It is clear that under these system conditions, the sensor output producing the best performance is the angular velocity measurement around the z-axis. Following next in performance is the angular velocity measurement around the y-axis. This is true for both IMUs with little difference in performance between the two for these specific outputs.

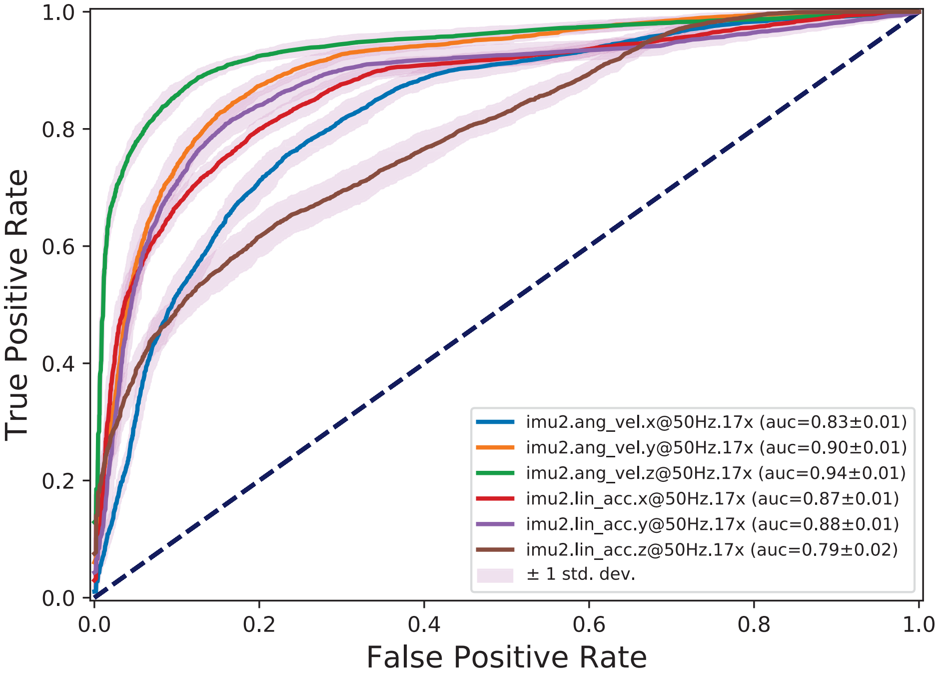

Figure 5.20: ROC curves for 17x training and testing cycle of the SVM system, based on IMU2 outputs sampled at 50 Hz with 0.16 s sample window duration.

w_s (s)	F_s (Hz)	n	ROC AUC
0.16	25	2	0.69 ± 0.02
0.16	40	3	0.78 ± 0.02
0.16	50	4	0.94 ± 0.01
0.16	100	8	0.97 ± 0.01
0.16	200	16	0.98 ± 0.00
0.16	400	32	0.98 ± 0.00
2.00	4	4	0.74 ± 0.04
2.00	8	8	0.85 ± 0.04
2.00	10	10	0.90 ± 0.03
2.00	20	20	0.97 ± 0.02
2.00	40	40	0.98 ± 0.01
2.00	100	100	0.98 ± 0.01

Table 5.2: Summary of subsampling parameters, feature vector length and ROC AUC performance metric.

5.3.1.3 Sampling window and rate comparison for a single output stream

Given the outstanding performance shown by the measurement of angular velocity around the z-axis from IMU2, we focus on it for this section. In figure 5.21 we can again see average ROC curves indicating the performance of the SVM slip classification system under various input conditions. However, in this case there is a single sensor output and the sampling frequency is varied between 25 Hz to 400 Hz. From this plot, it is clear sampling frequencies above 100 Hz give no additional meaningful benefits in performance. It is also clear that the performance rapidly degrades with a sampling rate lower than 50 Hz.

The following figure 5.22, presents a similar picture, with sampling frequencies between 4 to 100 Hz and a sampling window of 2.0 s. For this longer sampling window, very little performance benefits are gained with sampling frequencies higher than 20 Hz. We can also note much larger standard deviation characterising the variations in the ROC curves between SVM training cycles. This is likely caused by the reduction in training samples caused by the longer sampling window.

Here it is interesting to recall equation 6 presented in section 4.4.2 to calculate the feature length of the input provided to the SVM based on the sampling conditions. Given the sampling parameters of figures 5.21 and 5.22, we can calculate the number of features passed to the SVM classification system and the associated performance for the system. Table 5.2 shows this calculation for a handful

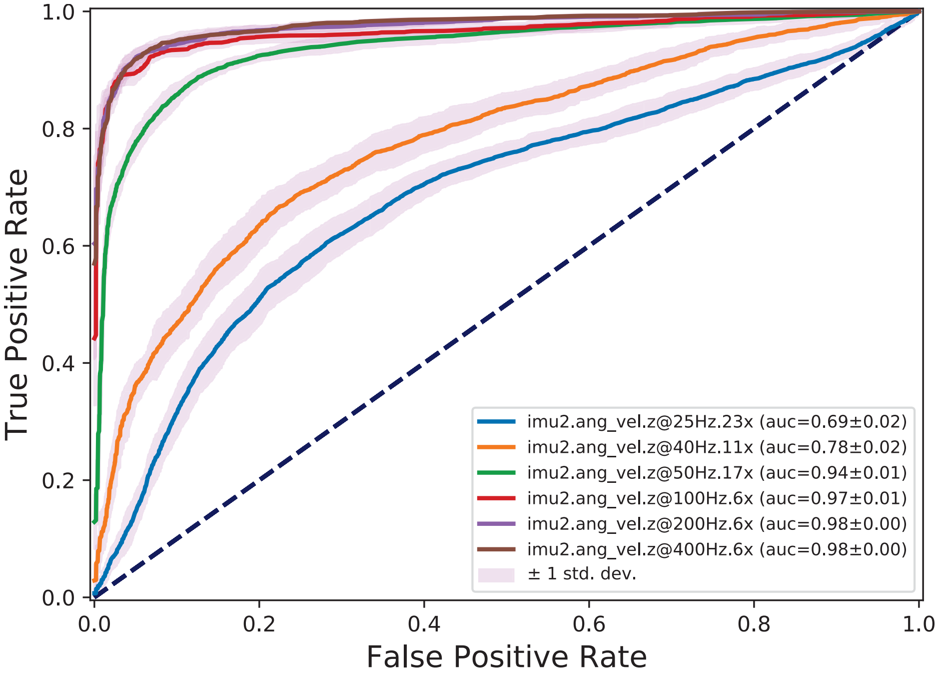

Figure 5.21: Average ROC curves for the SVM system at various subsampling rates, based on IMU2 z-axis angular velocity output sampled at 25 to 400 Hz with 0.16 s sample window duration with various amounts of training and testing cycle.

of cases along with their associated ROC AUC score. It is thus interesting to note that with low sampling rates and long sampling windows, significantly more features (x2.5+) are required to achieve a similar performance to a high sampling rate strategy and short sampling window. Given that SVM algorithms have a time complexity on the order of $O(n^2)$ to $O(n^3)$ (Abdiansah & Wardoyo, 2015), keeping the number of features low has significant implications in computational efficiency of the system.

As previously mentioned, with low sampling rate and long sampling windows, the lower amount of training and testing cases may be impacting the overall classification performance of the system. A possible solution to alleviate this issue would be some form of data augmentation algorithm. It would be especially pertinent to consider the large amount of measured data which gets discarded by the subsampling process. Indeed, for a 20 Hz sampling rate, 95% of the dataset collected at 400 Hz gets discarded prior to training. Separating the dataset in overlapping subsampled sets would most probably improve the training process.

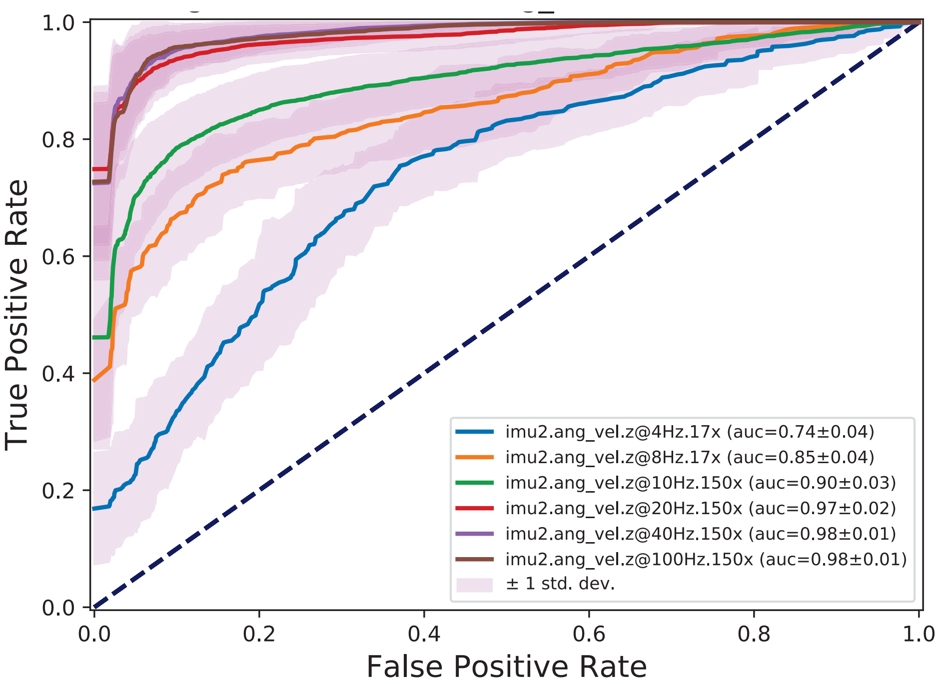

Figure 5.22: ROC curves for various amounts of training and testing cycle of the SVM system, based on IMU2 z-axis angular velocity output sampled at 4 Hz to 100 Hz with 2.0 s sample window duration.

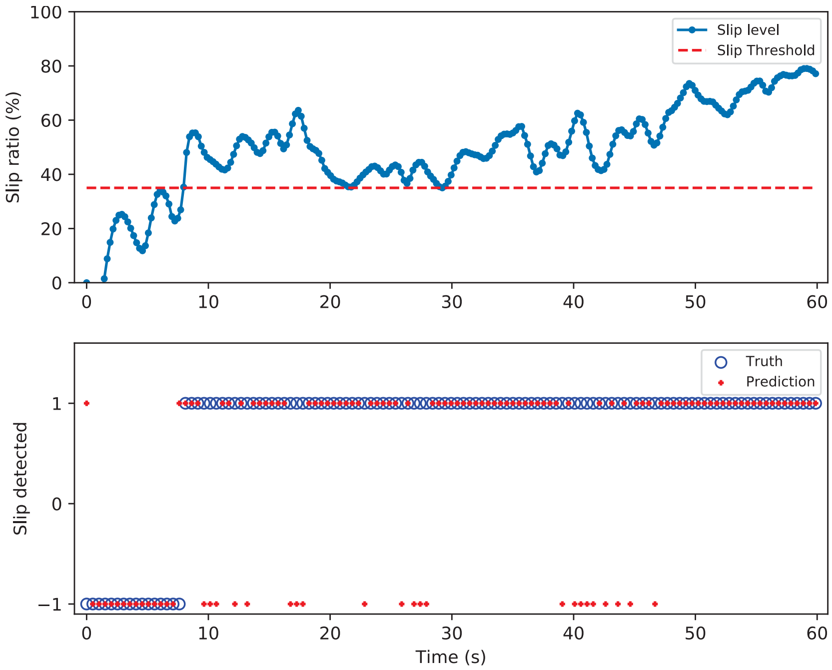

Figure 5.23: Plot of the test results of the classification task on the highslope_g slope dataset, based on IMU2 z-axis angular velocity output sampled at 20 Hz with 0.5 s sample window duration.

5.3.2 Slope test slip classification

Finally, with the parameters found to be effective in the validation process, the trained SVM system is applied to the slip classification task with the slope test data. Figure 5.23 shows a good example of the system detecting the high slip event with a reasonable amount of false negatives. The key moment is the transition between low slip to high slip and there, the system is accurate in detecting the first moments of high slip. Figure 5.23 shows a mostly normal slope ascent, with minimal slip throughout the test, except for a short spike towards the end. It is interesting to note that the classifier flags these peaks as high slip events whereas our ground truth, based on the average slip over the 0.50 s sampling window, does not show a high slip event. When the system is trained and tested with a shorter sampling window and higher sample rate, as per figure 5.25, we can see the short high slip event is properly represented. The slight offset between the prediction and truth may be a sign of misalignment between the slip data derived from the Total Station measurements and the vibration data saved with ROS. The lack of timestamps in the Total Station measurements made accurate alignment between the two datasets difficult.

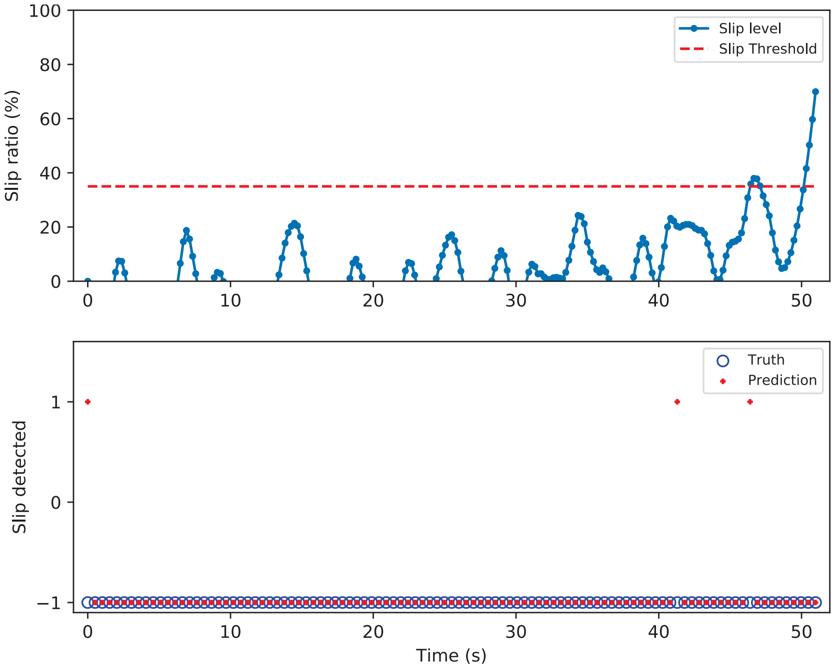

Figure 5.24: Plot of the test results of the classification task on the hill3_a slope dataset, based on IMU2 z-axis angular velocity output sampled at 20 Hz with 0.5 s sample window duration.

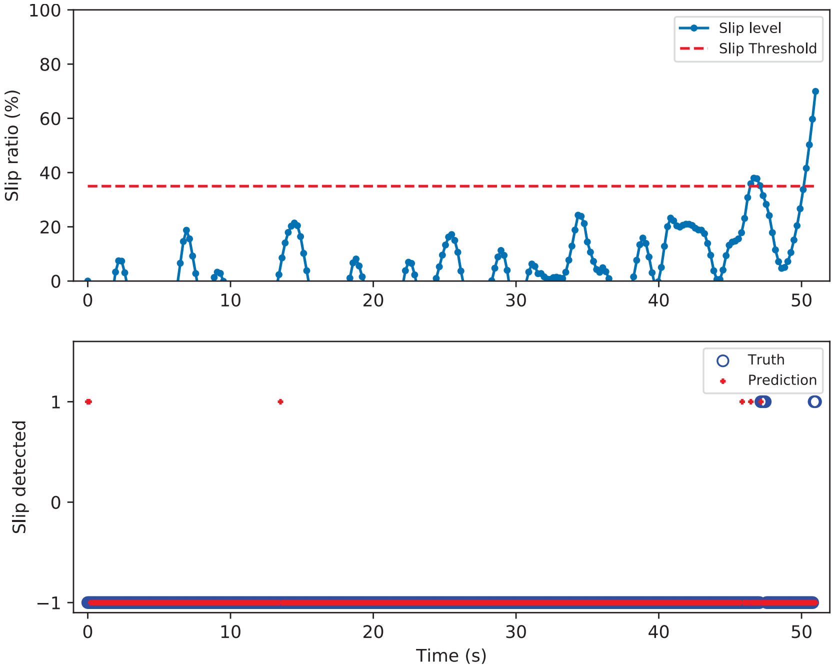

Figure 5.25: Plot of the test results of the classification task on the hill3_a slope dataset, based on IMU2 z-axis angular velocity output sampled at 100 Hz with 0.10 s sample window duration.

5.3.3 ROC AUC plot

Figure 5.26 shows the performance of the SVM binary classifier, given by the ROC AUC metric as per table 5.1, across a wide range of sampling frequencies and sample window durations. This figure informs the trade-offs which can be expected when varying these two parameters. For example, sample window durations below 0.1 s are not recommended. At a sampling frequency of 100 Hz, a 0.1 s sampling window is sufficient, while at 20 Hz a 0.5 s window is recommended. At 8 Hz sample collection, a 5.0 s sample window duration is advised. Given the consistent slip-induced vibration peaks seen around 15 Hz to 18 Hz in the FFT analysis for most sensor outputs, it makes sense to see significant drops in performance for sampling windows of 0.16 s and 0.25 s at around the 40 Hz to 32 Hz point. These would correspond to cases where, for those sampling frequencies, valuable frequency peaks are close to the Nyquist Frequency. Reducing the sampling frequency causes aliasing noise from these frequency peaks and most probably explains the performance reduction. With a fixed sampling rate, reducing the sampling window lowers the resolution of the FFT, which reduces the number of features sent to the classifier. In addition, shorter sampling window means few or no full periods of the waves representing these frequencies would be captured, which means they are less represented in the FFT results. With higher sampling rates, higher frequency components are represented in the FFT output. However, this only increases performance if the sampling window is long enough to capture a few full periods for key frequencies. In other words, the choice of sampling rate Principal Component Analysis (PCA) could be done on the vibration data to gain more accurate insight regarding those key frequencies.

Figure 5.27 shows a similar ROC AUC analysis done with the results of using the classifier on slope test data. Apart from a few small differences, the performance with the test data is generally similar to the performance with the validation data.

Appendix B contains figures B.1 through B.23 which cover all 12 IMU sensor output streams covered in this research. Figures B.2 through B.24 show the classifier performance on the slope test data.

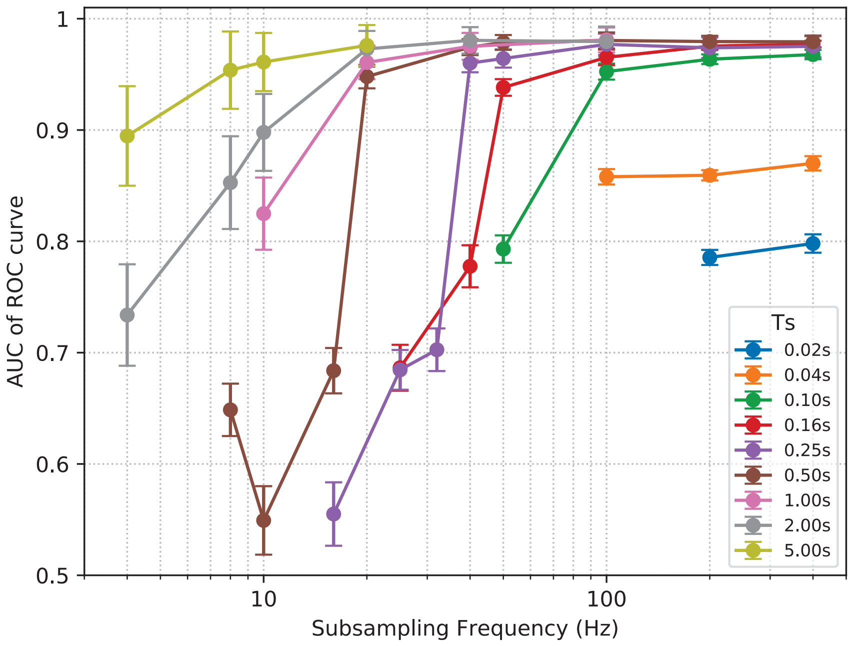

Figure 5.26: Plot of ROC AUC for various cycles of the SVM system, based on validation date with the IMU2 z-axis angular velocity output sampled at 4 Hz to 400 Hz with 0.02 s to 5 s sample window duration.

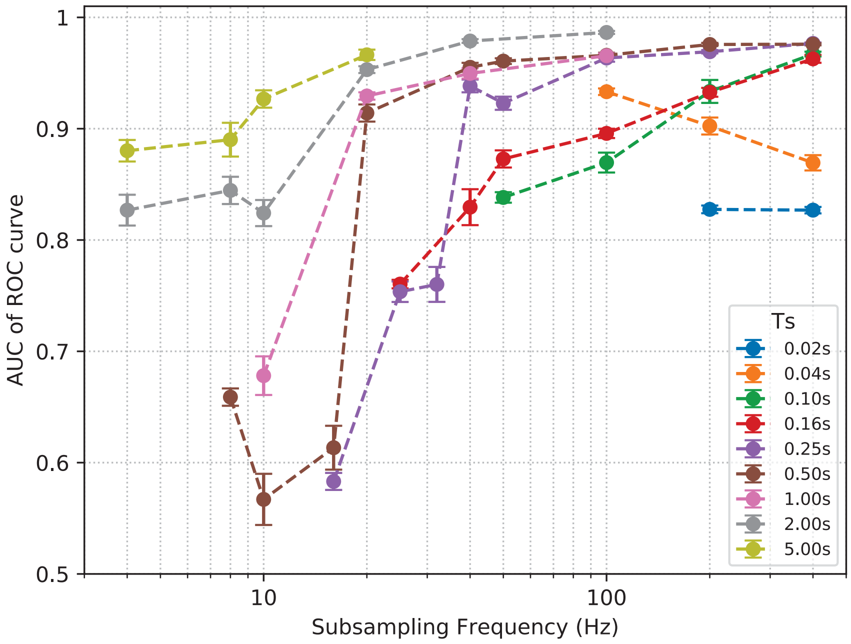

Figure 5.27: Plot of ROC AUC for various cycles of the SVM system, based on slope test date with the IMU2 z-axis angular velocity output sampled at 4 Hz to 400 Hz with 0.02 s to 5 s sample window duration.

5.4 3D printed wheel test results

5.4.1 Single wheel test results

The results of the single wheel tests are not very conclusive. As per figure 5.28 the vibration magnitude for the Husky's wheel is minimal across slip values and not at all representative of what is seen in the full rover tests. The low vibrations peak at 20% slip and are lower at higher slip values. The vibrations measured in the 3D printed wheels show different dynamics as well, with low vibrations at 20% and 40% slip and high vibrations only at 60% slip.

Interestingly, as per figure 5.29, with a non-zero slip angle, the SLR wheel showed significantly different vibration magnitude depending on the orientation of the slip angle. This shows that the slip angle between wheel grousers and the ground may have a significant impact on the vibrations induced in the wheel by the wheel-soil interaction.

Given the structure on which the wheel is mounted for the single-wheel tests vs the full rover test, it should be noted that there is a significant difference in rigidity between the two systems. On the Husky rover, the wheels are very rigidly constrained in all directions. On the other hand, our 4-bar mechanism for single-wheel testing is less rigidly constraining. For most other experiments, this poses no problems and gives perfectly good data. However, for an experiment where vibrations constitute the main interest, it may not be an appropriate system.

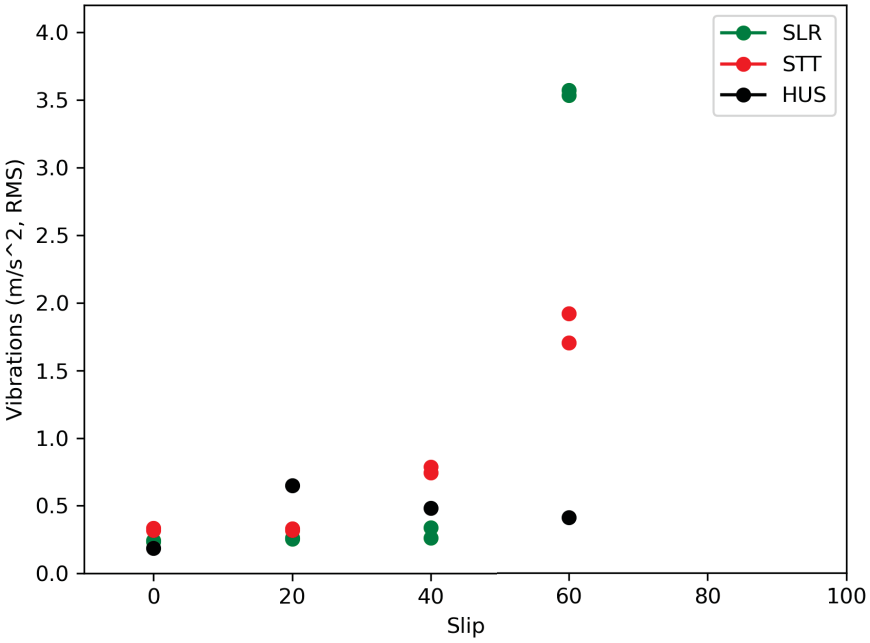

Figure 5.28: Magnitude of vibrations measured during the 3D printed wheel tests according to slip % with a 0 degree slip angle.

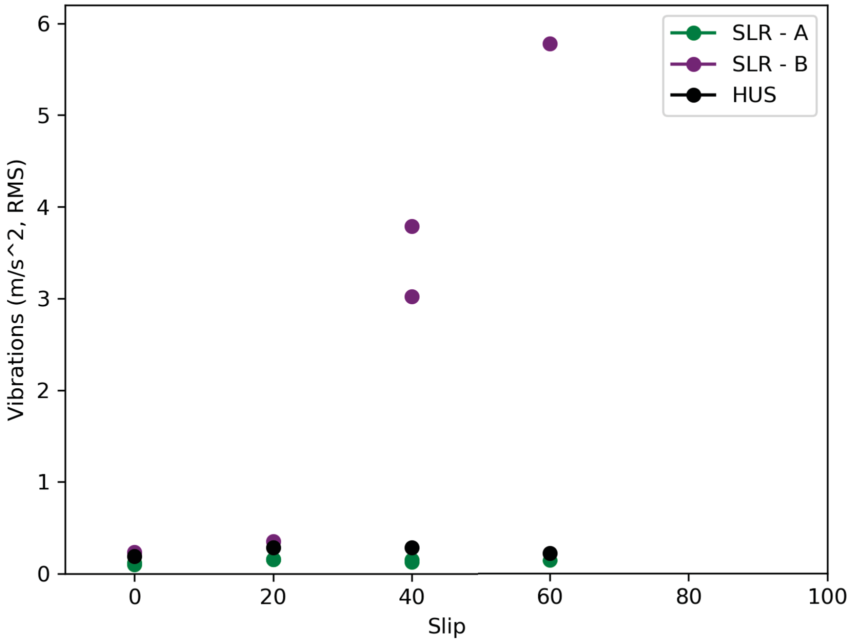

Figure 5.29: Magnitude of vibrations measured during the 3D printed wheel tests according to slip % with a 15 degree slip angle.

Chapter 6

Conclusion

This research presents a novel wheel-terrain slip classification system for skid-steer exploration rovers. Work done on data collected in the field suggests that this system would be useful in giving early warnings of elevated slip events in exploration rovers. Early warnings are a valuable feature since elevated slip events can devolve into entrapment situations where valuable exploration hardware can be temporarily stuck, wasting precious mission time getting unstuck, or can be lost, forcing early mission termination. The system measures the vibrations induced in the chassis of the rover during movements using an IMU. The measurements are then converted to frequency domain features and classified using an SVM system to differentiate low and high slip level with high success rate. The SVM is trained using data collected from rover test sessions where slip was induced to specific values through a mechanical constraint on the rover. The classification system is then tested with variable slip data from slope ascent tests. The classification system can be implemented with modest hardware requirements and requires a single channel of 6-DOF IMU sensor stream which is usually already present in most modern rover designs. An analysis is presented of the performance differences observed between the six sensor output channels and between IMUs installed in two locations on the rover. Trade-offs in performance according to sampling rate and sampling window duration are also discussed with emphasis on modest requirements relevant to microrovers.

This research comparatively evaluates the performance of twelve sensor output channels of two 6-DOF IMUs. It is shown that with generous sampling window duration and rate such as 1.00 s and 100 Hz, there is no significant difference between the performance of the system between the different sensor outputs. At reduced sampling window durations and rates, the results show that one

w_s (s)	F_s (Hz)	Features n	ROC AUC
5.0	10	25	0.96 ± 0.03
5.0	8	20	0.96 ± 0.04
1.0	100	50	0.98 ± 0.01
0.5	20	5	0.95 ± 0.01
0.25	100	12	0.98 ± 0.01
0.25	40	5	0.96 ± 0.01
0.16	100	8	0.97 ± 0.01
0.16	50	4	0.94 ± 0.01

Table 6.1: Summary of system parameter combinations resulting in outstanding results with IMU2's z-axis angular velocity output.

of the outputs, the z-axis linear acceleration, performs significantly worse than the others for both IMUs. For this particular output, the difference in performance was also significant between the two IMU locations, with the unit placed closer to the wheels performing better. This supports prior work indicating that IMUs located closer to the wheel result in higher classification performance. As mentioned in chapter 4, it can be noted that the structure on which the top IMU was mounted was part of the payload structure of the Husky rover, which is not as stiff as the rest of the chassis. This may have been a contributing factor to the lower performance observed. The sensor output with the best performance was the angular velocity around the z-axis in most situations.

The system performance is evaluated at different values of sampling window duration and sampling rate. A summary of key parameter combinations leading to outstanding results using IMU2's z-axis angular velocity output is shown in table 6.1. Sampling windows below 0.10 s are found to lead to significantly degraded performance. sampling windows of 0.10 s or greater produce outstanding performance (ROC AUC $>$ 0.90 (Hosmer Jr et al., 2013)) at high sampling rates of 200 Hz to 400 Hz. Increasing the sampling window allows outstanding performance at reduced sampling rates. A 0.25 s sampling window with 40 Hz sampling rate produce outstanding . Similar results are obtained with 0.50 s and 20 Hz. These two pairs of parameters provide outstanding performance with only five frequency domain features passed to the classifier. Significantly increasing the sampling window allows similar performance with reduced sampling rates such as 5.00 s and 10 Hz. However, this does come at a computational cost since it increases the feature count to 25 features. Given a time complexity on the order of $O(n^2)$ to $O(n^3)$ for SVM algorithms (Abdiansah & Wardoyo, 2015), keeping the feature count low is important for the computational efficiency of the system.

To tie this work back into the literature on slip estimation systems presented in chapter 2, we can compare table 6.1 to table 2.2. Results obtained in the present research show that outstanding performances were achieved with IMU sampling rate $<$100 Hz which is modest compared to previous work. With sampling rates as low as 20 Hz, outstanding results are achieved with $<$1.00 s sampling window duration. Similarly outstanding results were also achieved at low rates of 10 Hz with sampling window durations of 5.00 s, which could still result in detection latencies on the same order of magnitude as previous work. With sampling rates of 100 Hz and above, outstanding results are achieved with sampling window durations as low as 0.10 s, which could provide detection latencies significantly shorter than what is demonstrated in previous work.

This research makes two main contributions to the field of remote exploration rovers. First, a novel wheel-terrain slip estimator system based on frequency domain features of IMU measurements classified by an SVM system. Second, an analysis of performance trade-offs of various sampling rates and sampling window durations, suggesting a few options with outstanding performance. Further, a related analysis of system performance depending on the sensor output used suggests that angular velocity around the z-axis is a good option.

For future work, it may be valuable to evaluate the performance of this system with improved ground truth velocity measurement in the form of RTK GNSS or VO. Testing a few data augmentation methods would also be valuable if there is significant interest in low-frequency IMU sampling, on the order of 8 Hz to 10 Hz. Comparing the performance and efficiency of this system with other systems described in the literature would be interesting, especially with unsupervised learning/clustering methods. It would also be interesting to gather slip vibration datasets in various types of soils and terrain. This would allow performance evaluation in soil types different from the trained types or in variable terrain situations. A closer examination of the performance of the system at the transition moment between low slip and high slip could provide a more pertinent method of performance evaluation for these slip classifiers which aim to act as early warning systems. Given that the system in this research is trained and tested on data obtained from a rover commanded to move at constant speed, it may be interesting to investigate some form of scaling rule based on wheel speed and/or rover power consumption. This could allow the system to perform correctly over a range of commanded rover speeds. Given the wheel-terrain dynamics of skid-steer rover mobility, it may be interesting to investigate the vibrations seen during turning motions at different radii. It may be possible to link these vibrations with those found at specific values of slip during forward movements. This could provide a method for in-situ unsupervised or semi-supervised learning without requiring ground-truth measurements. Investigating turning motions may also lead to a method to classify elevated angular slip events. Finally, testing the performance of this system with various rover and wheel designs and sizes would be valuable to verify if any design features such as suspension elements significantly impact system performance. As mentioned in the introduction, given that our research group is a science team partner to the Emirates Lunar Mission, we will have access to recorded telemetry data from the Rashid rover. With the pictures taken by the rover used to estimate the ground truth of the rover's movements, we may be able to test the performance of this classifier on telemetry from an actual Lunar rover mission.

Appendix A

Sensor outputs frequency spectrum plots

A.1 FFT of vibrations during indoor induced slip tests

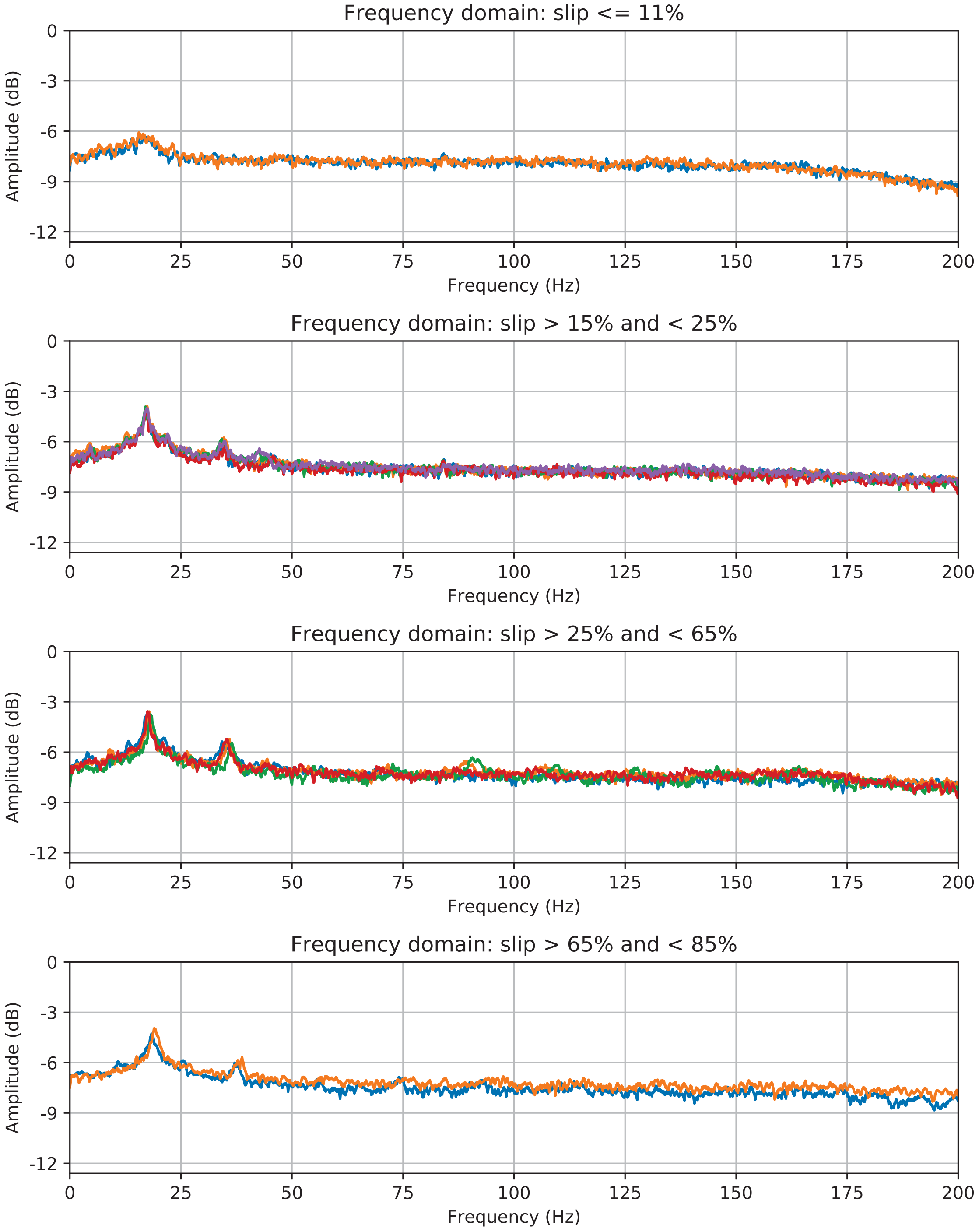

Figure A.1: Frequency spectrum of vibrations in z-axis linear acceleration measured by IMU1 during induced slip tests at 5 cm/s in our indoor facility separated according to slip %.

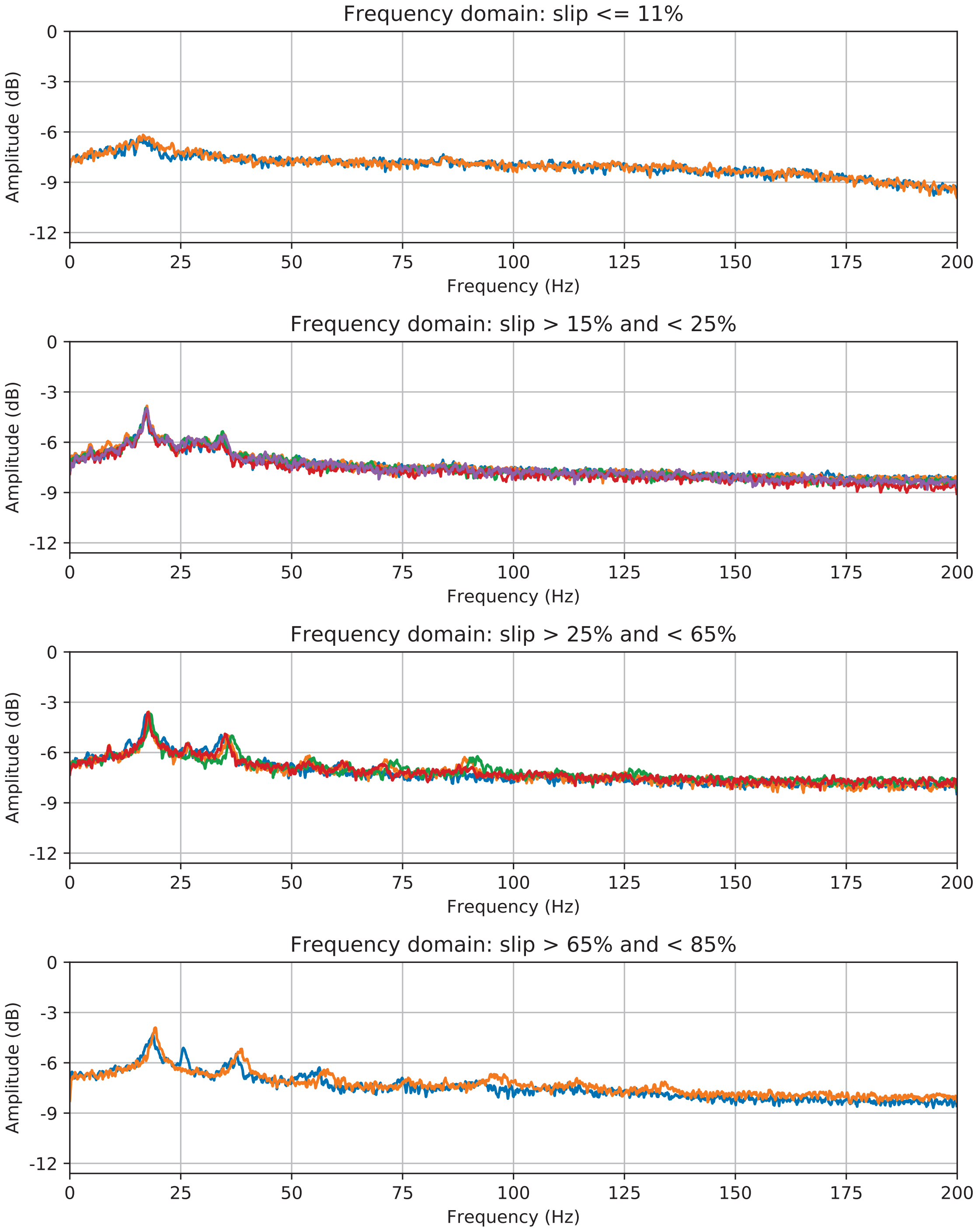

Figure A.2: Frequency spectrum of vibrations in z-axis linear acceleration measured by IMU2 during induced slip tests at 5 cm/s in our indoor facility separated according to slip %.

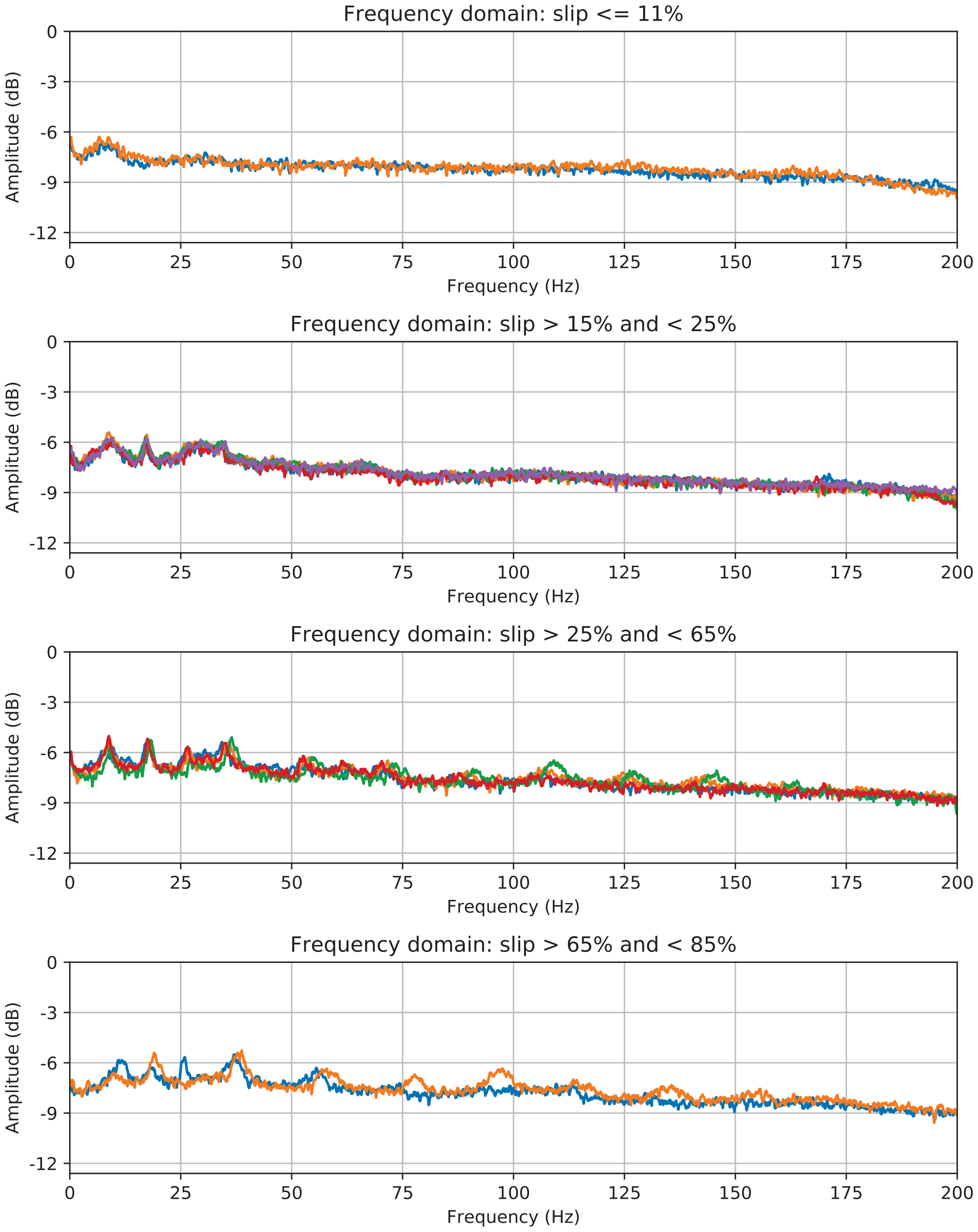

Figure A.3: Frequency spectrum of vibrations in y-axis linear acceleration measured by IMU1 during induced slip tests at 5 cm/s in our indoor facility separated according to slip %.

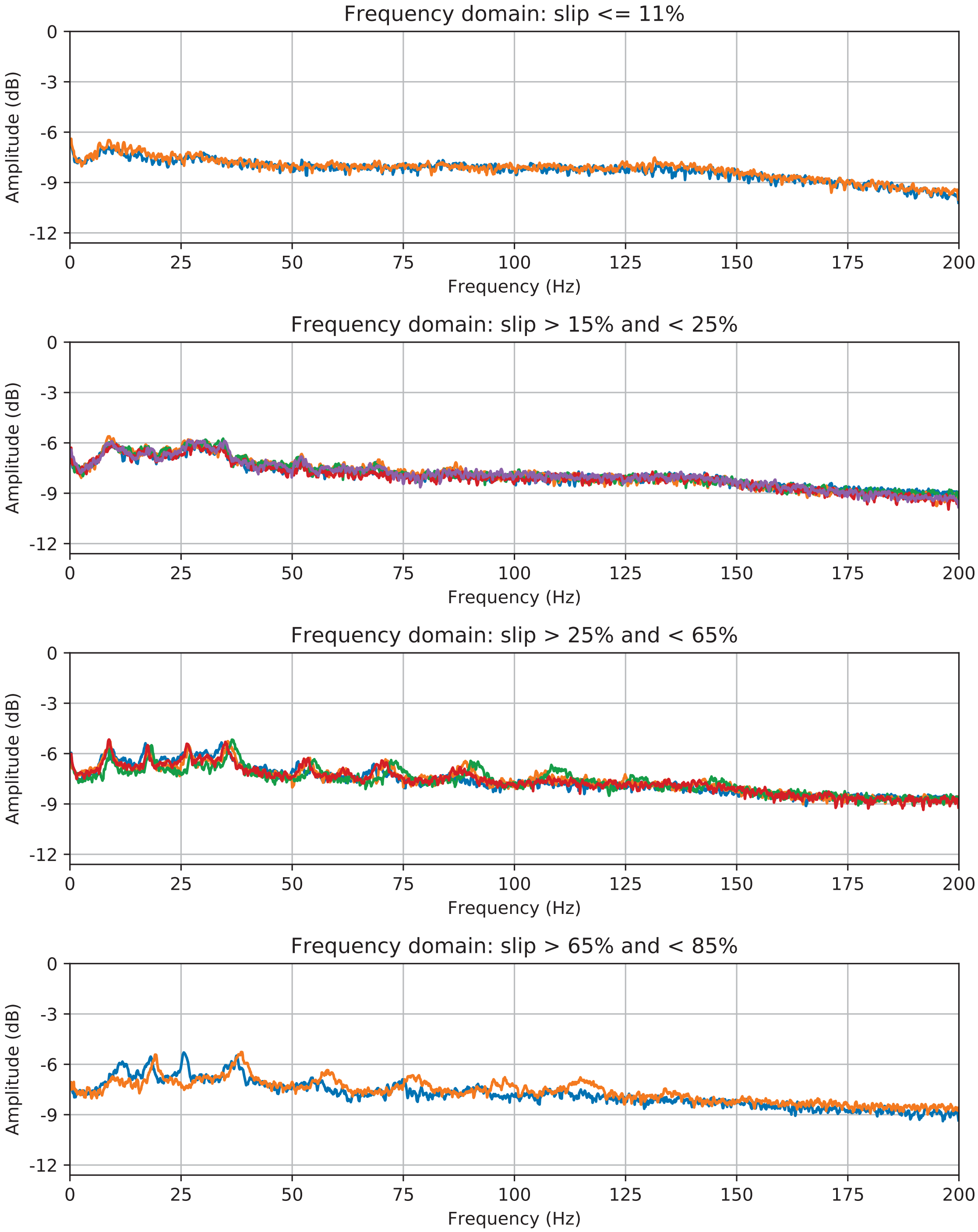

Figure A.4: Frequency spectrum of vibrations in y-axis linear acceleration measured by IMU2 during induced slip tests at 5 cm/s in our indoor facility separated according to slip %.

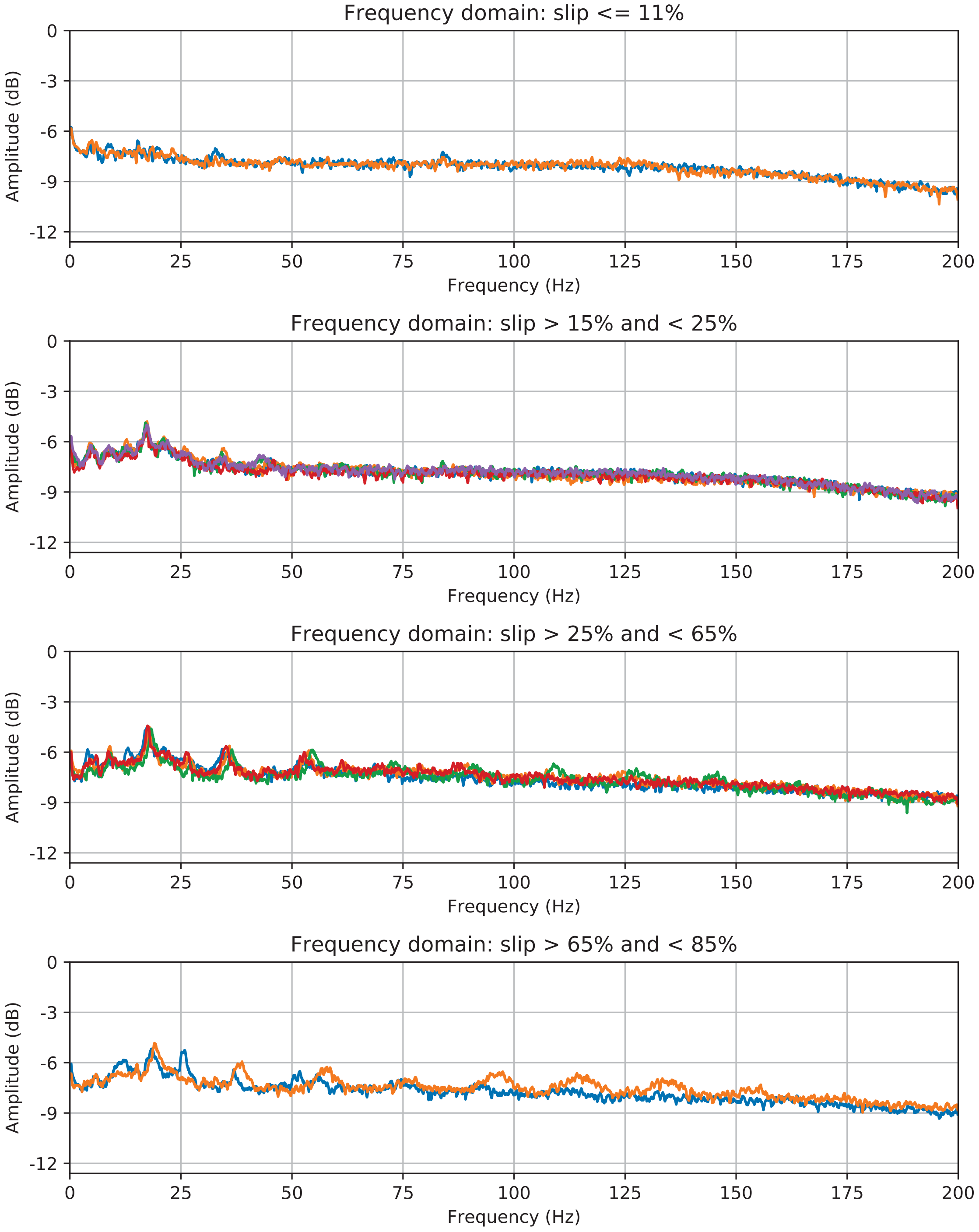

Figure A.5: Frequency spectrum of vibrations in x-axis linear acceleration measured by IMU1 during induced slip tests at 5 cm/s in our indoor facility separated according to slip %.

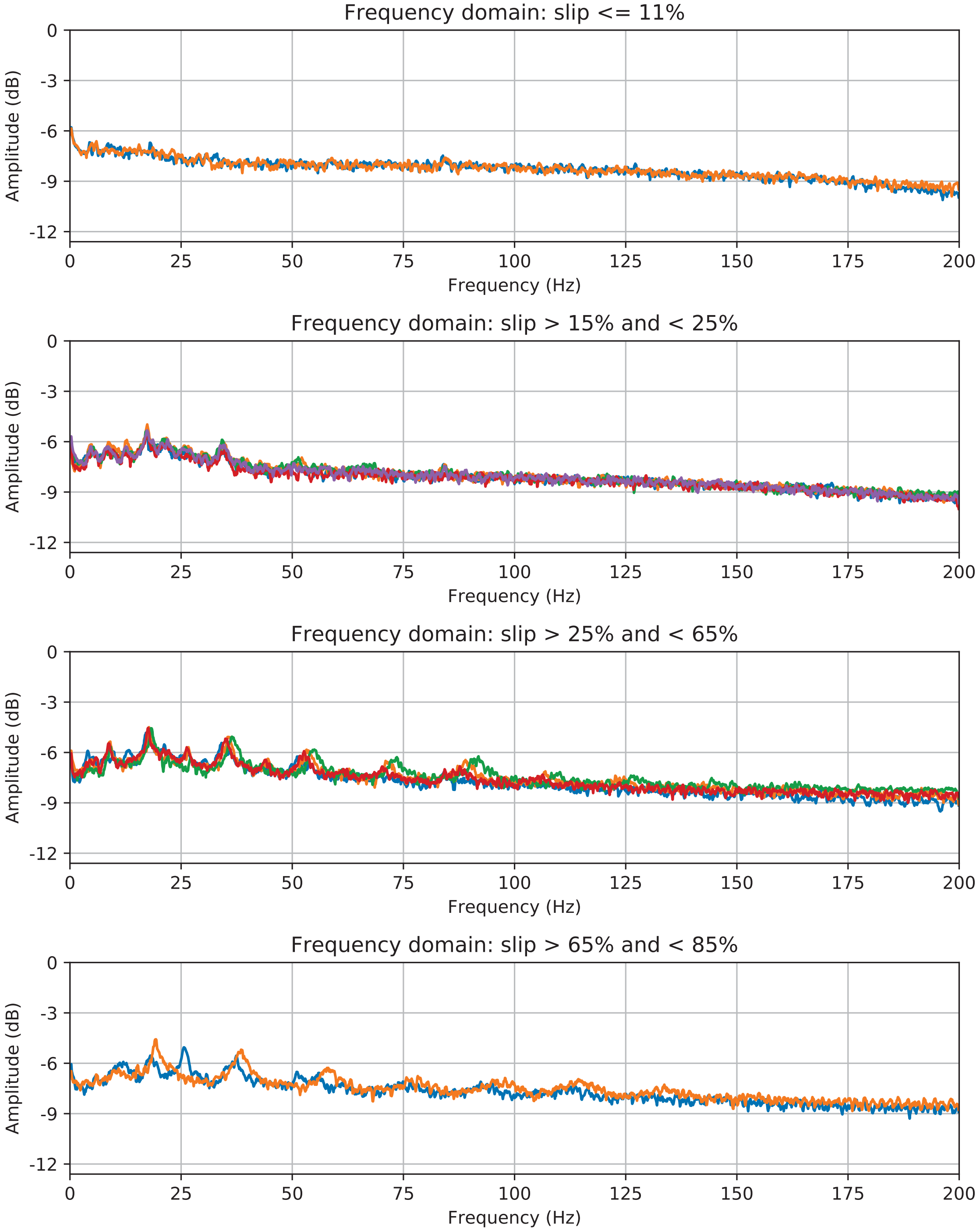

Figure A.6: Frequency spectrum of vibrations in x-axis linear acceleration measured by IMU2 during induced slip tests at 5 cm/s in our indoor facility separated according to slip %.

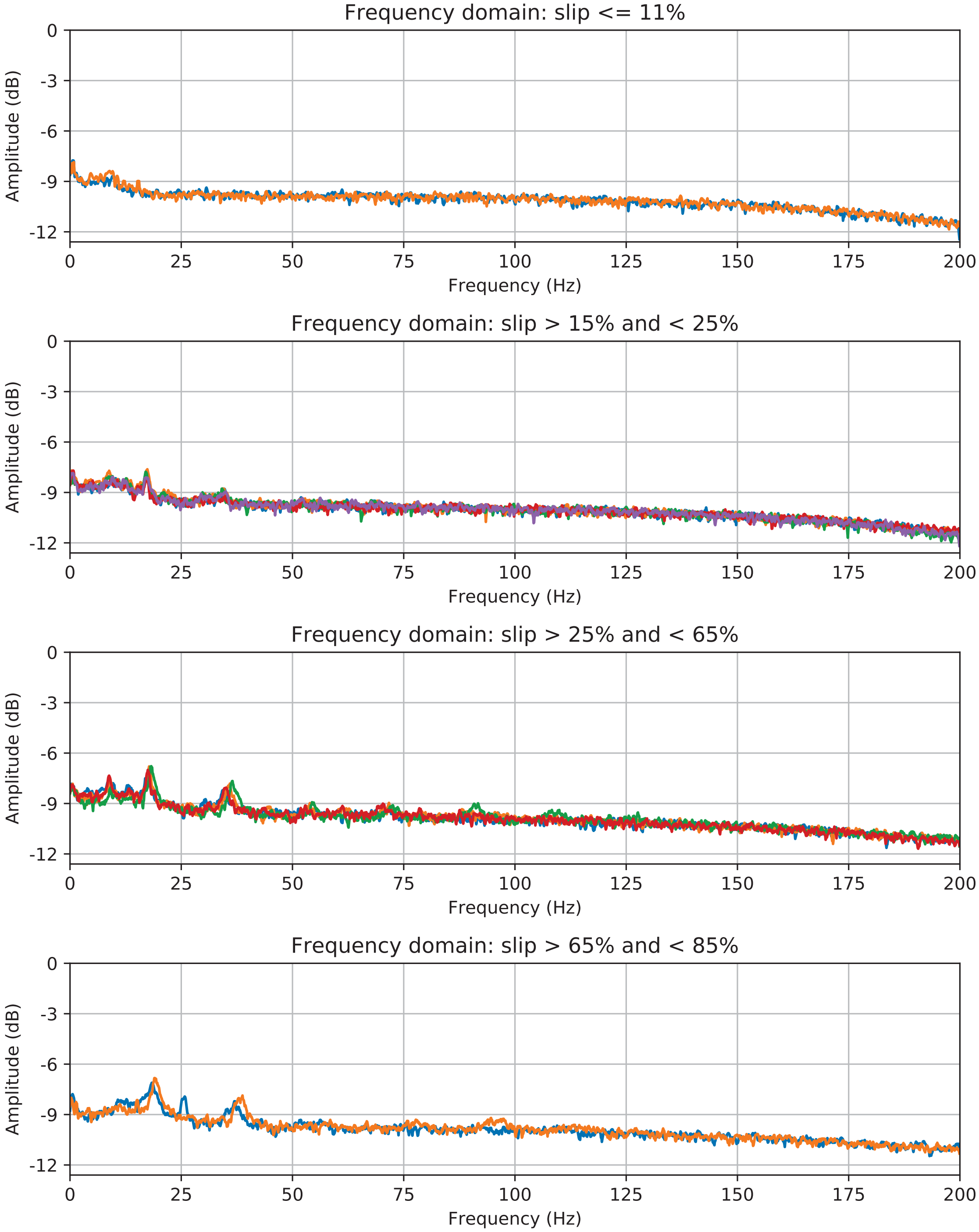

Figure A.7: Frequency spectrum of vibrations in z-axis angular velocity measured by IMU1 during induced slip tests at 5 cm/s in our indoor facility separated according to slip %.

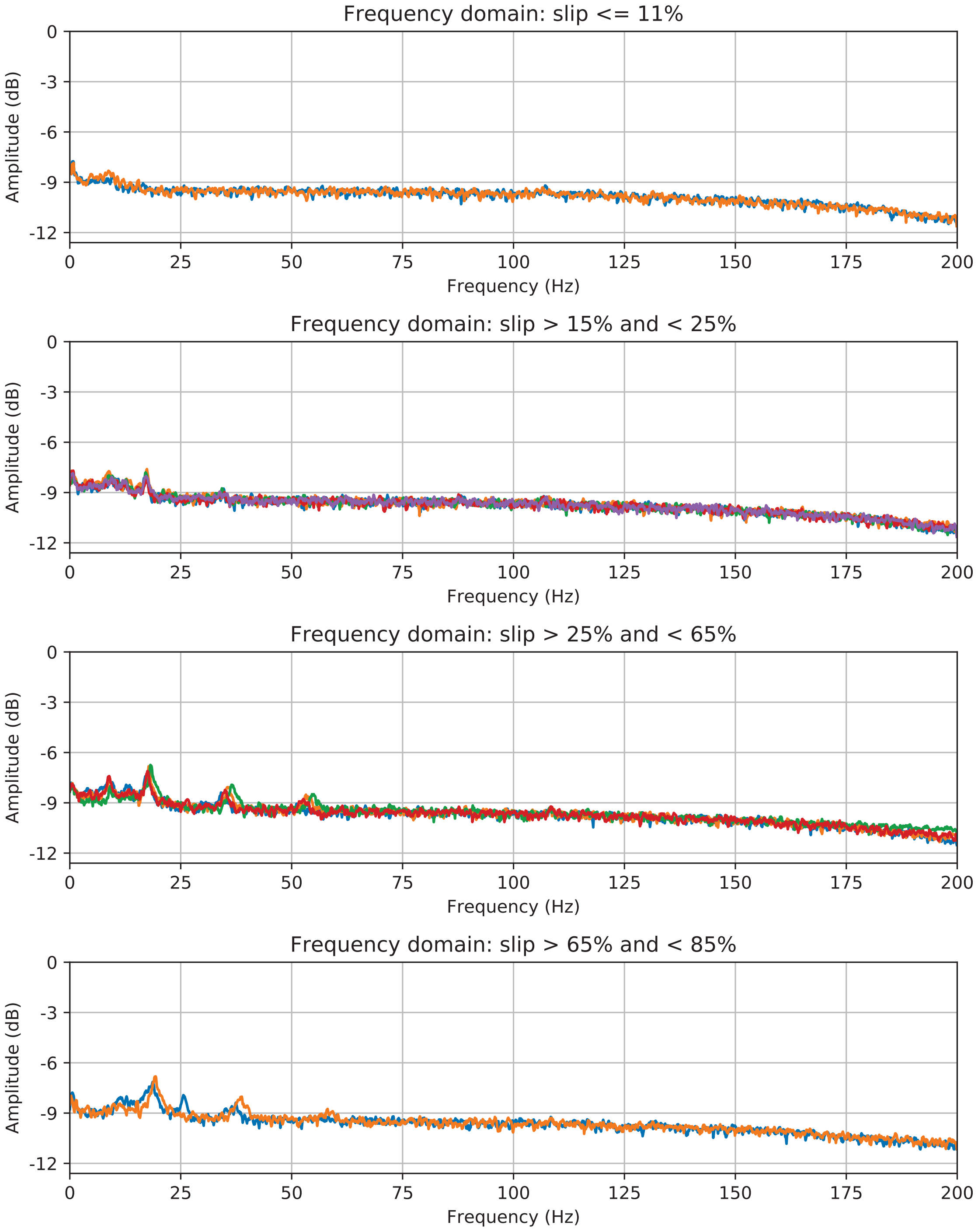

Figure A.8: Frequency spectrum of vibrations in z-axis angular velocity measured by IMU2 during induced slip tests at 5 cm/s in our indoor facility separated according to slip %.

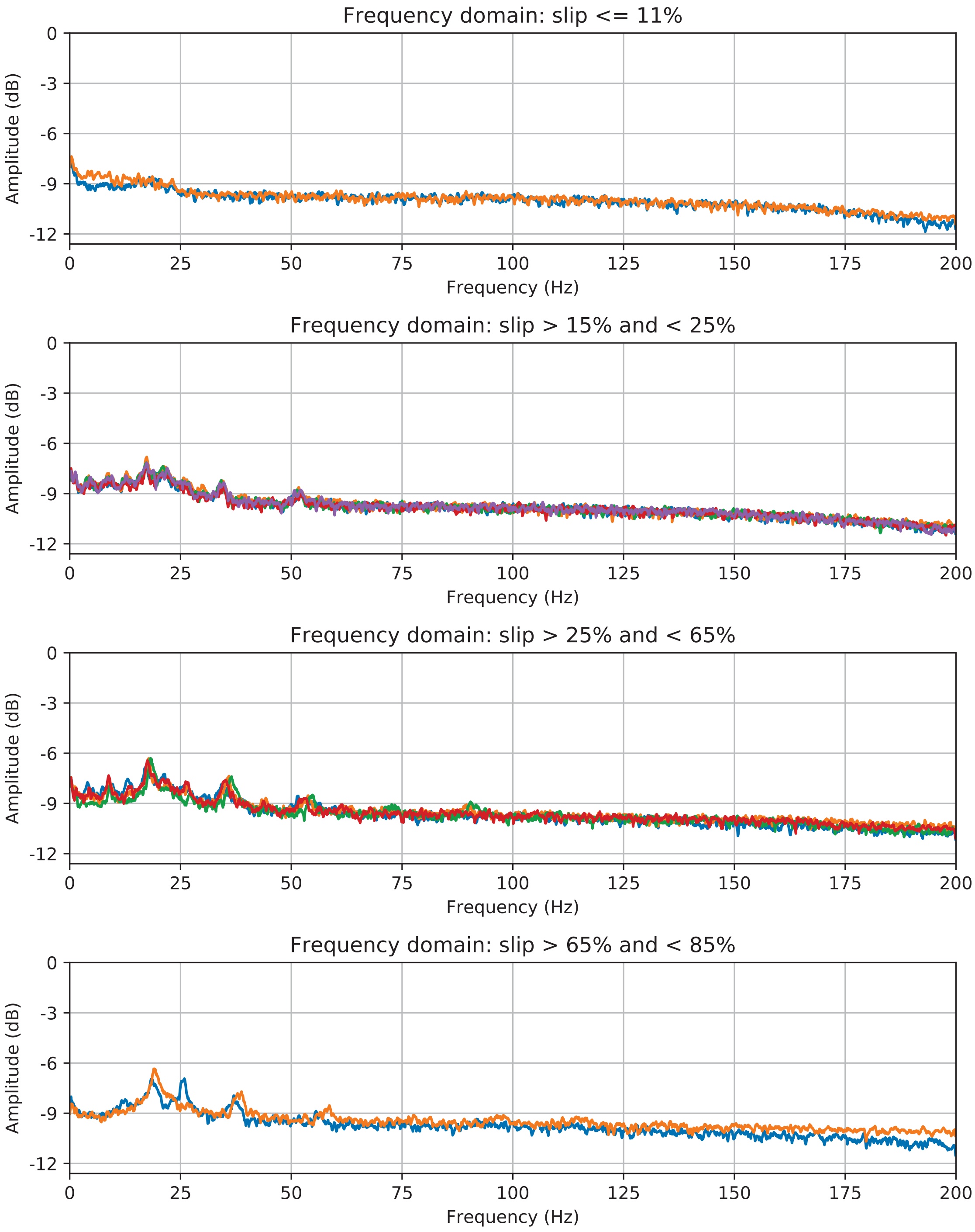

Figure A.9: Frequency spectrum of vibrations in y-axis angular velocity measured by IMU1 during induced slip tests at 5 cm/s in our indoor facility separated according to slip %.

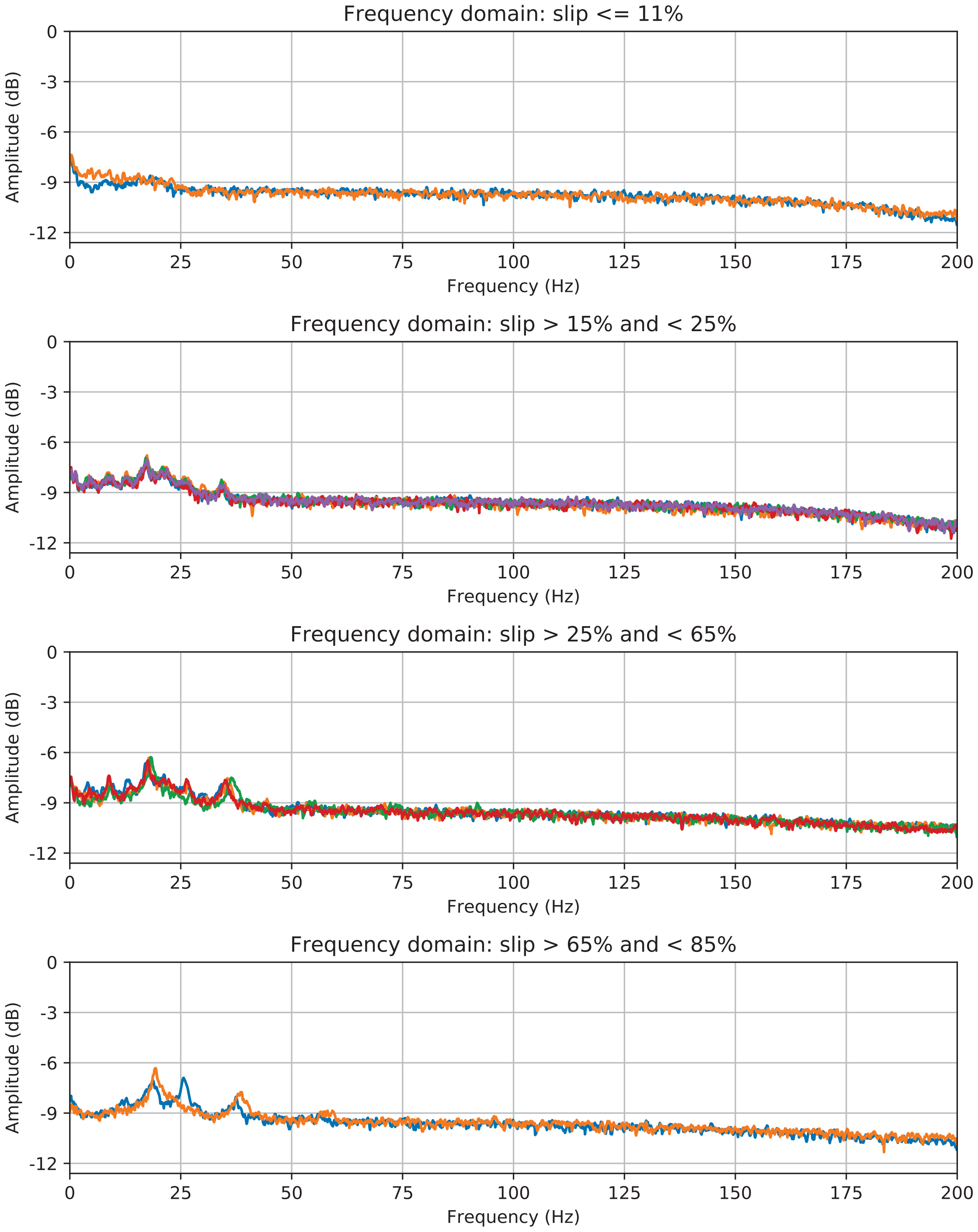

Figure A.10: Frequency spectrum of vibrations in y-axis angular velocity measured by IMU2 during induced slip tests at 5 cm/s in our indoor facility separated according to slip %.

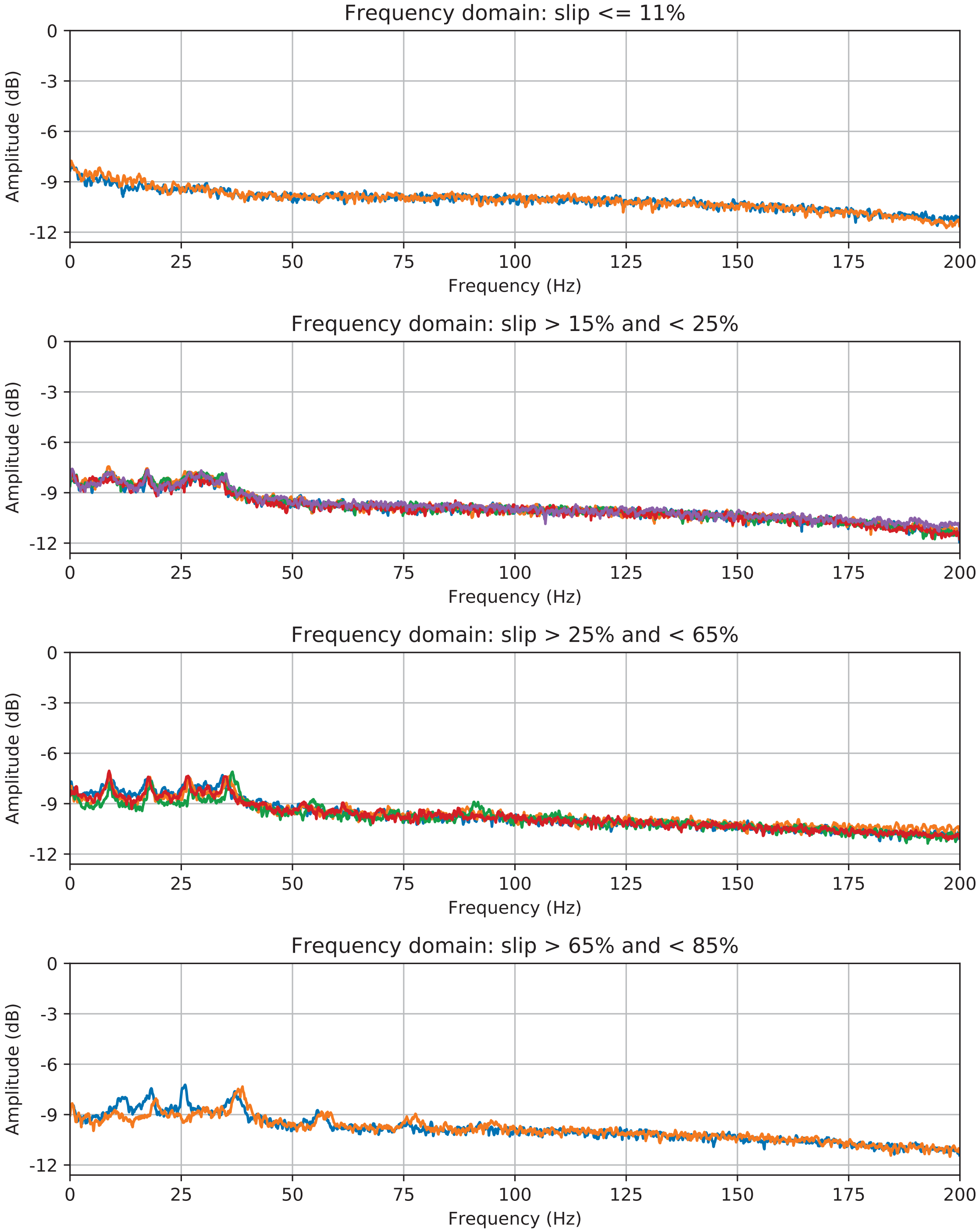

Figure A.11: Frequency spectrum of vibrations in x-axis angular velocity measured by IMU1 during induced slip tests at 5 cm/s in our indoor facility separated according to slip %.

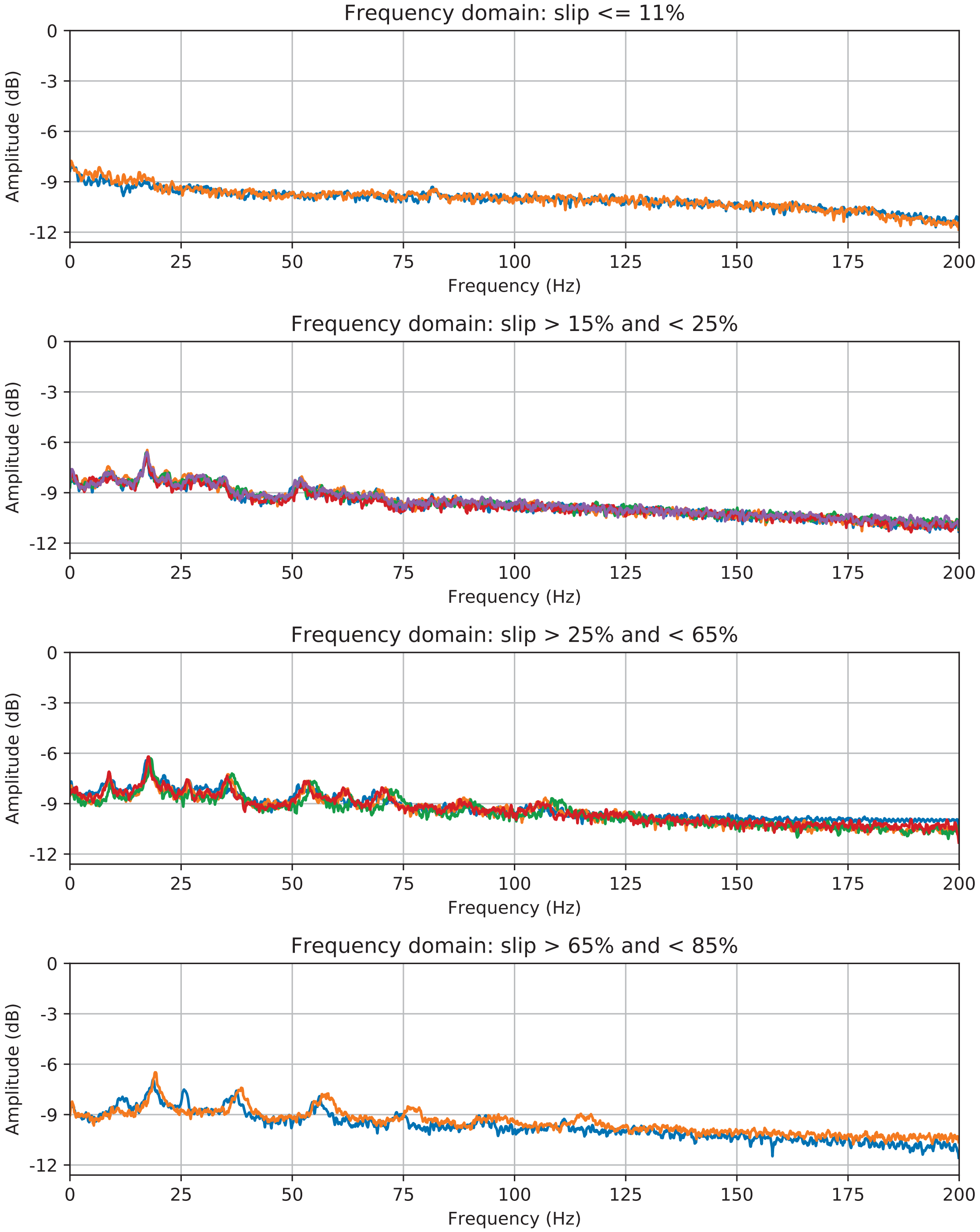

Figure A.12: Frequency spectrum of vibrations in x-axis angular velocity measured by IMU2 during induced slip tests at 5 cm/s in our indoor facility separated according to slip %.

A.2 FFT of vibrations during outdoor induced slip tests

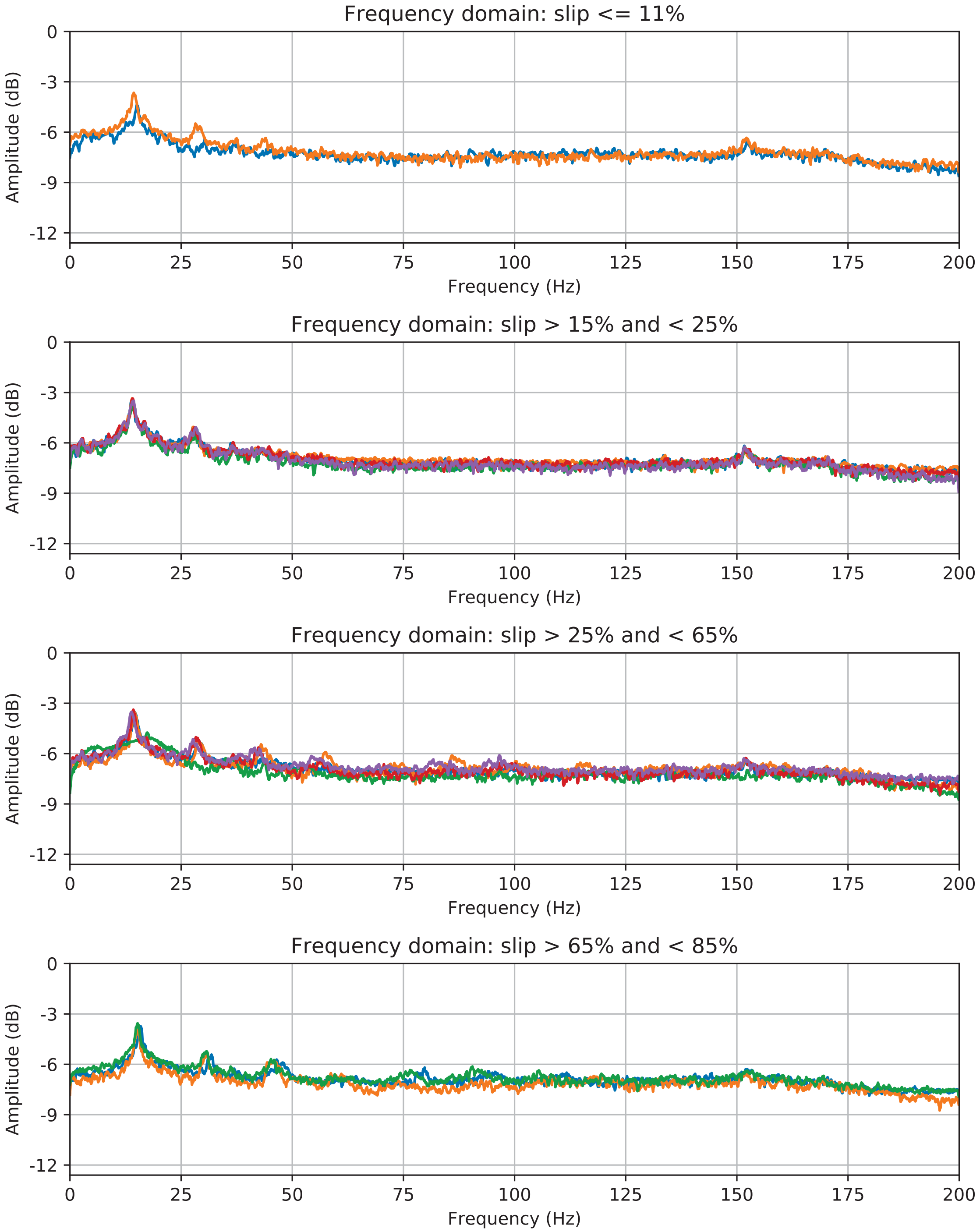

Frequency domain: slip <= 11%

Frequency domain: slip > 15% and < 25%

Frequency domain: slip > 25% and < 65%

Frequency domain: slip > 65% and < 85%

Figure A.13: Frequency spectrum of vibrations in z-axis linear acceleration measured by IMU1 during induced slip tests at 20 cm/s at the CSA's outdoor facility separated according to slip %.

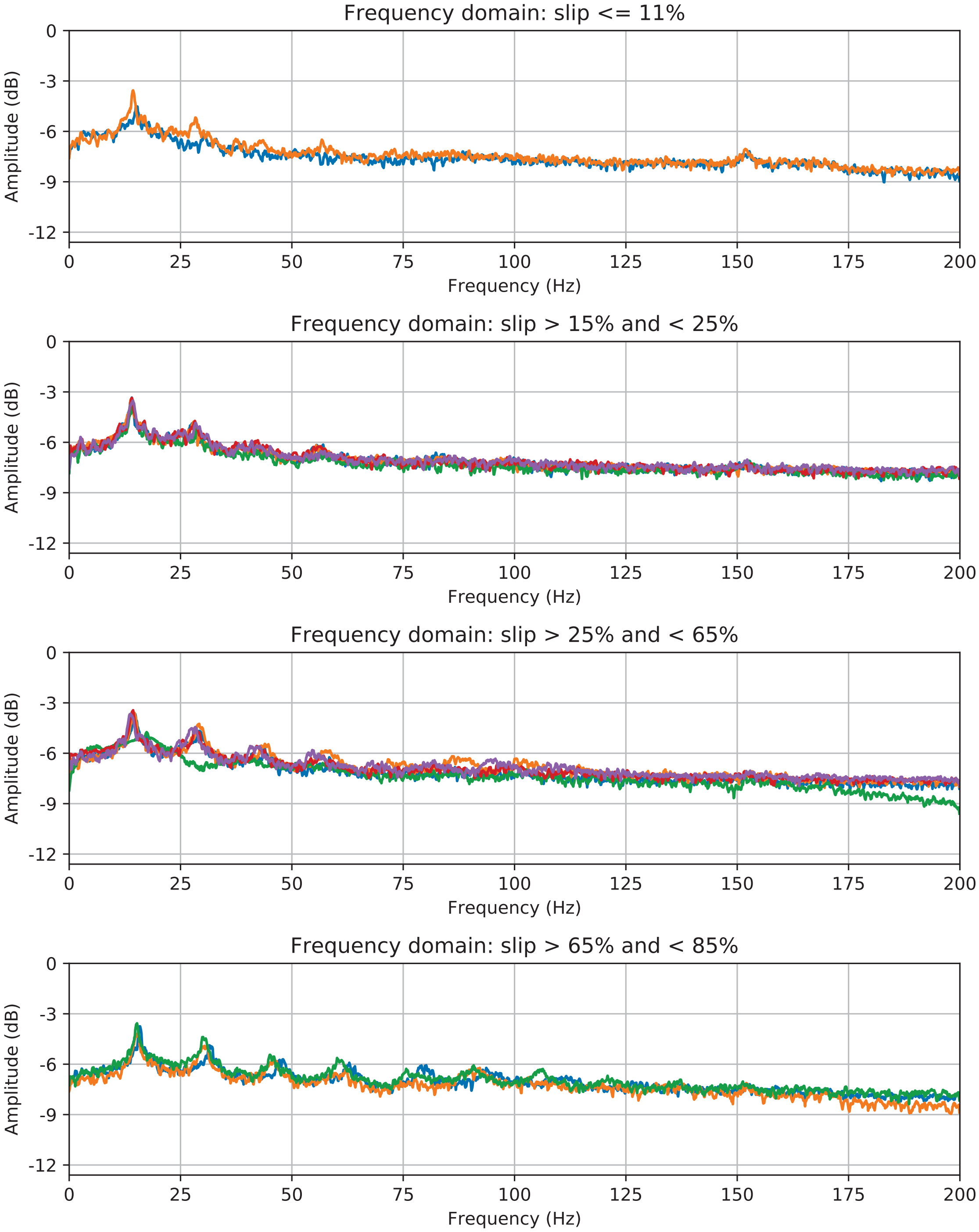

Figure A.14: Frequency spectrum of vibrations in z-axis linear acceleration measured by IMU2 during induced slip tests at 20 cm/s at the CSA's outdoor facility separated according to slip %.

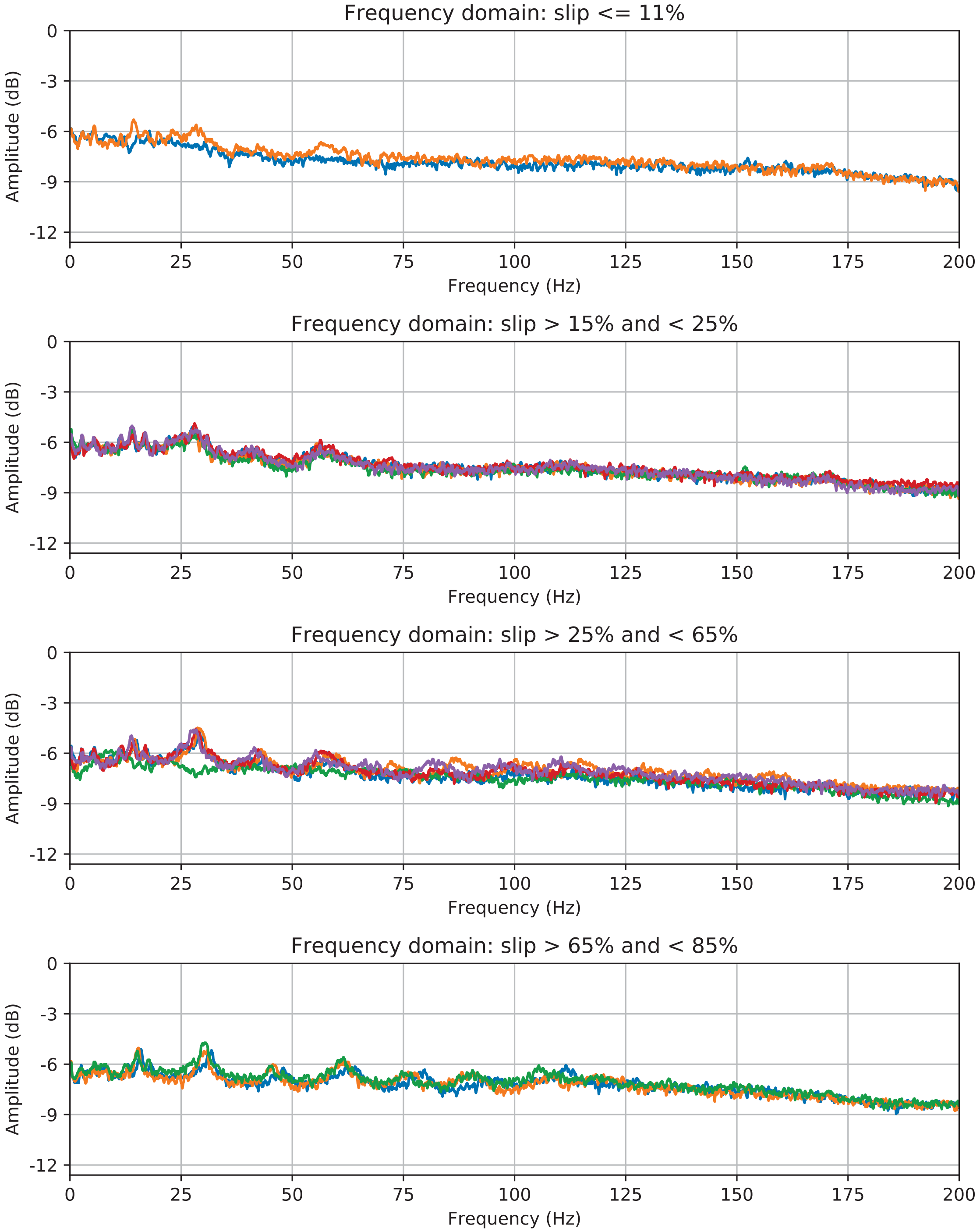

Figure A.15: Frequency spectrum of vibrations in y-axis linear acceleration measured by IMU1 during induced slip tests at 20 cm/s at the CSA's outdoor facility separated according to slip %.

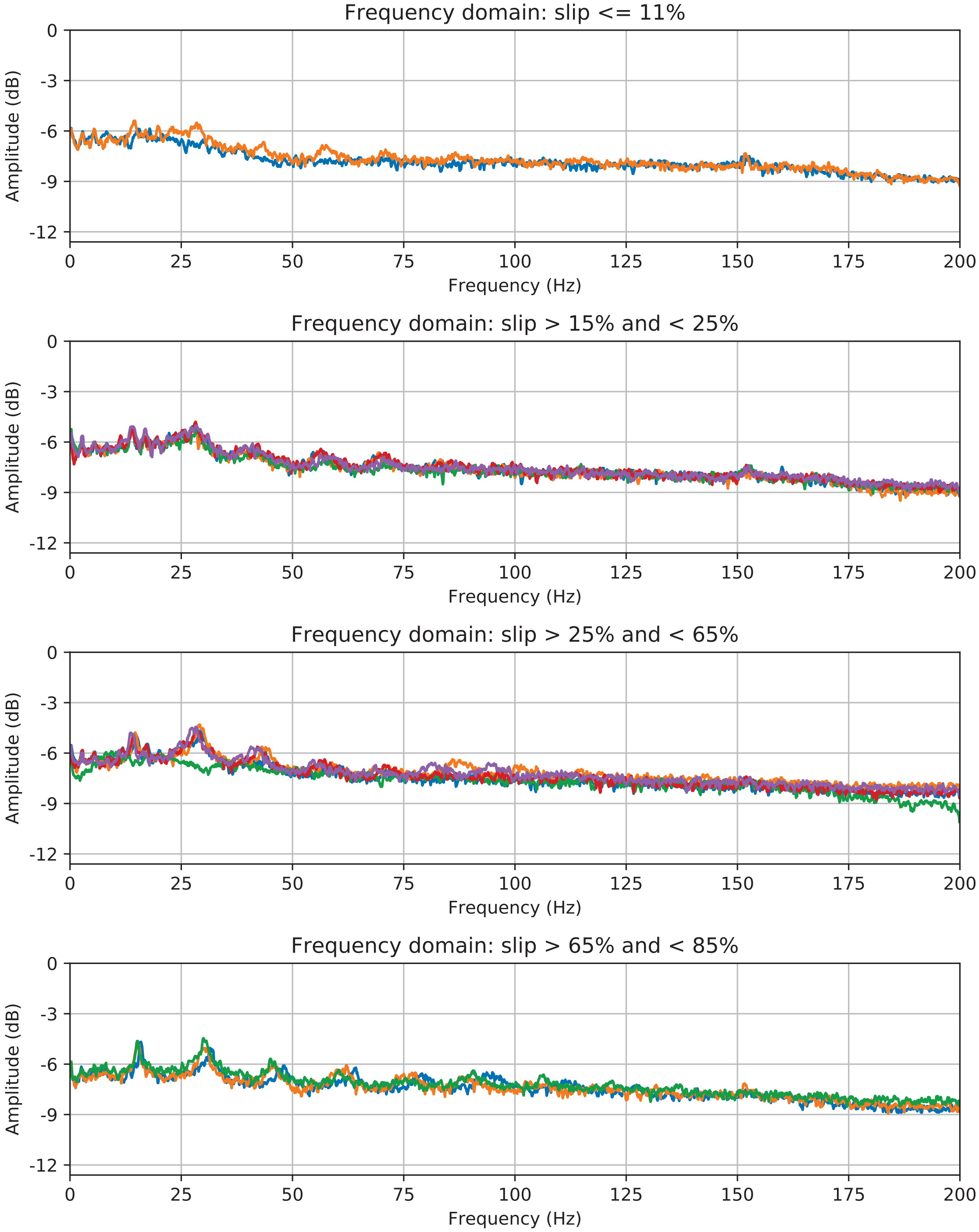

Figure A.16: Frequency spectrum of vibrations in y-axis linear acceleration measured by IMU2 during induced slip tests at 20 cm/s at the CSA's outdoor facility separated according to slip %.

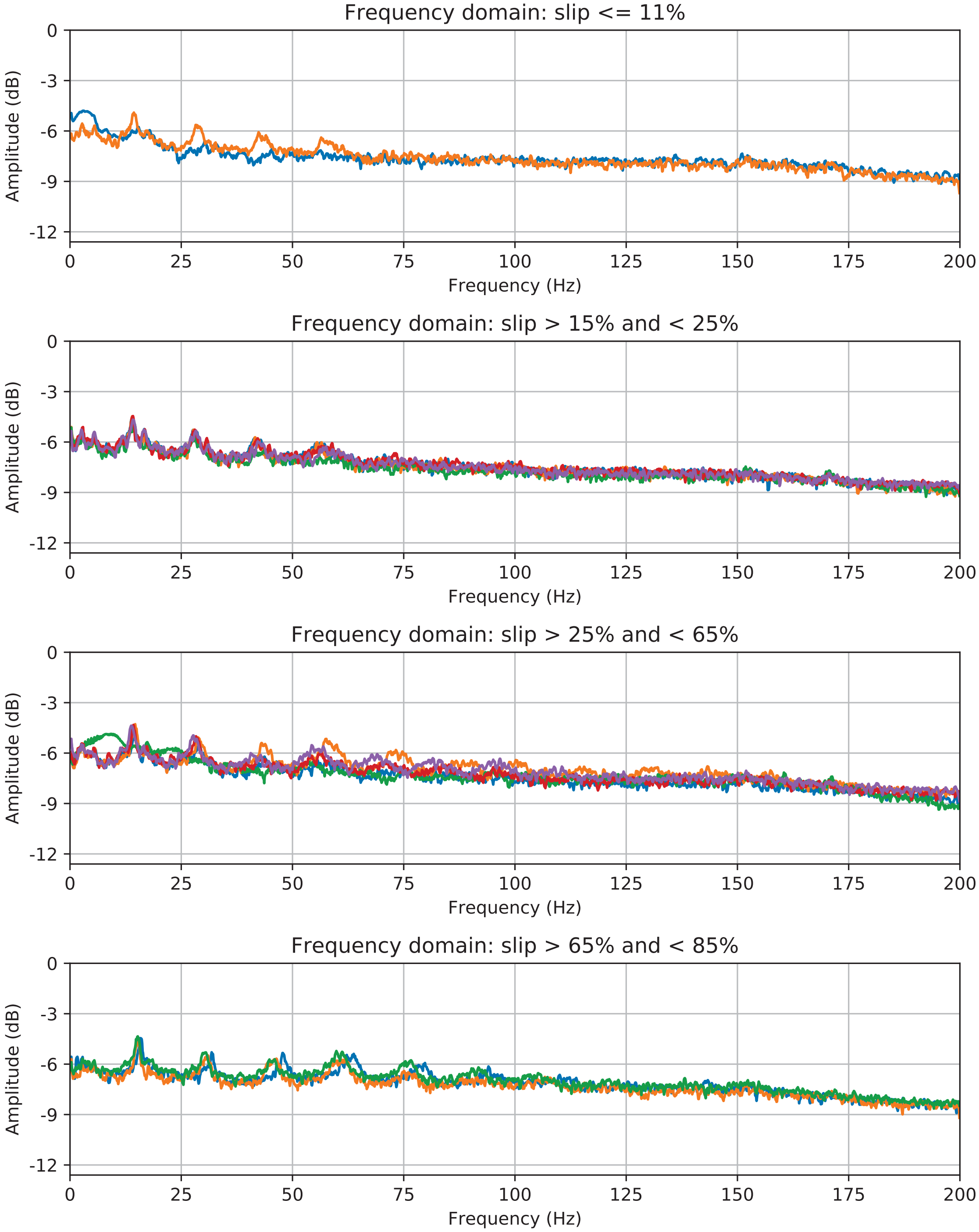
Frequency domain: slip <= 11%

Frequency domain: slip > 15% and < 25%

Frequency domain: slip > 25% and < 65%

Frequency domain: slip > 65% and < 85%

Figure A.17: Frequency spectrum of vibrations in x-axis linear acceleration measured by IMU1 during induced slip tests at 20 cm/s at the CSA's outdoor facility separated according to slip %.

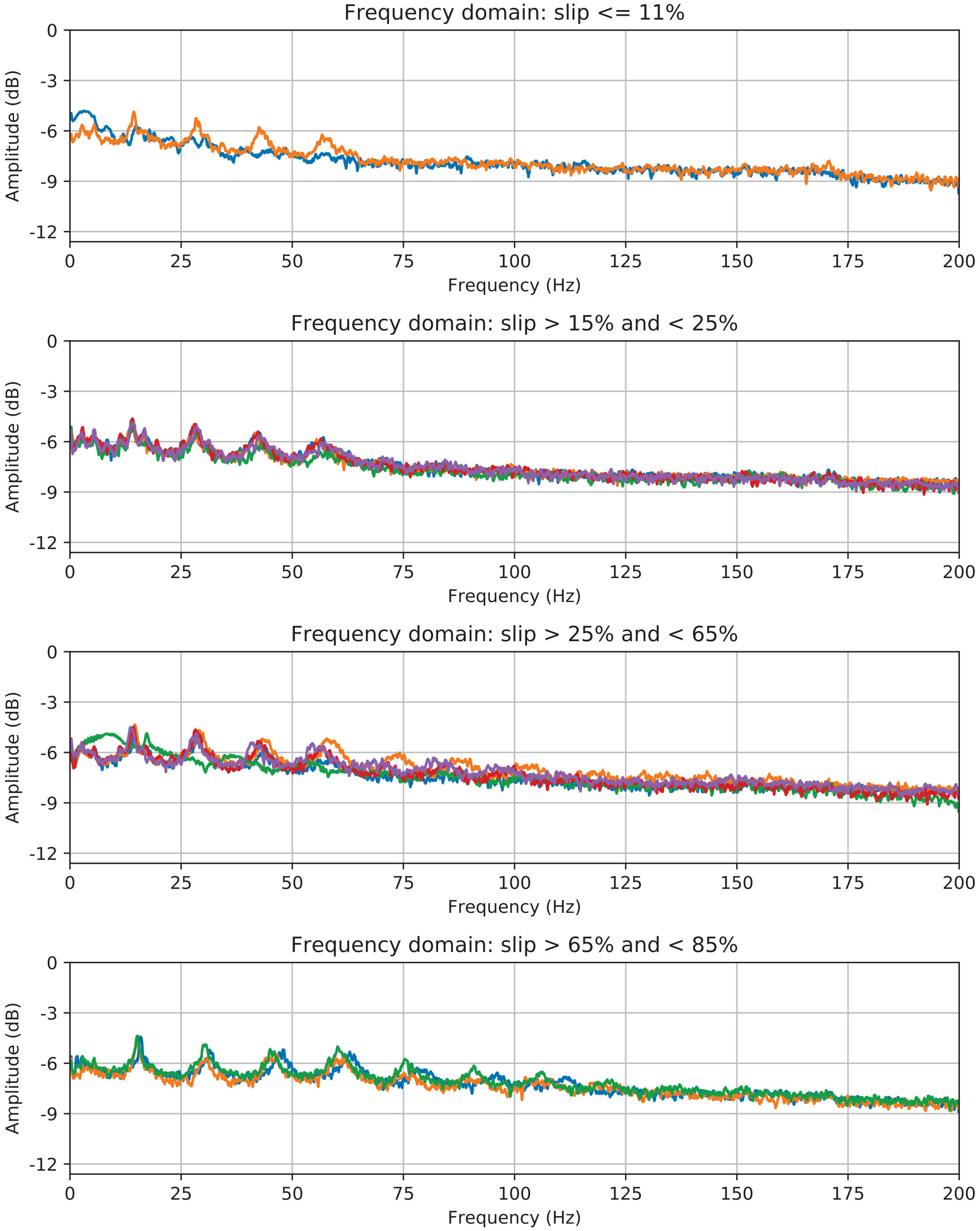

Figure A.18: Frequency spectrum of vibrations in x-axis linear acceleration measured by IMU2 during induced slip tests at 20 cm/s at the CSA's outdoor facility separated according to slip %.

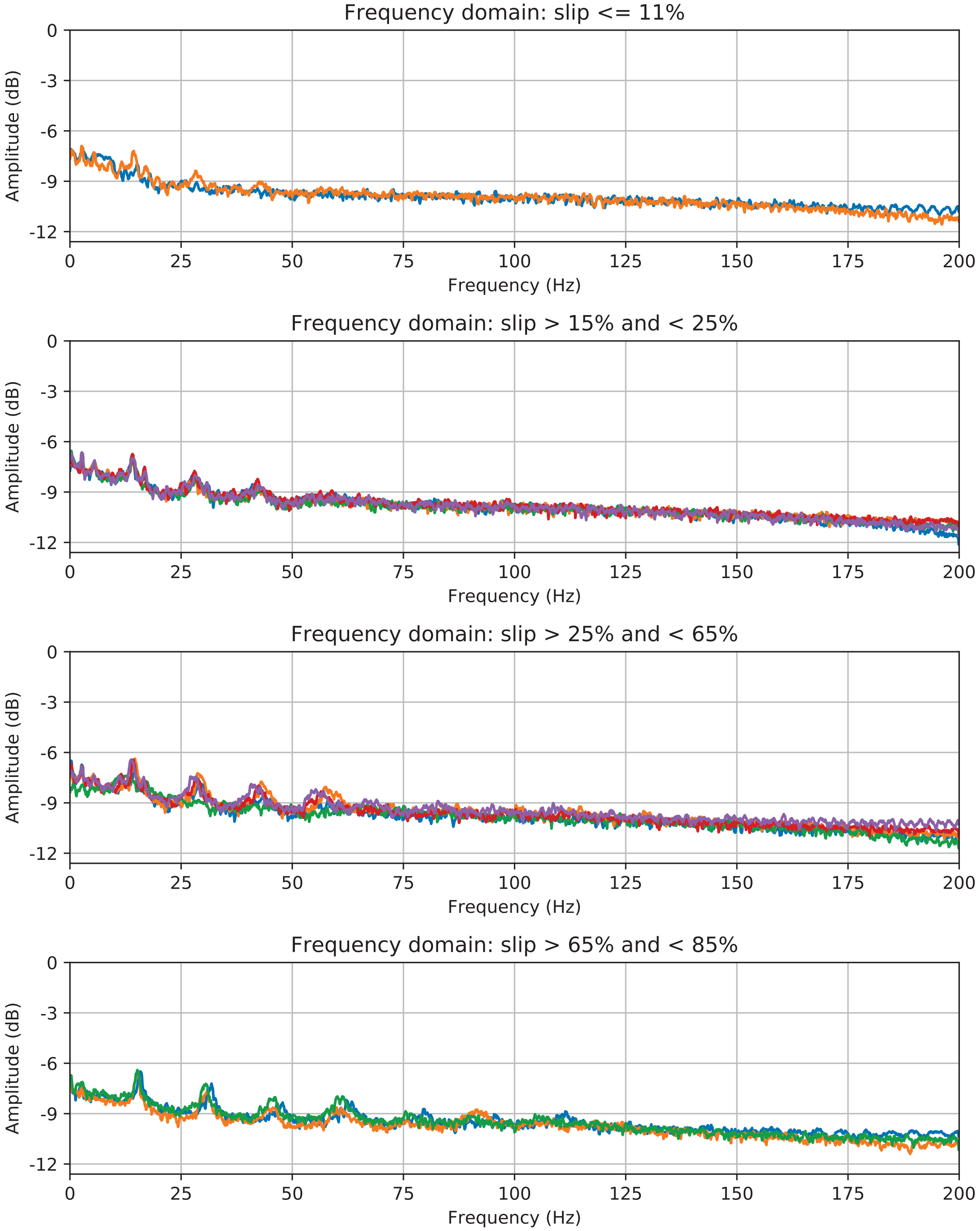

Figure A.19: Frequency spectrum of vibrations in z-axis angular velocity measured by IMU1 during induced slip tests at 20 cm/s at the CSA's outdoor facility separated according to slip %.

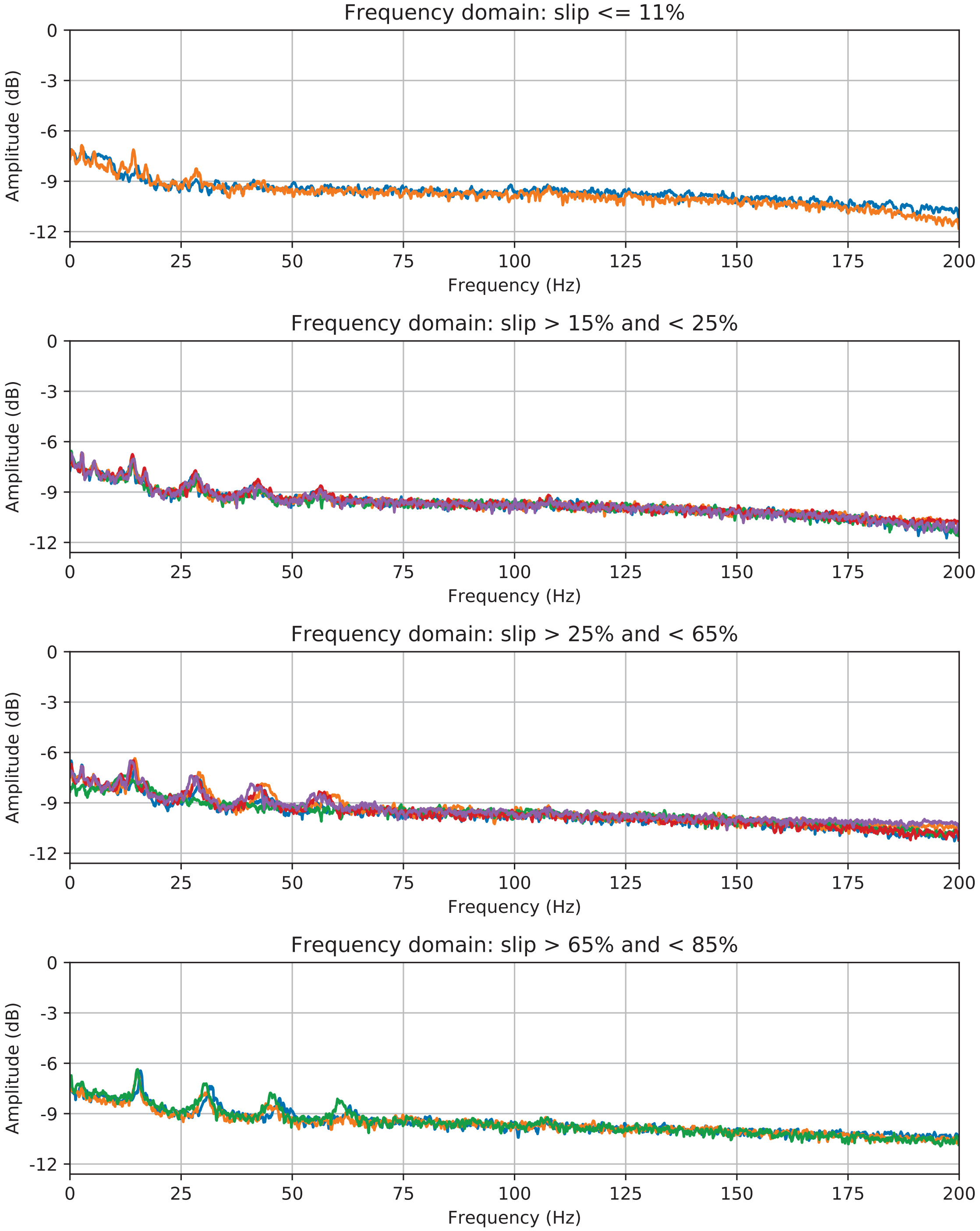
Frequency domain: slip <= 11%

Frequency domain: slip > 15% and < 25%

Frequency domain: slip > 25% and < 65%

Frequency domain: slip > 65% and < 85%

Figure A.20: Frequency spectrum of vibrations in z-axis angular velocity measured by IMU2 during induced slip tests at 20 cm/s at the CSA's outdoor facility separated according to slip %.

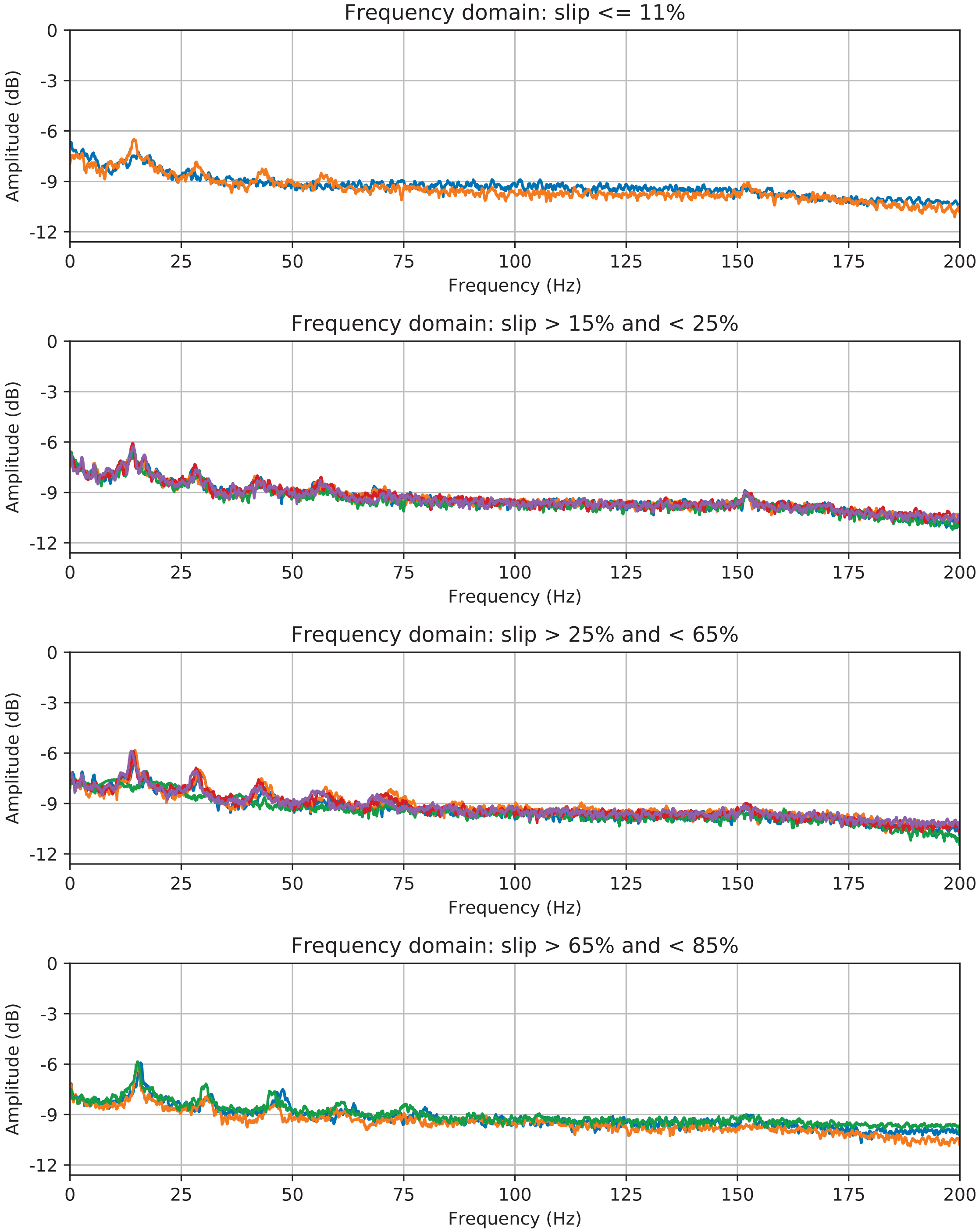

Frequency domain: slip <= 11%

Frequency domain: slip > 15% and < 25%

Frequency domain: slip > 25% and < 65%

Frequency domain: slip > 65% and < 85%

Figure A.21: Frequency spectrum of vibrations in y-axis angular velocity measured by IMU1 during induced slip tests at 20 cm/s at the CSA's outdoor facility separated according to slip %.

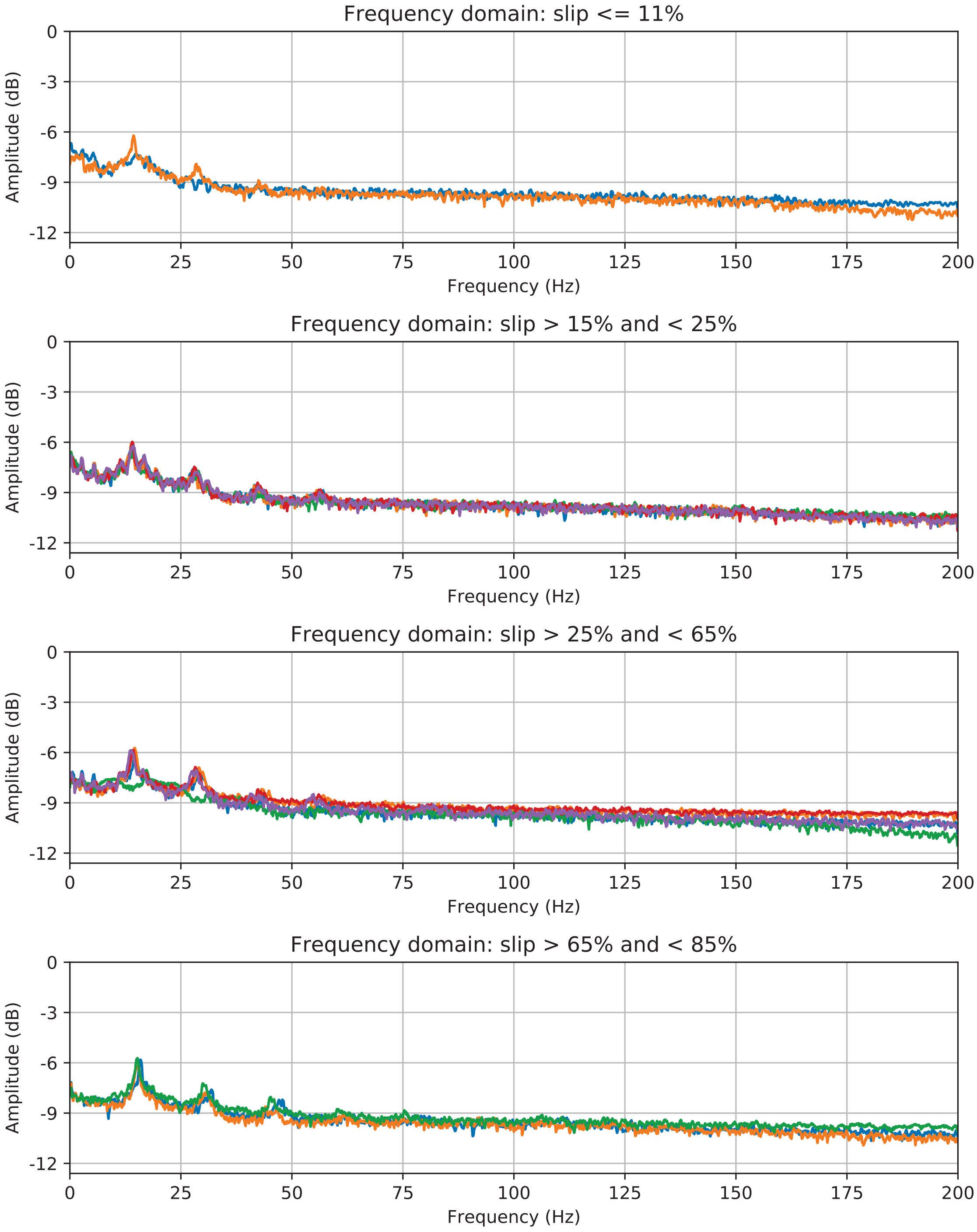

Figure A.22: Frequency spectrum of vibrations in y-axis angular velocity measured by IMU2 during induced slip tests at 20 cm/s at the CSA's outdoor facility separated according to slip %.

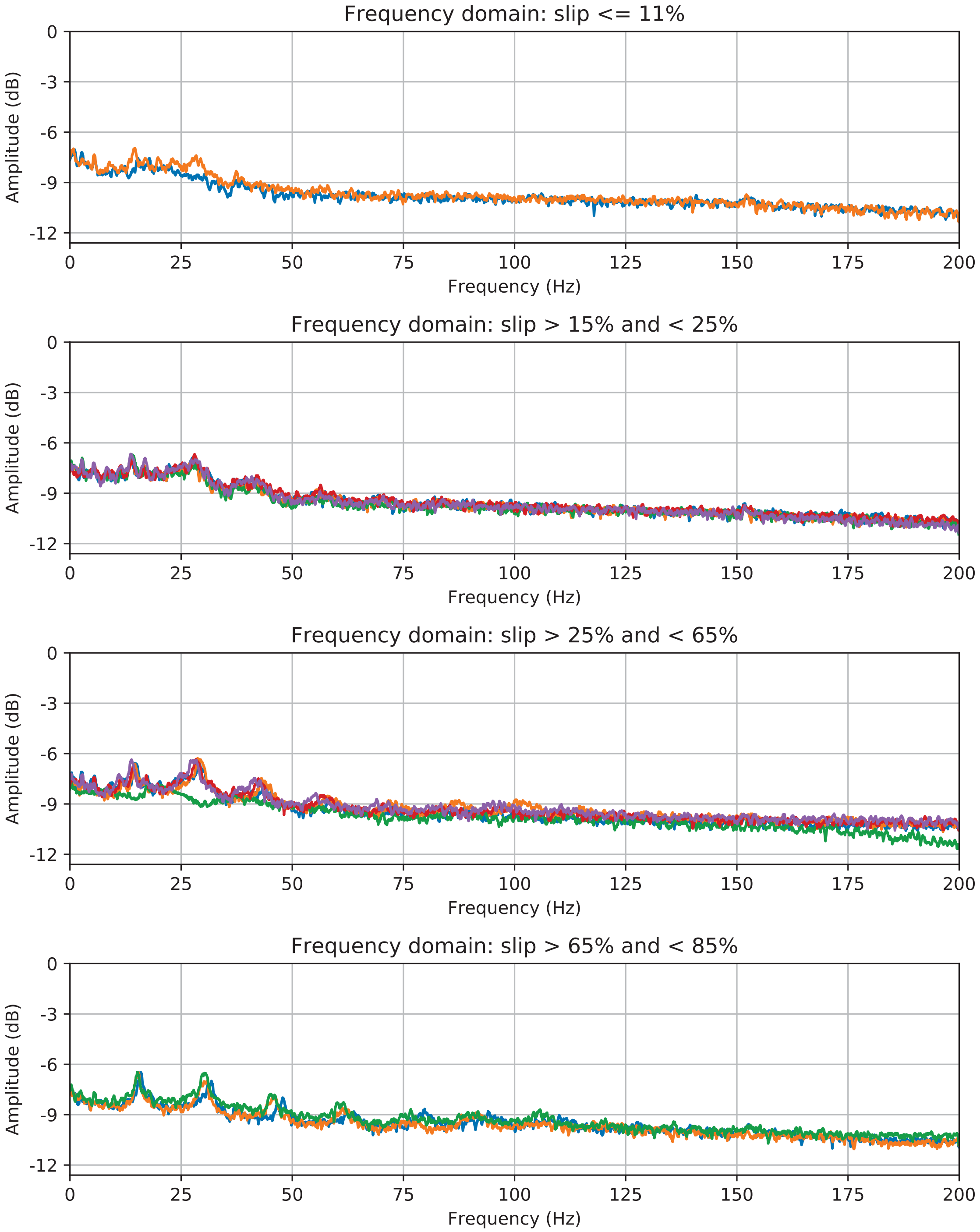

Figure A.23: Frequency spectrum of vibrations in x-axis angular velocity measured by IMU1 during induced slip tests at 20 cm/s at the CSA's outdoor facility separated according to slip %.

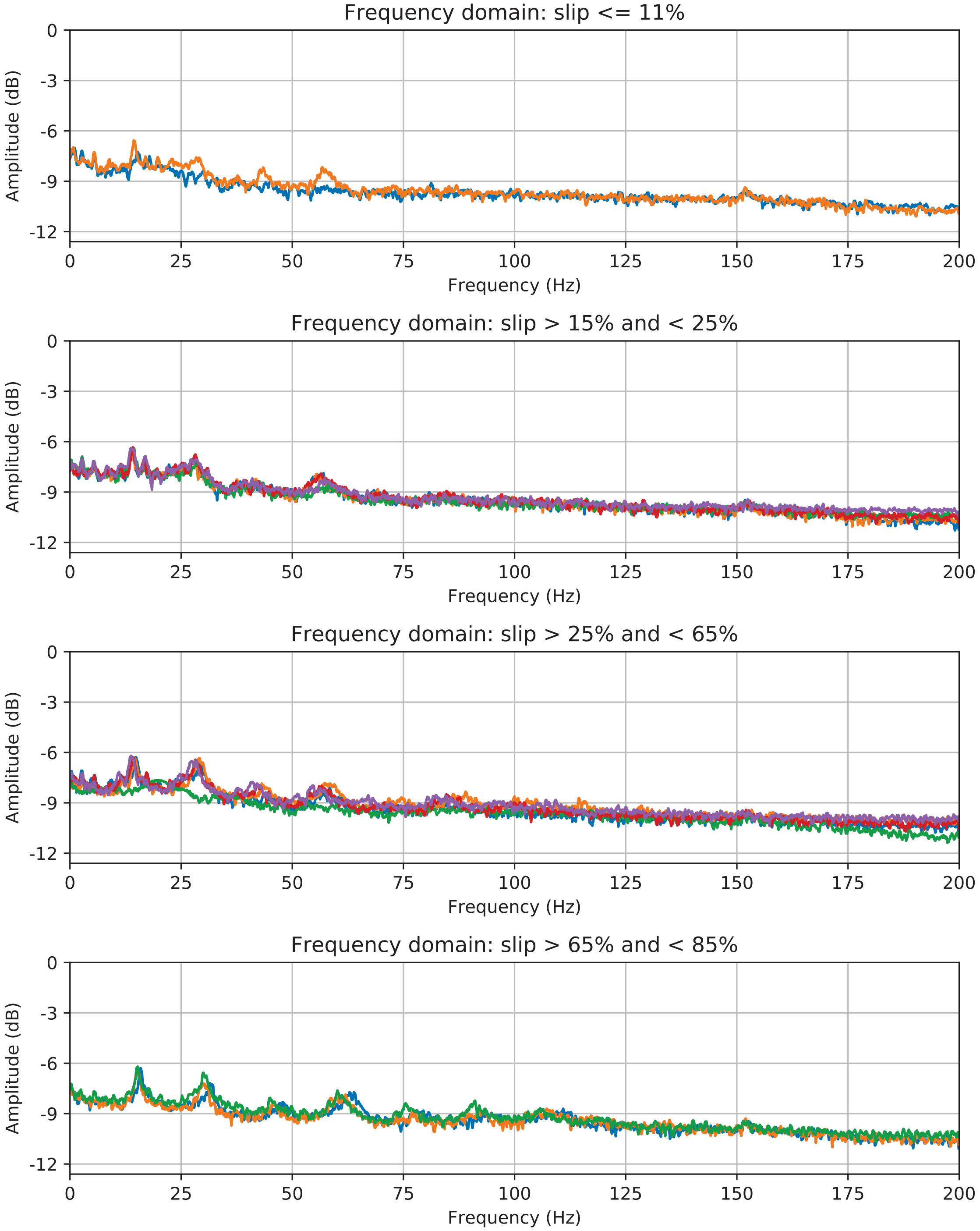

Figure A.24: Frequency spectrum of vibrations in x-axis angular velocity measured by IMU2 during induced slip tests at 20 cm/s at the CSA's outdoor facility separated according to slip %.

Appendix B

SVM performance plots

B.1 Validation ROC AUC plots compared to Test ROC AUC plots

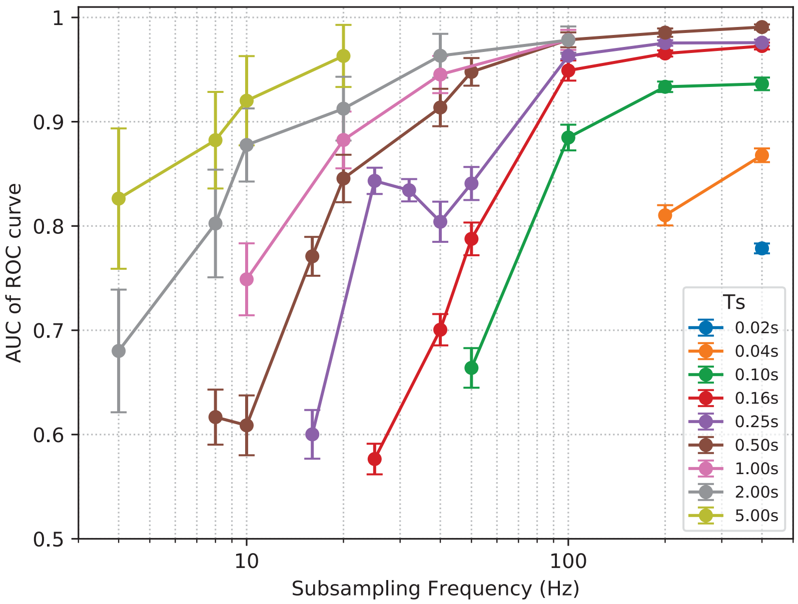

Figure B.1: Plot of ROC AUC for SVM classifiers trained with various sampling time and frequency of z-axis linear acceleration measured by IMU1.

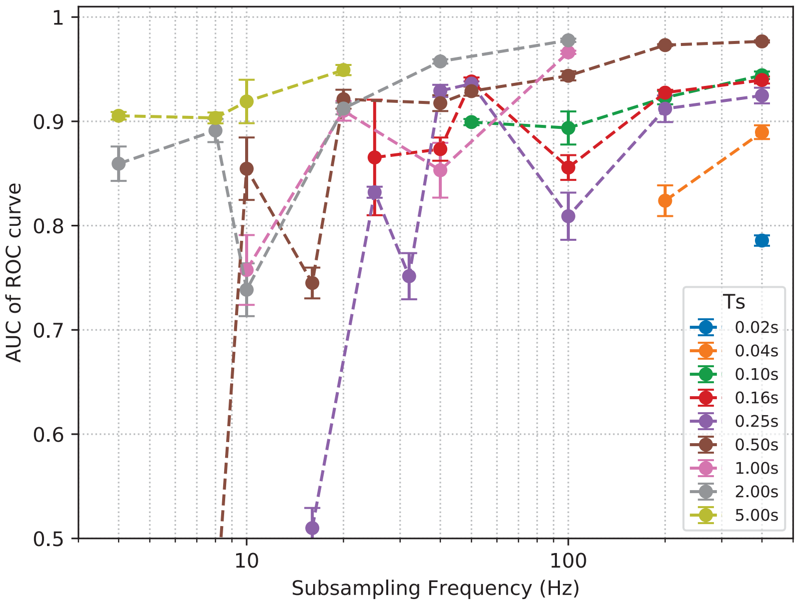

Figure B.2: Plot of ROC AUC for SVM classifiers trained with various sampling time and frequency of z-axis linear acceleration measured by IMU1 and applied to slope test data.

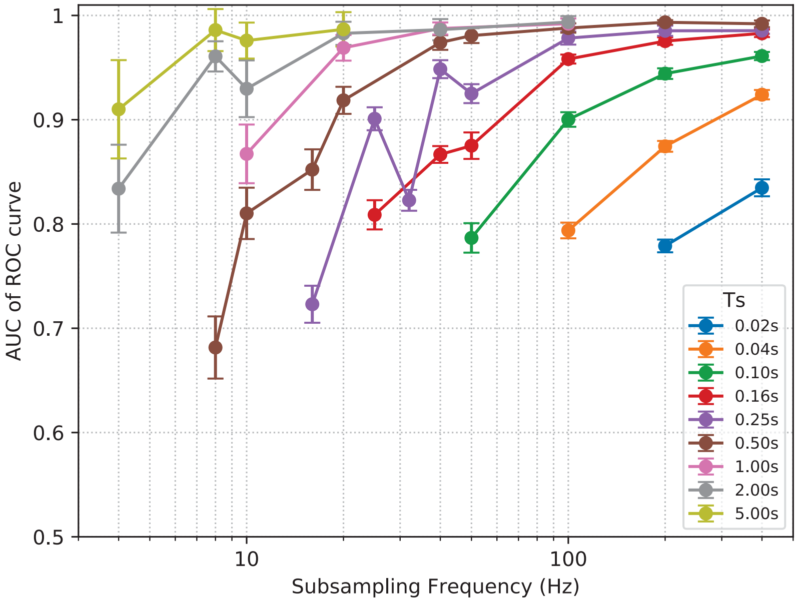

Figure B.3: Plot of ROC AUC for SVM classifiers trained with various sampling time and frequency of y-axis linear acceleration measured by IMU1.

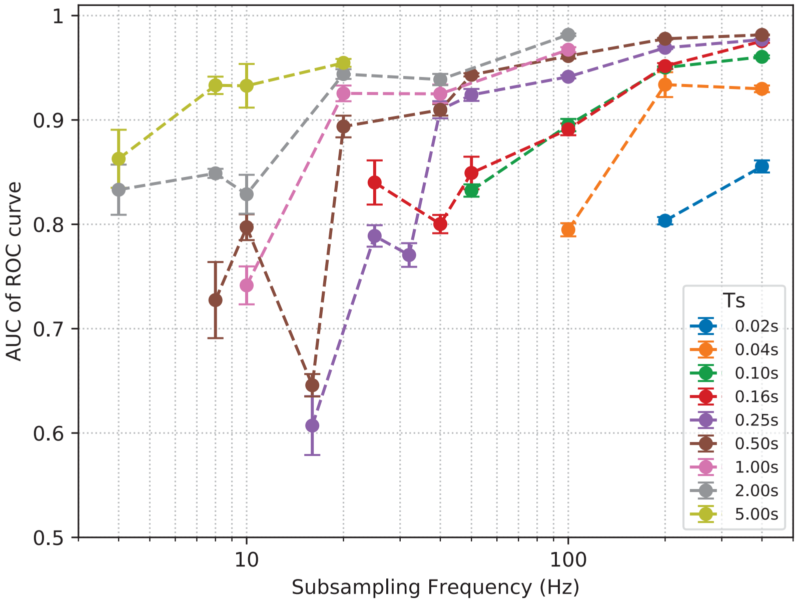

Figure B.4: Plot of ROC AUC for SVM classifiers trained with various sampling time and frequency of y-axis linear acceleration measured by IMU1 and applied to slope test data.

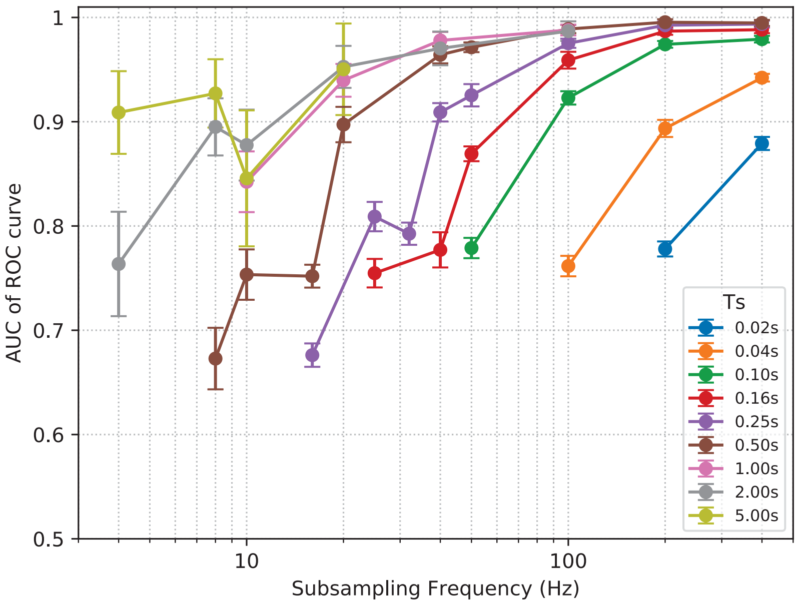

Figure B.5: Plot of ROC AUC for SVM classifiers trained with various sampling time and frequency of x-axis linear acceleration measured by IMU1.

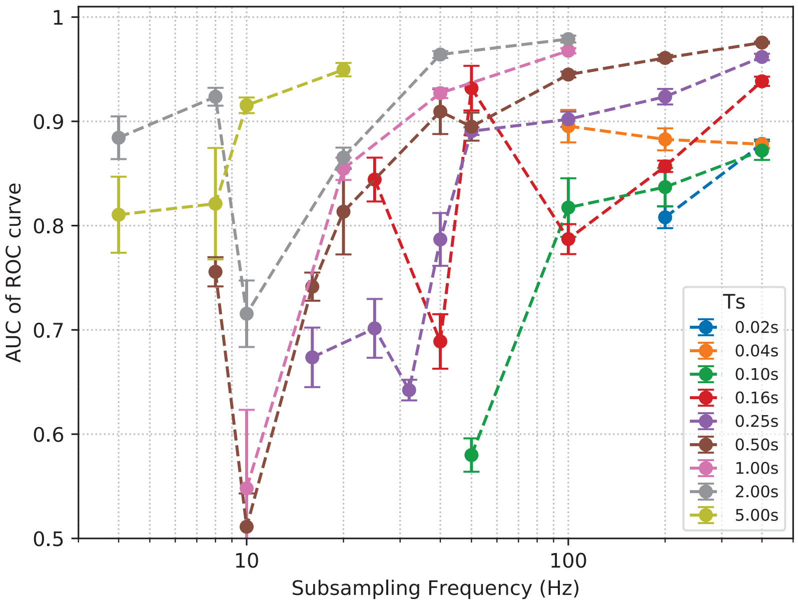

Figure B.6: Plot of ROC AUC for SVM classifiers trained with various sampling time and frequency of x-axis linear acceleration measured by IMU1 and applied to slope test data.

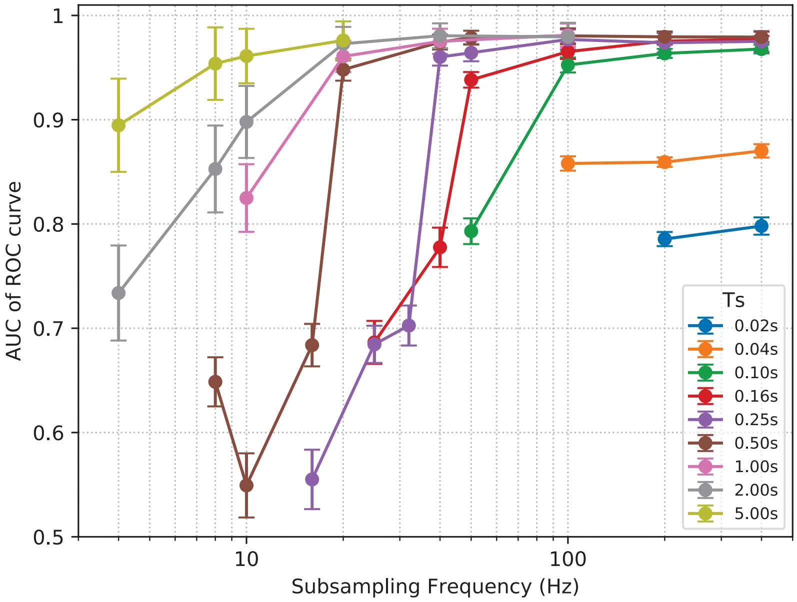

Figure B.7: Plot of ROC AUC for SVM classifiers trained with various sampling time and frequency of z-axis angular velocity measured by IMU1.

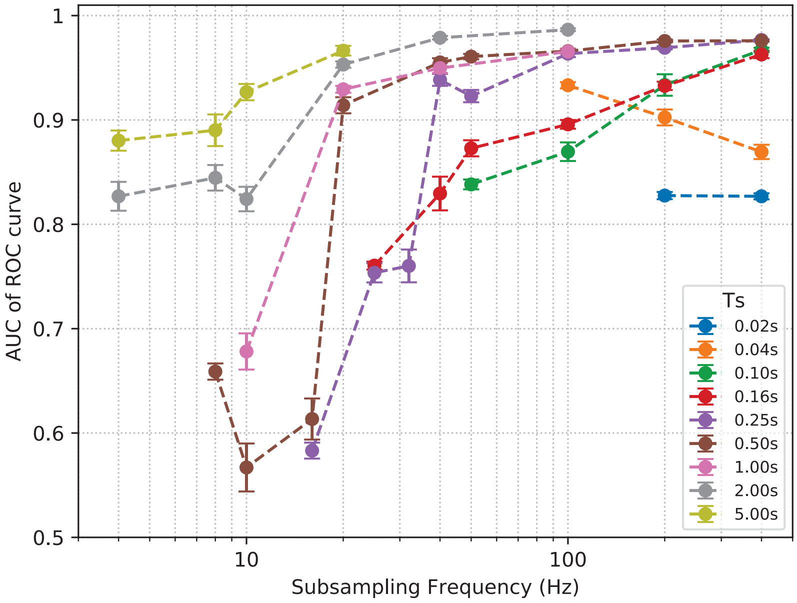

Figure B.8: Plot of ROC AUC for SVM classifiers trained with various sampling time and frequency of z-axis angular velocity measured by IMU1 and applied to slope test data.

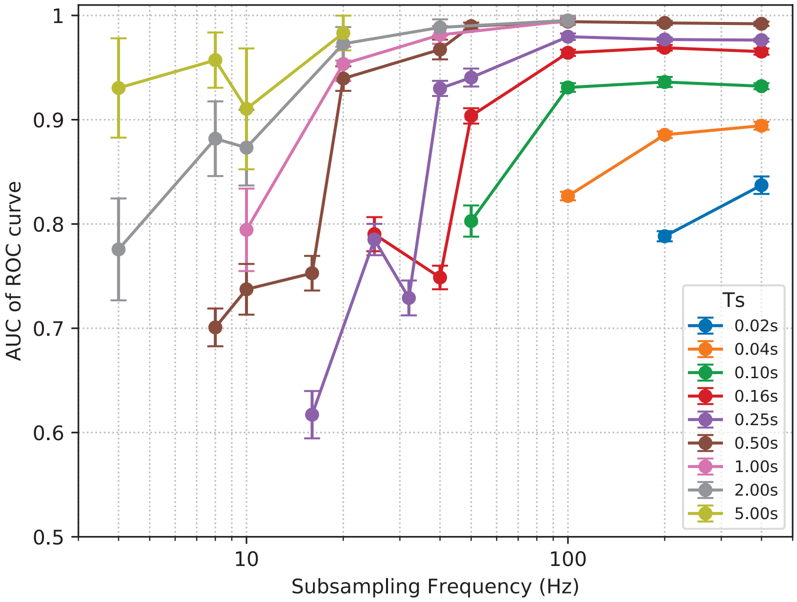

Figure B.9: Plot of ROC AUC for SVM classifiers trained with various sampling time and frequency of y-axis angular velocity measured by IMU1.

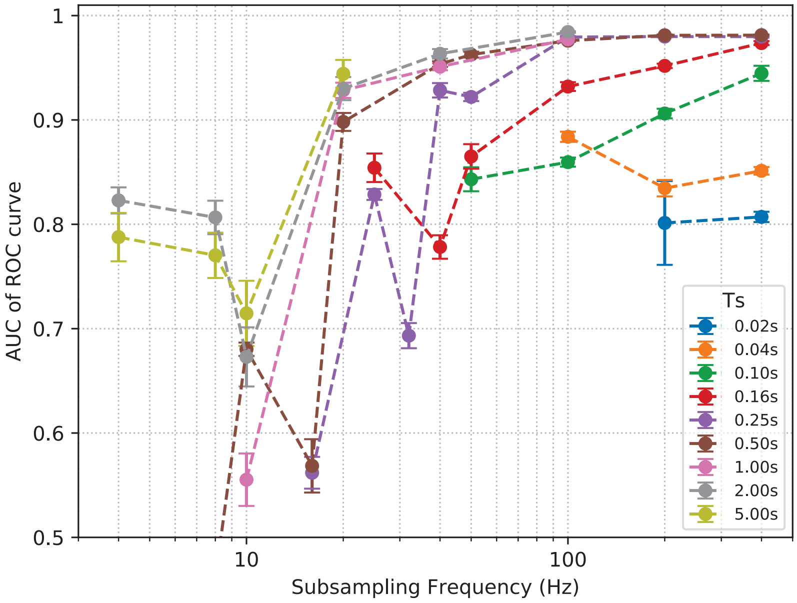

Figure B.10: Plot of ROC AUC for SVM classifiers trained with various sampling time and frequency of y-axis angular velocity measured by IMU1 and applied to slope test data.

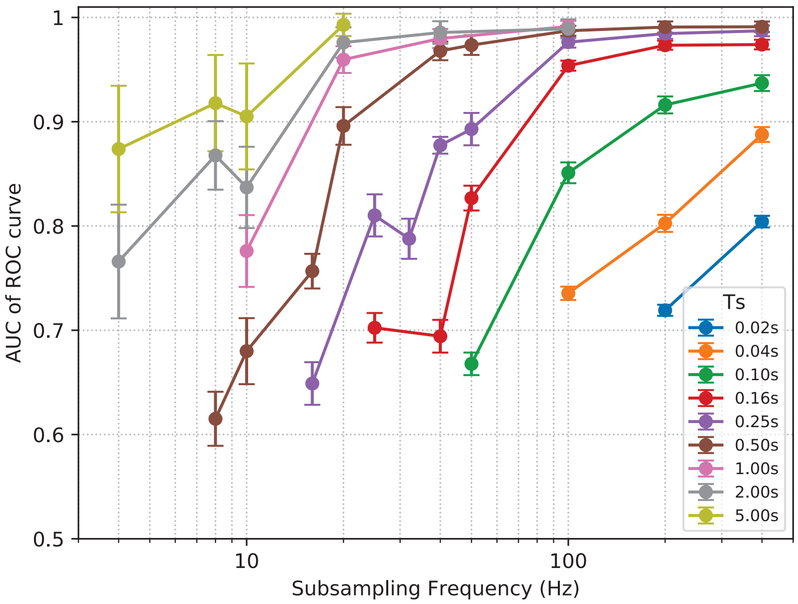

Figure B.11: Plot of ROC AUC for SVM classifiers trained with various sampling time and frequency of x-axis angular velocity measured by IMU1.

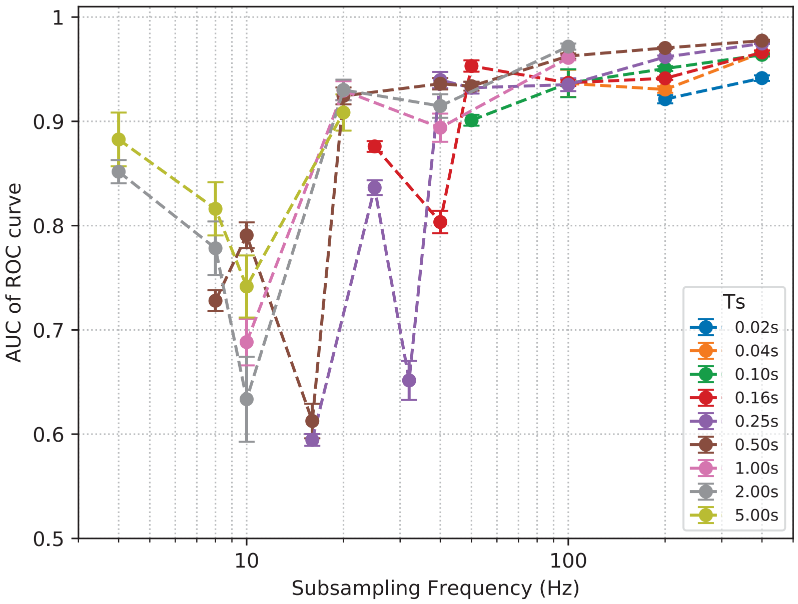

Figure B.12: Plot of ROC AUC for SVM classifiers trained with various sampling time and frequency of x-axis angular velocity measured by IMU1 and applied to slope test data.

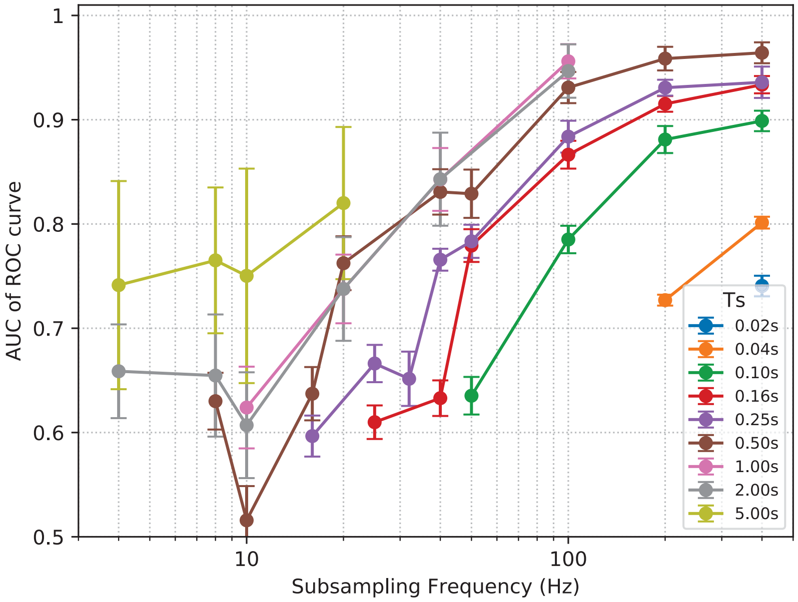

Figure B.13: Plot of ROC AUC for SVM classifiers trained with various sampling time and frequency of z-axis linear acceleration measured by IMU2.

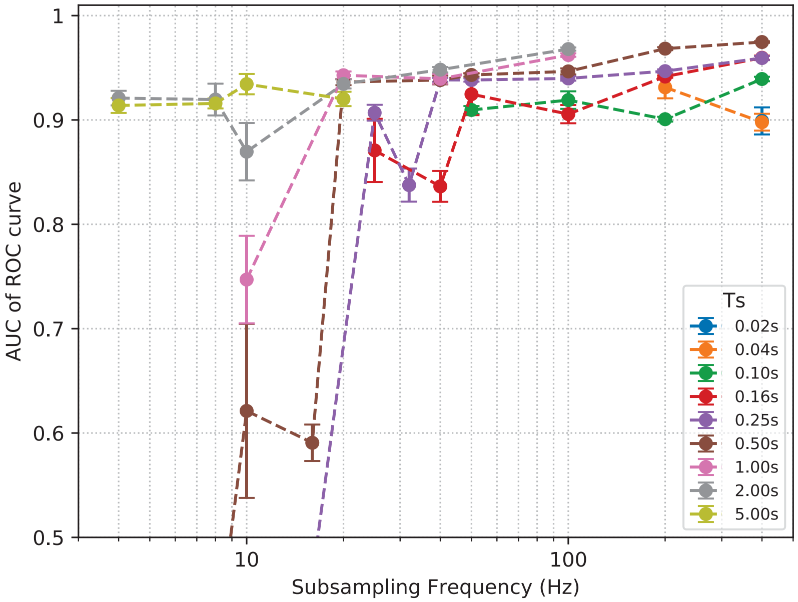

Figure B.14: Plot of ROC AUC for SVM classifiers trained with various sampling time and frequency of z-axis linear acceleration measured by IMU2 and applied to slope test data.

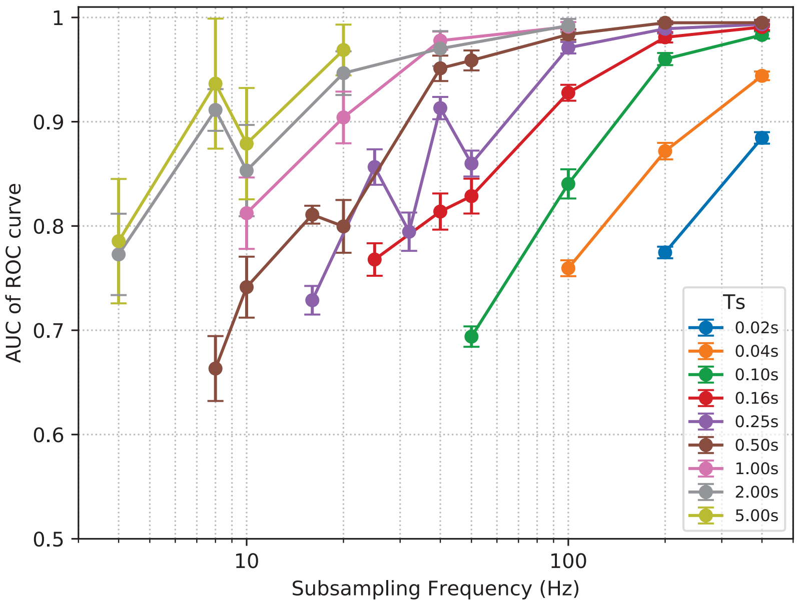

Figure B.15: Plot of ROC AUC for SVM classifiers trained with various sampling time and frequency of y-axis linear acceleration measured by IMU2.

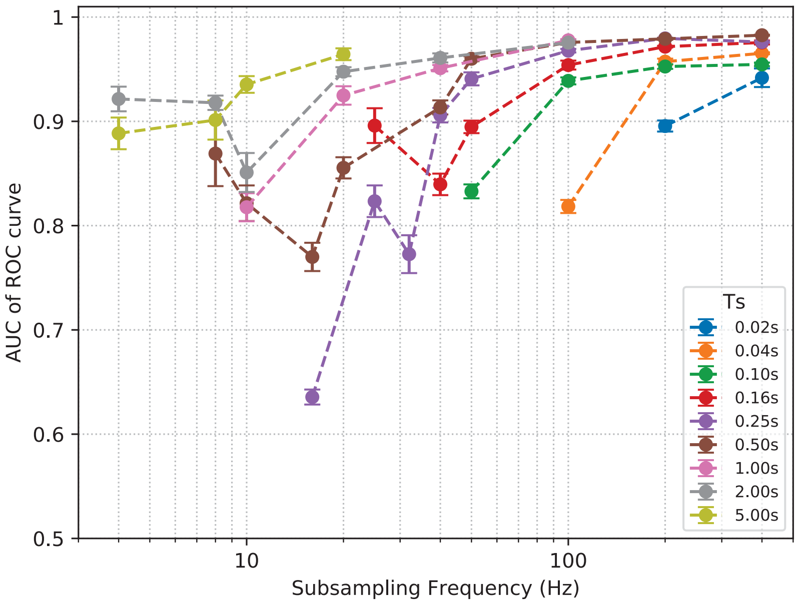

Figure B.16: Plot of ROC AUC for SVM classifiers trained with various sampling time and frequency of y-axis linear acceleration measured by IMU2 and applied to slope test data.

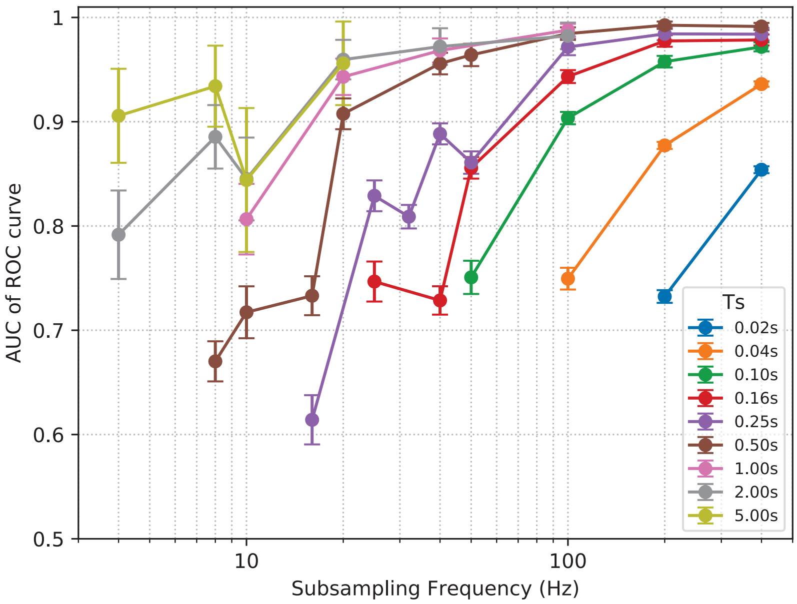

Figure B.17: Plot of ROC AUC for SVM classifiers trained with various sampling time and frequency of x-axis linear acceleration measured by IMU2.

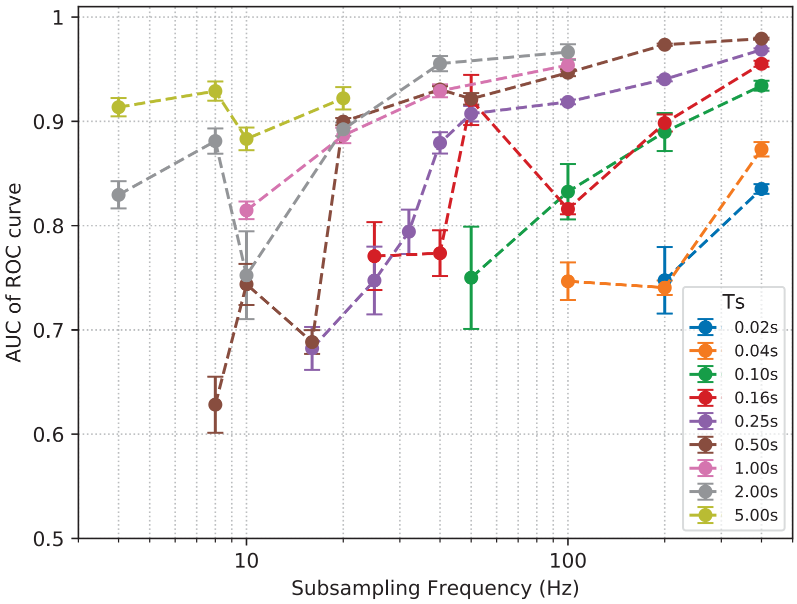

Figure B.18: Plot of ROC AUC for SVM classifiers trained with various sampling time and frequency of x-axis linear acceleration measured by IMU2 and applied to slope test data.

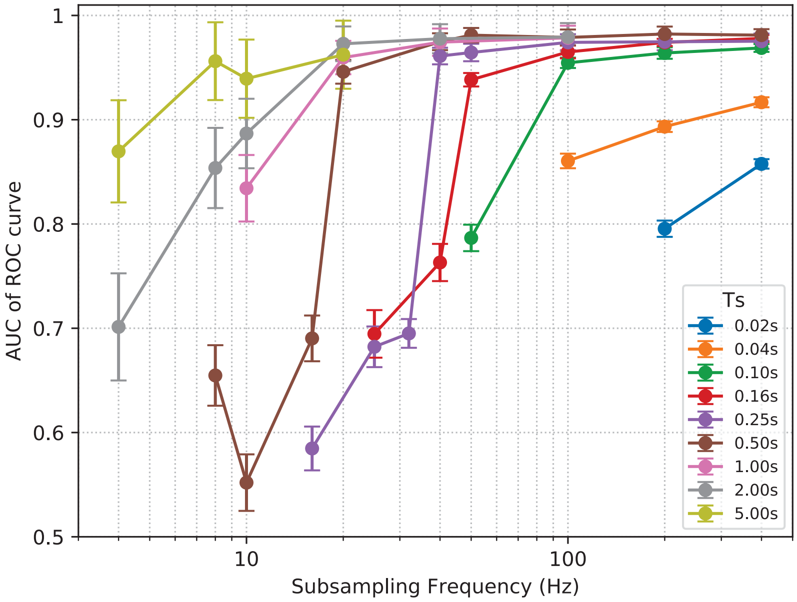

Figure B.19: Plot of ROC AUC for SVM classifiers trained with various sampling time and frequency of z-axis angular velocity measured by IMU2.

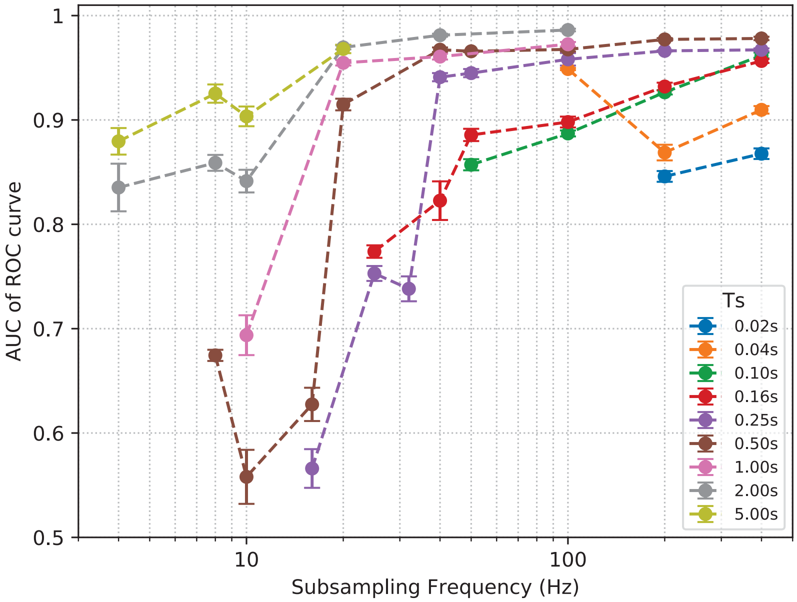

Figure B.20: Plot of ROC AUC for SVM classifiers trained with various sampling time and frequency of z-axis angular velocity measured by IMU2 and applied to slope test data.

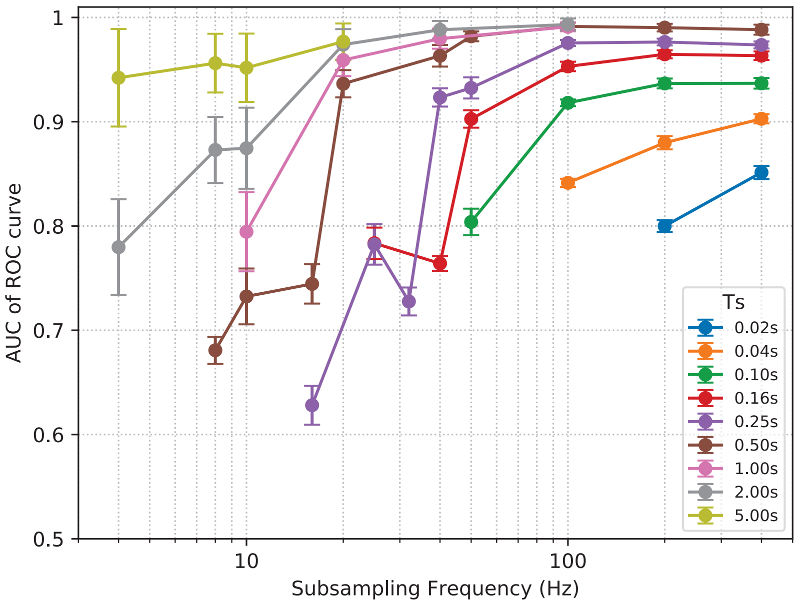

Figure B.21: Plot of ROC AUC for SVM classifiers trained with various sampling time and frequency of y-axis angular velocity measured by IMU2.

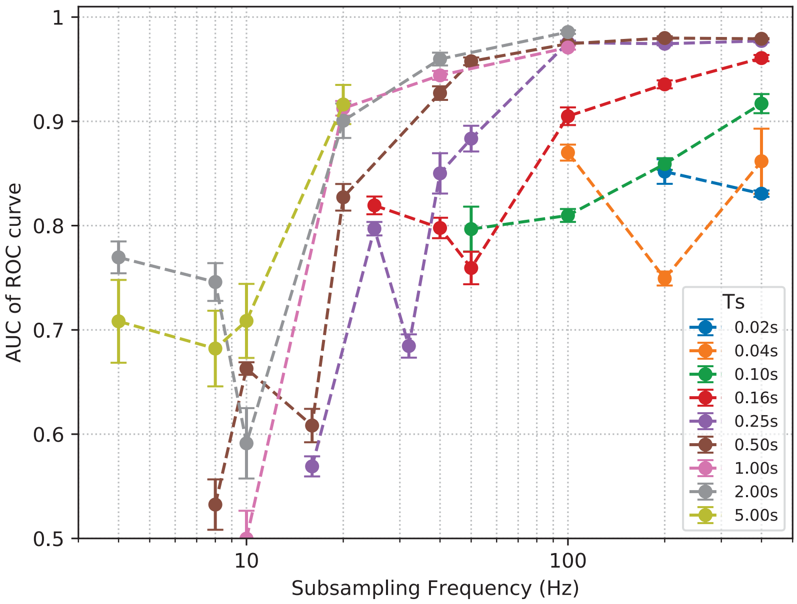

Figure B.22: Plot of ROC AUC for SVM classifiers trained with various sampling time and frequency of y-axis angular velocity measured by IMU2 and applied to slope test data.

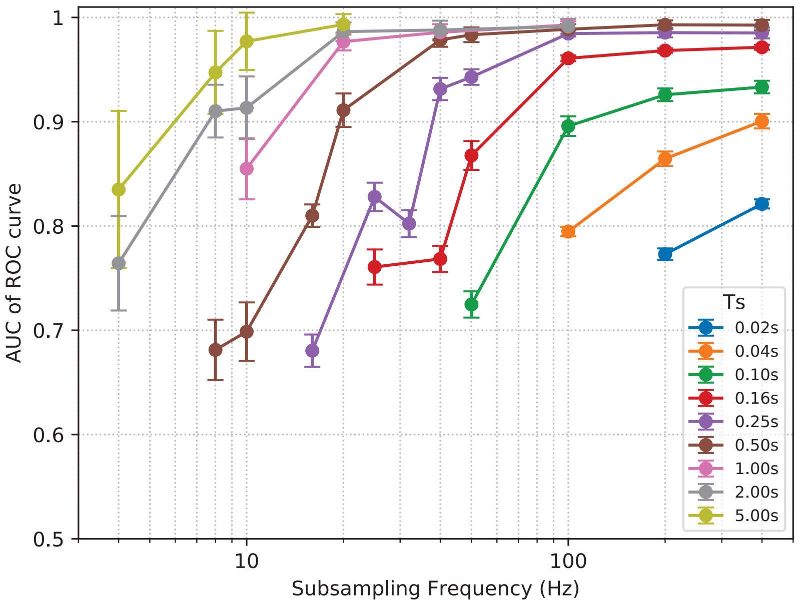

Figure B.23: Plot of ROC AUC for SVM classifiers trained with various sampling time and frequency of x-axis angular velocity measured by IMU2.

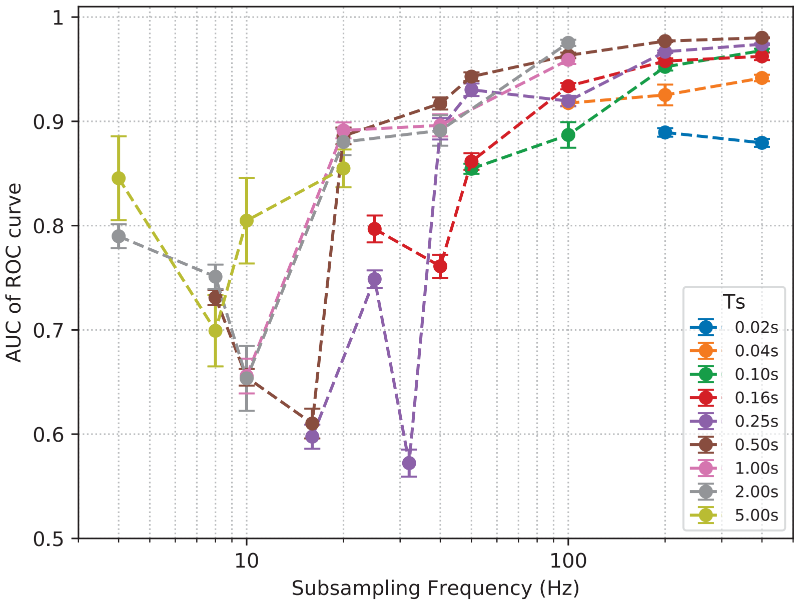

Figure B.24: Plot of ROC AUC for SVM classifiers trained with various sampling time and frequency of x-axis angular velocity measured by IMU2 and applied to slope test data.

References

Abdiansah, A., & Wardoyo, R. (2015). Time complexity analysis of support vector machines (svm) in libsvm. *International journal computer and application*, *128*(3), 28–34.

Arvidson, R. E., Ashley, J. W., Bell III, J. F., Chojnacki, M., Cohen, J., Economou, T., ... others (2011). Opportunity mars rover mission: Overview and selected results from purgatory ripple to traverses to endeavour crater. *Journal of Geophysical Research: Planets*, *116*(E7).

Arvidson, R. E., Bell III, J. F., Bellutta, P., Cabrol, N. A., Catalano, J., Cohen, J., ... others (2010). Spirit mars rover mission: Overview and selected results from the northern home plate winter haven to the side of scamander crater. *Journal of Geophysical Research: Planets*, *115*(E7).

Arvidson, R. E., Iagnemma, K. D., Maimone, M., Fraeman, A. A., Zhou, F., Heverly, M. C., ... others (2017). Mars science laboratory curiosity rover megaripple crossings up to sol 710 in gale crater. *Journal of Field Robotics*, *34*(3), 495–518. `https://doi.org/10.1002/rob.21647`.

Bekker, M. G. (1956). Theory of land locomotion. *Ann Arbor*.

Bekker, M. G. (1960). Off-the-road locomotion. *Research and development in terramechanics*.

Bouguelia, M.-R., Gonzalez, R., Iagnemma, K., & Byttner, S. (2017). Unsupervised classification of slip events for planetary exploration rovers. *Journal of Terramechanics*, *73*, 95–106. `https://doi.org/10.1016/j.jterra.2017.09.001`.

Brooks, C. A., & Iagnemma, K. (2012). Self-supervised terrain classification for planetary surface exploration rovers. *Journal of Field Robotics*, *29*(3), 445–468. `https://doi.org/10.1002/rob.21408`.

Bussmann, K., Meyer, L., Steidle, F., & Wedler, A. (2018). Slip modeling and estimation for a planetary exploration rover: Experimental results from mt. etna. In *2018 ieee/rsj international* *conference on intelligent robots and systems (iros)* (pp. 2449–2456). https://doi.org/10.1109/IROS.2018.8594294.

Canadian Space Agency. (n.d.). *Analogue terrain.* Retrieved 2022-04-04, from https://www.asc-csa.gc.ca/eng/laboratories-and-warehouse/analogue-terrain.asp (Last Modified: 2021-08-06)

Cheng, Y., Maimone, M., & Matthies, L. (2005). Visual odometry on the mars exploration rovers. In *2005 ieee international conference on systems, man and cybernetics* (Vol. 1, pp. 903–910). https://doi.org/10.1109/ICSMC.2005.1571261.

Cortes, C., & Vapnik, V. (1995). Support-vector networks. *Machine learning*, *20*, 273–297.

Creager, C., Asnani, V., Oravec, H., & Woodward, A. (2017, August). *Drawbar Pull (DP) Procedures for Off-Road Vehicle Testing.* Retrieved 2022-04-21, from https://ntrs.nasa.gov/citations/20170010706 (NTRS Author Affiliations: NASA Glenn Research Center, Akron Univ., Virginia Polytechnic Inst. and State Univ. NTRS Report/Patent Number: GRC-E-DAA-TN31725 NTRS Document ID: 20170010706 NTRS Research Center: Glenn Research Center (GRC))

Daca, A., Nassiraei, A. A. F., Tremblay, D., & Skonieczny, K. (2022). Comparison of wheel load application methods in single-wheel testbeds. *Journal of Terramechanics*, *99*, 35–55.

Fiset, J.-S. (2019). *Effects of turning radius on skid-steered wheeled robot power consumption on loose soil* (Master's thesis, Concordia University). Retrieved from https://spectrum.library.concordia.ca/id/eprint/985917/ (Unpublished)

Gonzalez, R., Apostolopoulos, D., & Iagnemma, K. (2018). Slippage and immobilization detection for planetary exploration rovers via machine learning and proprioceptive sensing. *Journal of Field Robotics*, *35*(2), 231–247. https://doi.org/10.1002/rob.21736.

Gonzalez, R., Chandler, S., & Apostolopoulos, D. (2019). Characterization of machine learning algorithms for slippage estimation in planetary exploration rovers. *Journal of Terramechanics*, *82*, 23–34. https://doi.org/10.1016/j.jterra.2018.12.001.

Gonzalez, R., Fiacchini, M., & Iagnemma, K. (2018). Slippage prediction for off-road mobile robots via machine learning regression and proprioceptive sensing. *Robotics and Autonomous Systems*, *105*, 85–93. https://doi.org/10.1016/j.robot.2018.03.013.

Gonzalez, R., & Iagnemma, K. (2018, June). Slippage estimation and compensation for planetary exploration rovers. State of the art and future challenges. *Journal of Field Robotics*, *35*(4), 564–577. https://doi.org/10.1002/rob.21761.

Gonzalez, R., Rodriguez, F., Guzman, J. L., Pradalier, C., & Siegwart, R. (2012). Combined visual odometry and visual compass for off-road mobile robots localization. *Robotica*, *30*(6), 865–878. https://doi.org/10.1017/S026357471100110X.

Google. (n.d.). *Google Maps CSA Mars Yard.* Retrieved 2022-04-07, from https://www.google.com/maps/place/Canadian+Space+Agency+%7C+Agence+spatiale+canadienne/@45.5188084,-73.3931719,110a,35y,180h,39.53t/data=!3m1!1e3!4m9!1m2!2m1!1sCSA!3m5!1s0x4cc9040f11be6b73:0x8b6009a6b418a283!8m2!3d45.520008!4d-73.393547!15sCgNDU0EiA4gBAZIBGWZlZGVyYWxfZ292ZXJubWVudF9vZmZpY2U!5m1!1e4

Helmick, D. M., Cheng, Y., Clouse, D. S., Matthies, L. H., & Roumeliotis, S. I. (2004). Path following using visual odometry for a mars rover in high-slip environments. In *2004 ieee aerospace conference proceedings (ieee cat. no. 04th8720)* (Vol. 2, pp. 772–789). https://doi.org/10.1109/AERO.2004.1367679.

Hosmer Jr, D. W., Lemeshow, S., & Sturdivant, R. X. (2013). *Applied logistic regression* (Vol. 398). John Wiley & Sons.

Hsu, C.-W., Chang, C.-C., Lin, C.-J., & others. (2003). *A practical guide to support vector classification.* Taipei, Taiwan. Retrieved from https://www.csie.ntu.edu.tw/~cjlin/papers/guide/guide.pdf

Li, J., Aubin-Fournier, P.-L., & Skonieczny, K. (2020). Slaam: Simultaneous localization and additive manufacturing. *IEEE Transactions on Robotics*, *37*(2), 334–349. https://doi.org/10.1109/TRO.2020.3021241.

Lopez-Arreguin, A. J. R., & Montenegro, S. (2021). Machine learning in planetary rovers: A survey of learning versus classical estimation methods in terramechanics for in situ exploration. *Journal of Terramechanics*, *97*, 1–17. https://doi.org/10.1016/j.jterra.2021.04.005.

Maimone, M., Patel, N., Sabel, A., Holloway, A., & Rankin, A. (2022). Visual odometry thinking while driving for the curiosity mars rover's three-year test campaign: Impact of evolving constraints on verification and validation. In *2022 ieee aerospace conference (aero)* (pp. 1–10). https://doi.org/10.1109/AERO53065.2022.9843487.

McRae, J., Powell, C., & Wismer, R. (1965). Performance of soils under tire loads, report 1: test facilities and techniques. *U.S. Army Engineer Waterways Experiment Station*.

Niksirat, P., Daca, A., & Skonieczny, K. (2020). The effects of reduced-gravity on planetary rover mobility. *The International Journal of Robotics Research*, *39*(7), 797–811. https://doi.org/10.1177/0278364920913945.

Nourizadeh, P., Stevens McFadden, F. J., & Browne, W. N. (2022). In situ slip estimation for mobile robots in outdoor environments. *Journal of Field Robotics*. https://doi.org/10.1002/rob.22141.

Ojeda, L., Cruz, D., Reina, G., & Borenstein, J. (2006). Current-based slippage detection and odometry correction for mobile robots and planetary rovers. *IEEE Transactions on robotics*, *22*(2), 366–378. https://doi.org/10.1109/TRO.2005.862480.

Omura, T., & Ishigami, G. (2017). Wheel slip classification method for mobile robot in sandy terrain using in-wheel sensor. *Journal of Robotics and Mechatronics*, *29*(5), 902–910. https://doi.org/10.20965/jrm.2017.p0902.

Oravec, H. A., Zeng, X., & Asnani, V. M. (2010). Design and characterization of GRC-1: A soil for lunar terramechanics testing in earth-ambient conditions. *Journal of Terramechanics*, *47*(6), 361–377. https://doi.org/10.1016/j.jterra.2010.04.006.

Pisner, D. A., & Schnyer, D. M. (2020). Support vector machine. In *Machine Learning* (pp. 101–121). Elsevier. https://doi.org/10.1016/B978-0-12-815739-8.00006-7.

Reina, G., Ishigami, G., Nagatani, K., & Yoshida, K. (2010). Odometry correction using visual slip angle estimation for planetary exploration rovers. *Advanced Robotics*, *24*(3), 359–385. https://doi.org/10.1163/016918609X12619993300548.

Reina, G., Ojeda, L., Milella, A., & Borenstein, J. (2006). Wheel slippage and sinkage detection for planetary rovers. *IEEE/Asme Transactions on Mechatronics*, *11*(2), 185–195. https://doi.org/10.1109/TMECH.2006.871095.

Rieber, R., McHenry, M., Twu, P., & Stragier, M. M. (2022). Planning for a martian road trip-the mars2020 mobility systems design. In *2022 ieee aerospace conference (aero)* (pp. 01–18).

https://doi.org/10.1109/AERO53065.2022.9843375.

Scikit-learn: Svm module. (2022). Retrieved 2022-10-27, from https://scikit-learn.org/stable/modules/svm.html

Skonieczny, K., Shukla, D. K., Faragalli, M., Cole, M., & Iagnemma, K. D. (2019). Data-driven mobility risk prediction for planetary rovers. *Journal of Field Robotics*, *36*(2), 475–491.